NAVAL POSTGRADUATE SCHOOL

MONTEREY, CALIFORNIA

THESIS

AUTOMATING NEARSHORE BATHYMETRY
EXTRACTION FROM WAVE MOTION IN SATELLITE
OPTICAL IMAGERY

by

Steven Mancini

March 2012

Thesis Advisor: Richard C. Olsen
Second Reader: Jamie MacMahan

Approved for public release; distribution is unlimited

THIS PAGE INTENTIONALLY LEFT BLANK

13. ABSTRACT (maximum 200 words)

Nearshore depths for Waimanalo Beach, HI, are extracted from optical imagery, taken by the WorldView-2 satellite on 31 March 2011, by means of automated wave kinematics bathymetry (WKB). Two sets of three sequential images taken at intervals of about 10 seconds are used for the analyses herein. Water depths are calculated using a computer program that registers the images, estimates the currents, and then uses the linear dispersion relationship for surface gravity waves to estimate depth. Depths are generated from close to shore out to about 20 meters depth. Comparisons with SHOALS LIDAR bathymetry values show WKB depths are accurate to about half a meter, with R^2 values of 90%, and are frequently in the range of 10–20 percent relative error for depths ranging from 2–16 meters.

THIS PAGE INTENTIONALLY LEFT BLANK

AUTOMATING NEARSHORE BATHYMETRY EXTRACTION FROM WAVE MOTION IN SATELLITE OPTICAL IMAGERY

Steven Mancini
Commander, United States Navy
B.S., Xavier University, 1992

Submitted in partial fulfillment of the
requirements for the degree of

MASTER OF SCIENCE IN SPACE SYSTEMS OPERATIONS

from the

NAVAL POSTGRADUATE SCHOOL
March 2012

Author: Steven Mancini

Approved by: Dr. Richard C. Olsen
                Thesis Advisor

                Dr. Jamie MacMahan
                Second Reader

                Dr. Rudy Panholzer
                Chair, Space Systems Academic Group

THIS PAGE INTENTIONALLY LEFT BLANK

ABSTRACT

Nearshore depths for Waimanalo Beach, HI, are extracted from optical imagery, taken by the WorldView-2 satellite on 31 March 2011, by means of automated wave kinematics bathymetry (WKB). Two sets of three sequential images taken at intervals of about 10 seconds are used for the analyses herein. Water depths are calculated using a computer program that registers the images, estimates the currents, and then uses the linear dispersion relationship for surface gravity waves to estimate depth. Depths are generated from close to shore out to about 20 meters depth. Comparisons with SHOALS LIDAR bathymetry values show WKB depths are accurate to about half a meter, with R^2 values of 90%, and are frequently in the range of 10–20 percent relative error for depths ranging from 2–16 meters.

THIS PAGE INTENTIONALLY LEFT BLANK

TABLE OF CONTENTS

THIS PAGE INTENTIONALLY LEFT BLANK

LIST OF FIGURES

xiii

THIS PAGE INTENTIONALLY LEFT BLANK

LIST OF TABLES

THIS PAGE INTENTIONALLY LEFT BLANK

LIST OF ACRONYMS AND ABBREVIATIONS

2MSI   Two-image Multispectral

2Pan   Two-image Panchromatic

3MSI   Three-image Multispectral

3Pan   Three-image Panchromatic

AROSS   Airborne Remote Optical Spotlight System

CDIP   Coastal Data Information Program

CHARTS   Compact Hydrographic Airborne Rapid Total Survey

GUI   Graphical User Interface

IHO   International Hydrographic Organization

JALBTCX   Joint Airborne LIDAR Bathymetry Technical Center of Expertise

LIDAR   Light Detection and Ranging

MLLW   Mean Lower Low Water

RMS   Root Mean Squared

SAR   Synthetic Aperture Radar

SHOALS   Scanning Hydrographic Operational Airborne LIDAR Survey

SNR   Signal-to-Noise Ratio

STK   Satellite Tool Kit

UTM   Universal Transverse Mercator

WKB   Wave Kinematics Bathymetry

THIS PAGE INTENTIONALLY LEFT BLANK

ACKNOWLEDGMENTS

THIS PAGE INTENTIONALLY LEFT BLANK

I. INTRODUCTION

A. PURPOSE OF RESEARCH

Characterizing the environmental parameters of the battlespace ahead of a military operation can enable the planners and decision makers to understand the potential impacts the environment might have. This can help them conduct safer and more efficient operations. One parameter that is extremely important for certain operations conducted in the nearshore is bathymetry. Amphibious landings, mine warfare operations, reconnaissance missions, and other special operations missions performed in the nearshore region require accurate and up-to-date bathymetric information. Without it, the operation could be hampered by difficulties, such as vessel groundings, causing equipment damage, personnel injuries or death, delays, and perhaps mission failure.

Several methods and techniques are currently employed to determine nearshore bathymetry. Hydrographic surveys, especially those that require International Hydrographic Organization (IHO) standards, such as for navigation charts, are typically performed using acoustic systems, such as single and multi-beam sonar, mounted on a vessel. Relying on relatively high frequency sound to illuminate the bottom, they are very accurate but time consuming owing to their small swath, sometimes taking many days to map a region of interest.

The Compact Hydrographic Airborne Rapid Total Survey (CHARTS) system (Figure 1), an airplane with a Light Detection and Ranging (LIDAR) instrument mounted on it, is also very accurate and can perform large area surveys in a much shorter time. Both of these methods, however, require uncontested access to the region of interest. Often times, military operations are conducted in denied areas, where survey vessels and aircraft are in danger of being fired upon. In addition, due to the high cost and demand of these scarce resources, it is impractical to resurvey the same area regularly using these

methods. This leads to significant time intervals between surveys allowing natural nearshore processes, such as tidal currents and storms, to alter the bathymetry, potentially rendering older surveys inaccurate.
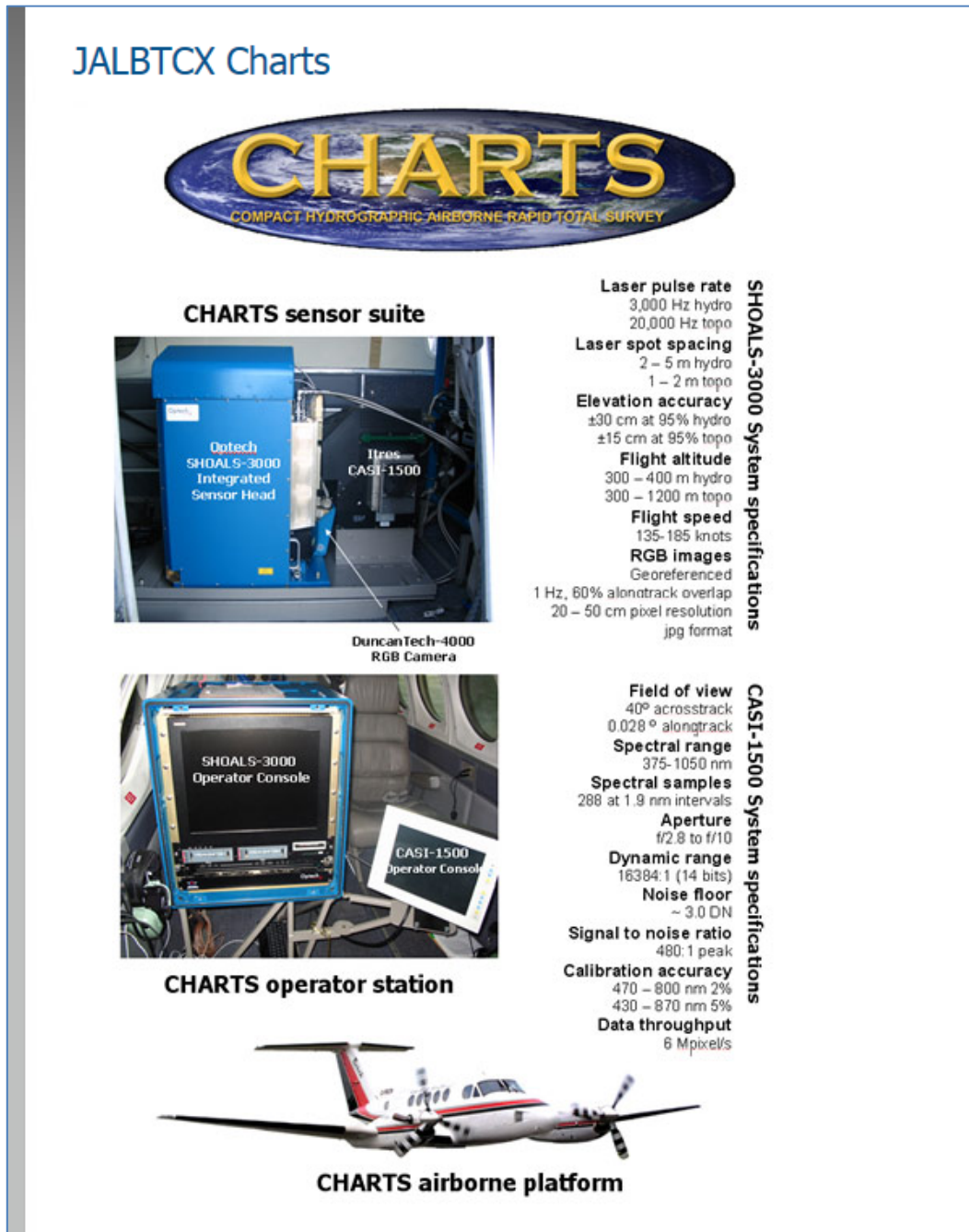
Figure 1.   Compact Hydrographic Airborne Rapid Total Survey (From Joint Airborne LIDAR Bathymetry Technical Center of Expertise, 2011).

If IHO standards are not required, other methods exist that are better protected from adversaries through greater stand-off distances, are much lower in cost, and have frequent revisit capability, especially those that use satellite-based sensors. Nearshore bathymetry can be extracted from satellite multispectral imagery by applying the linear dispersion theory of surface gravity waves, which is the focus of this research. Previous research into this method at the Naval Postgraduate School focused on determining the viability and accuracy of this method, but used a manual, time-intensive process (Myrick, 2011; McCarthy, 2010). The purpose herein is to take the next step by investigating an algorithm that automates this process. A few of the other methods that have been or are still being explored are briefly discussed in Chapter II.

B. SPECIFIC OBJECTIVES

The objective is to investigate an automated method for determining nearshore bathymetry using remotely sensed images of the Waimanalo Beach area of Hawaii. A desire to reduce the time and effort required to extract the bathymetry information, therefore greatly increasing the efficiency of the process as compared to the previous work is what provided motivation for this effort.

The WorldView-2 satellite took the multispectral and panchromatic images in rapid succession in March 2011. The imagery was orthorectified, converted to Universal Transverse Mercator (UTM) coordinates, and processed using a Wave Kinematics Bathymetry (WKB) computer algorithm to: crop the images to the desired analysis area; register the images to one another (~ 1 m accuracy); apply filters and distinguish between land, clouds, and water and; finally, extract current and depth fields by fitting a solution to the data (Abileah, 2006). The resulting estimated depth fields were compared to ground truth data collected by the Joint Airborne LIDAR Bathymetry Technical Center of Expertise (JALBTCX) during survey operations using the CHARTS system with a Scanning Hydrographic Operational Airborne LIDAR Survey (SHOALS)-3000 bathymetric LIDAR (Figure 1). This study reaffirms that applying the linear dispersion relation for surface gravity waves to wave data collected from multispectral satellite imagery is a viable technique for determining bathymetry in denied or restricted areas.

THIS PAGE INTENTIONALLY LEFT BLANK

II. BACKGROUND

A. INTRODUCTION

For many years, nearshore bathymetry has been determined without the use of direct measurement, such as a sounding line, even as far back as World War I (Myrick, 2011). Described in more detail in Myrick's paper, those early methods consisted of the waterline, transparency, wave celerity, and wave period methods. The waterline method relied on aerial photographs of the beach at times of low tides, when the bottom was partially exposed. The transparency method exploited the concept that deeper water absorbs more light and, thus appears darker in aerial photographs. The wave period method used the fact that the period is constant as a wave propagates so a relationship can be established between the period, the wavelength, and the water depth at multiple locations. These methods all had limitations that made them marginally useful, but were sometimes arguably better than having no bathymetry information at all (Myrick, 2011).

The wave celerity method, which invokes the linear dispersion relation discussed shortly, was also very limited before more accurate timekeeping and better resolution images became available. Modern remote sensing technology has removed these previous handicaps and the wave celerity method is now a viable one for determining water depth in nearshore regions (Myrick, 2011). The wave celerity method is the method used as the foundation for this study.

B. THEORY

Surface gravity waves propagating in the ocean obey the linear dispersion relation between wave celerity, or phase speed, c; wave period (T); wavelength (λ); and water depth (d). The dispersion relation for surface gravity waves is:

$$\omega^2 = gk \tanh(kd), \tag{1}$$

where ω is the angular frequency ($\omega = 2\pi/T$), g is the acceleration due to gravity, and k is the wavenumber ($k = 2\pi/\lambda$) (Herbers, 2003). For large kd, which is the case in deep water, $\tanh(kd) \approx 1$ and the dispersion relation reduces to:

$$\omega^2 = gk \,. \tag{2}$$

In shallow water, where $kd \ll 1$, $\tanh(kd) \approx kd$, so the dispersion relation reduces to:

$$\omega = \sqrt{gd}k \,. \tag{3}$$

The corresponding limits of the phase speed $c = \omega/k$ are:

$$c = \frac{g}{\omega} \qquad \text{for deep water} \tag{4}$$

$$c = \sqrt{gd} \qquad \text{for shallow water.} \tag{5}$$

The conclusion from Equations (4) and (5) is that deep water waves are dispersive, whereas shallow water waves are nondispersive. That is, the phase speed of deep water waves is a function only of ω, whereas the phase speed of shallow water waves is independent of ω and is instead, only a function of depth (Herbers, 2003). Another way to think of this is, as waves travel from deep to shallow water, their frequency and period remain constant, forcing phase speed to decrease and wavenumber to increase with decreasing depth. Since these changes are proportional to each other, this is exactly the phenomenon that is exploited to extract the water depth.

In addition to waves slowing and getting shorter as they shoal, another physical effect is an increase in their amplitude. This effect becomes important in the surf zone, where the waves break and wave height increases wave speed. The nonlinear processes that occur in the surf zone and add speed to the waves are not accounted for in the linear dispersion relation. This introduces error, usually in the form of overestimated depths because of the additional speed (Myrick, 2011). Equation (1) is actually a very good approximation for depths greater than 2 m, and is still valid at 1 m depths with moderate wave heights (Abileah, 2006). Therefore, caution is necessary when using any method that relies on the dispersion relation in the very shallow depths of the surf zone.

It can be shown that the wave induced velocity components and the water pressure decay exponentially with depth as $kd \to \infty$ (deep water). In fact, by only half a wavelength below the surface, these parameters are reduced to about 4% of their surface

values (Herbers, 2003). For this reason, a good thumb rule is: regions where the depth is greater than half the wavelength are deep water and the dispersion relation does not help in determining water depth, since phase speed does not depend on depth in this regime. For the purposes of this study, regions where the depth is less than half the wavelength will be considered "nearshore" and is the regime where the dispersion relation is useful for this technique. It should be noted that this definition includes both the shallow water regime, discussed previously, and the intermediate water depth regime, where phase speed depends on both frequency and depth.

C.   SOME MODERN METHODS FOR DETERMINING NEARSHORE BATHYMETRY

Several methods using different techniques have been developed that use modern remote sensing technology to determine nearshore bathymetry. The methods discussed are only a few of the many methods and techniques currently being investigated by a multitude of researchers.

1.   Airborne Passive Optical System (Using Linear Dispersion Theory)

The basis of modern methods using the dispersion relation is to collect ocean images, extract the space-time characteristics of the waves in the images, then transform this data into spectra that can be used to retrieve depth and currents.

The first method employs a passive optical system mounted on an aircraft (Figure 2). This turret-based system, called the Airborne Remote Optical Spotlight System (AROSS), maps a time series of images to a common geodetic surface by carefully measuring the imaging geometry (Dugan et al., 2001a). It was designed using commercial off-the-shelf technology with the intention of ultimately mounting it on unmanned aerial vehicles.

Precisely registering the images to each other is critical to obtaining accurate results. Other important considerations are: adequate spatial resolution to resolve the smallest waves (the resulting viewing geometry typically yields a sufficient 2 m), large

enough field of view to capture several of the longest waves (2 km x 2 km is typically used), and dwell times long enough to observe several of the longer wave periods (30 s or greater is used) (Dugan et al., 2001a).
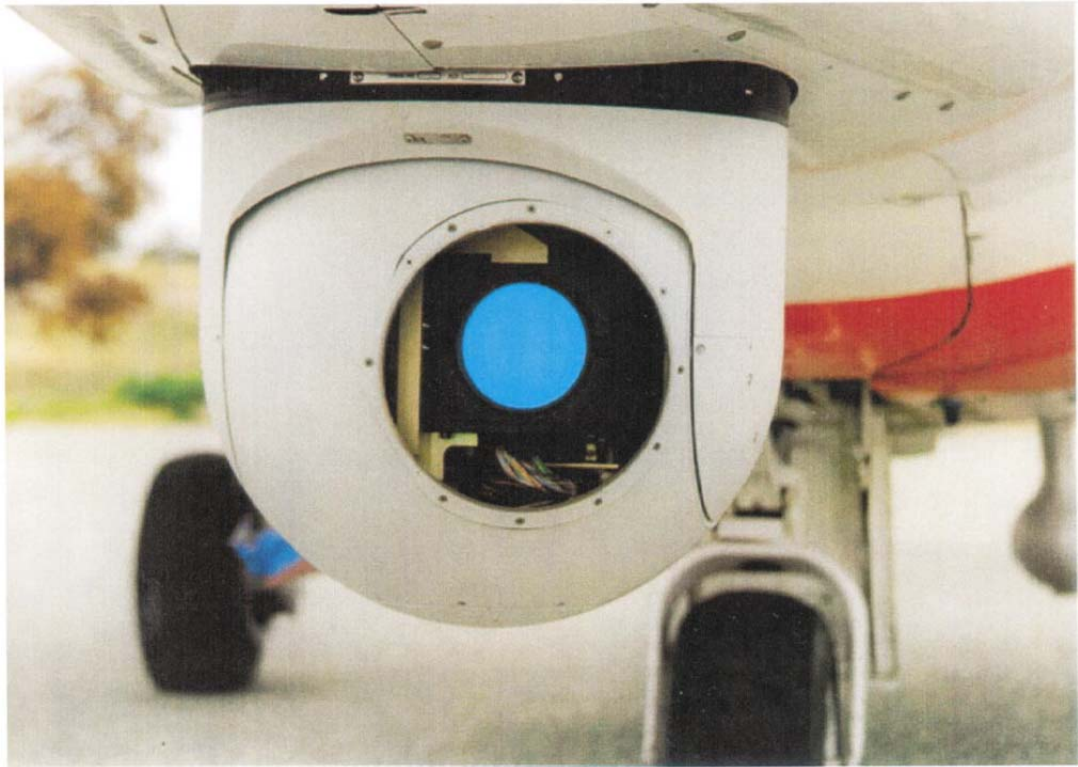
Figure 2.   Close-up photo of camera and turret as mounted on the nose cone
of the Pelican aircraft (From Dugan et al., 2001a).

One data set using AROSS was collected during the Shoaling Waves Experiment in the Outer Banks of North Carolina in 1999. A three-dimensional (3-D) Fourier transform was used to turn a data cube consisting of 2 minutes' worth of data from an area approximately 500 x 500 m into a frequency-wavenumber power spectrum. Figure 3 shows a two-dimensional (2-D) slice through the resulting power spectrum, oriented in the direction of the primary swell waves. The theoretical dispersion surface that includes no current and is for infinite depth is represented by the dashed curve at the intersection of the dispersion surface with the plane of the slice. The wave energy is concentrated in a

narrow ridge that is slightly skewed off of the theoretical curve. The depth and current are determined by calculating a surface that fits the measured wave spectrum. The resulting dispersion surface is denoted by the solid curve and, in this case, a depth of 8.2 m and current speed of 0.14 m/s is the solution (Dugan, Piotrowski, & Williams, 2001b).
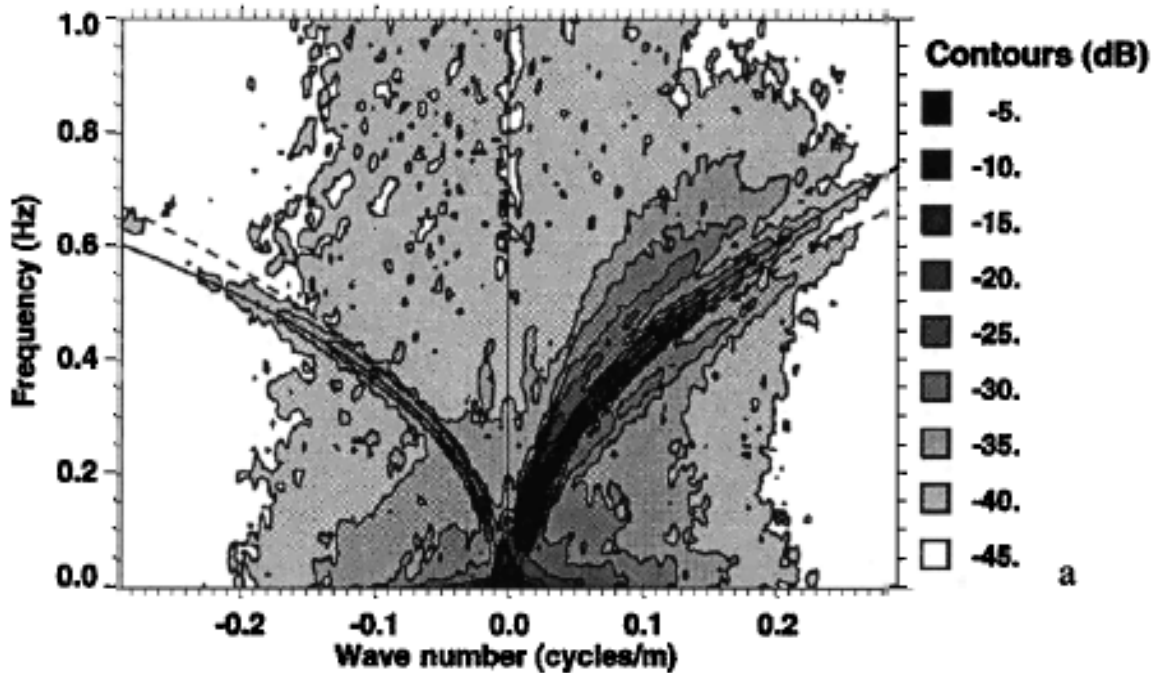
Figure 3.   Frequency-wavenumber slice, from Outer Banks study, through the power spectrum, oriented in the direction of the primary swell waves. The theoretical dispersion surface that includes no current and is for infinite depth is represented by the dashed curve. The depth and current are determined by calculating a dispersion surface that fits the measured wave spectrum, denoted by the solid curve (From Dugan et al., 2001b).

Another AROSS study was conducted in the Monterey Bay in 1999. The same size tiles were used, but in this case, only 1 minute of data was Fourier transformed. A slice through the 3-D spectrum in the direction of the wind waves is shown in Figure 4. Again, the solid curve is the intersection of the deep water dispersion surface (i.e., no current and infinite depth), but this time the wave energy is closely distributed along this curve. Since the data closely match the theoretical curve, it can be surmised that no

significant surface currents were present during the collection. There is, however, a slight shift of the low frequency energy off the curve. This is due to the longer waves (50–100 m wavelengths) feeling the bottom because the depth at the imaged location is not infinite (i.e., is less than half a wavelength deep). The actual depth, as determined from nautical charts, is about 18 m (Dugan et al., 2001a).
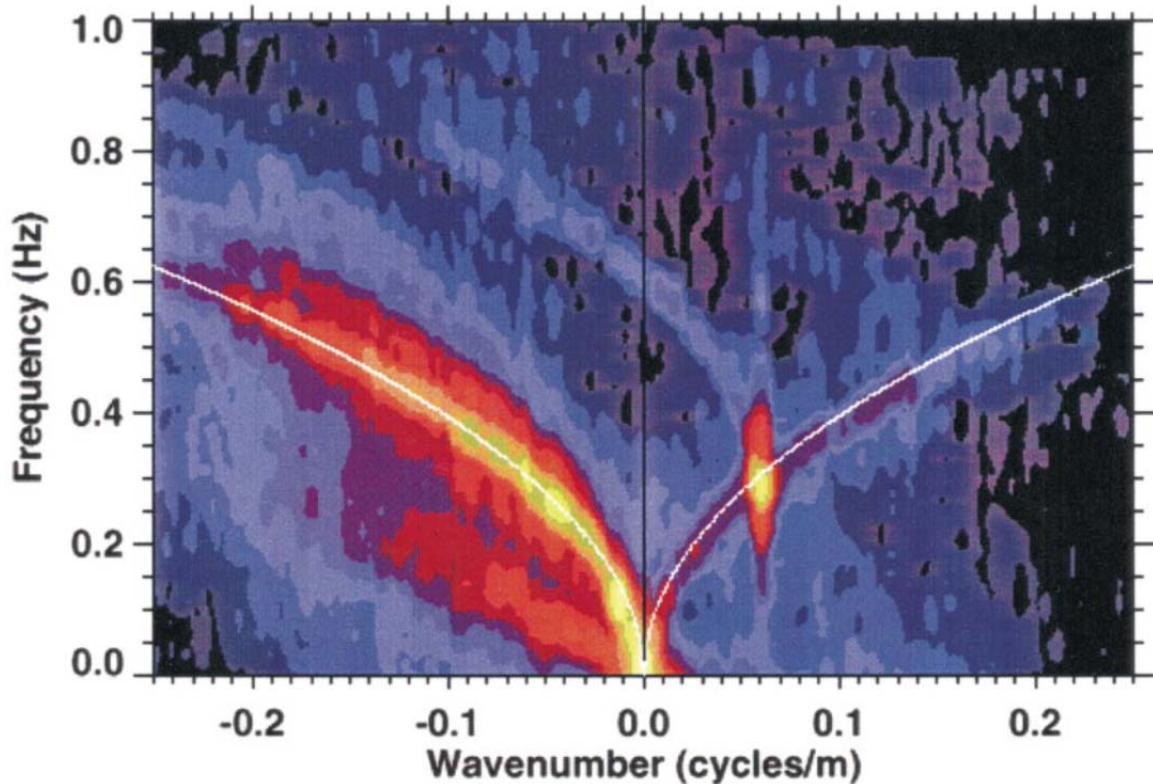
Figure 4.   Frequency-wavenumber slice, from Monterey Bay study, through the power spectrum, in the direction of the wind. The solid curve is the intersection of the deep water dispersion surface (i.e., no current and infinite depth). The wave energy is closely distributed along this curve, indicating that no significant surface currents were present during the collection (From Dugan et al., 2001a).

One of the conclusions from these and similar studies is that a dwell (total image time series length) of 1 minute or more is required for high accuracy. The root mean squared (RMS) error approaches 5% for 2-minute dwell times, but increases rapidly with shorter dwell times (Figure 5). This graph is based on using 3-D Fourier transforms in

the inversion algorithm. The algorithm in this study uses a 2-D Fourier transform that results in a much flatter curve where errors do not sharply increase at shorter dwell times. In the aforementioned two studies, the depths agreed within 15% and the currents within 10% of the in situ values (Dugan, Piotrowski, & Williams, 2002).
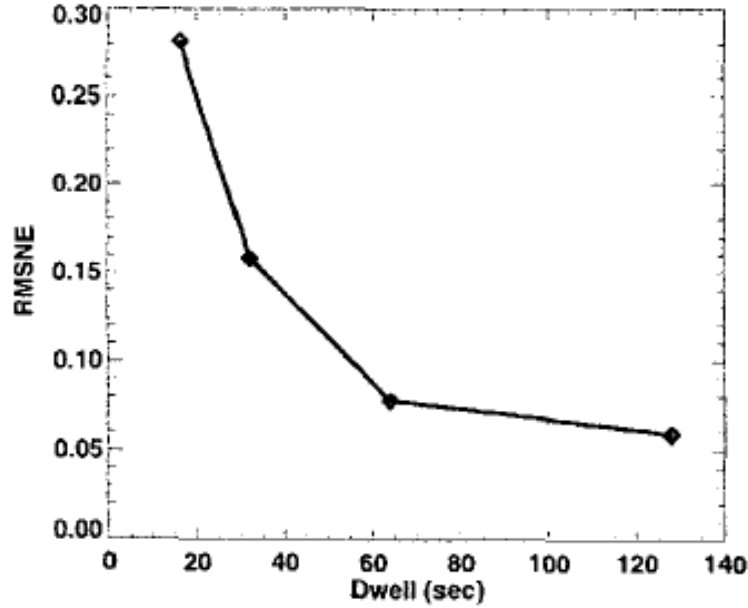
Figure 5.   RMS error as a function of dwell (From Dugan et al., 2002).

2.   Synthetic Aperture Radar (Using Wave Refraction)

Another remote sensing application for determining nearshore bathymetry uses Synthetic Aperture Radar (SAR), which can be done from both airborne and space-based platforms. The basis for this method is to examine wave refraction as determined by SAR imagery using the two-scale Bragg scattering model. The Bragg scattering model assumes that the SAR image brightness of a patch of ocean is proportional to the amplitude of the Bragg waves. Bragg waves are small-scale ocean surface waves that have wavelengths equal to that of the projection of the transmitted radar electromagnetic wavelength onto the surface, and are propagating directly toward or away from the sensor (Wackerman & Clemente-Colon, 2004). An expression for this geometry is:

$$\lambda_B = \frac{\lambda_e}{2\sin\theta},$$

(6)

11

where λ_B is the Bragg wavelength, λ_e is the SAR electromagnetic wavelength, and θ is the local incident angle of the ocean surface. This geometry produces a scattering pattern of the SAR radiation that leads to constructive interference and the corresponding brightness in the image (Wackerman & Clemente-Colon, 2004).

The two-scale aspect of the model is illustrated in Figure 6, which shows a slice through a simplified ocean surface consisting of one large-scale and one small-scale wave. The Bragg waves are the smaller scale waves shown embedded in and riding on the large-scale surface waves. Flat plates, a few Bragg wavelengths in size, are then used to model the radar's interaction with the surface. The plates tilt and move based on the local slope and motion of the large-scale wave surface, changing the radar image signature as they do (Wackerman & Clemente-Colon, 2004).
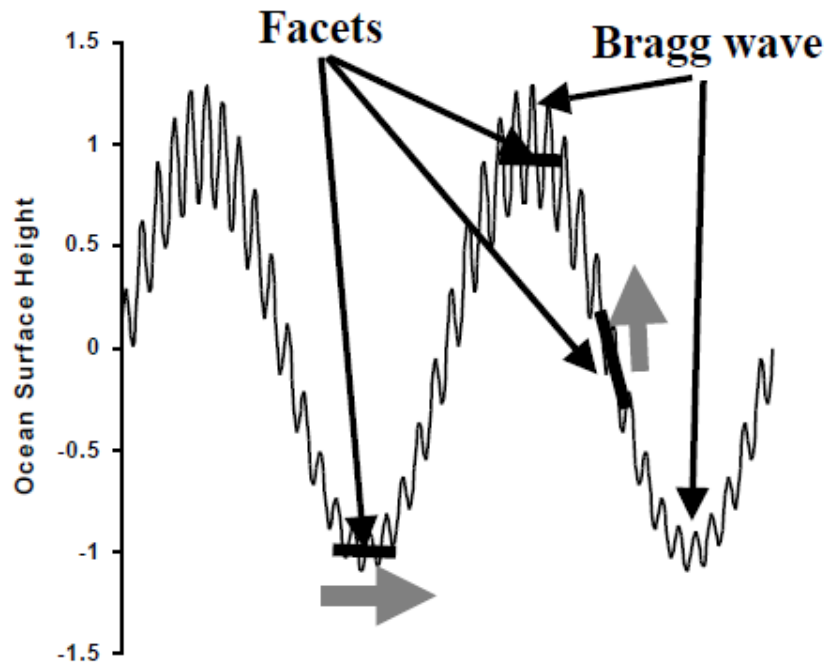
Figure 6.   Two-scale model illustrating Bragg waves (the smaller scale waves) embedded in and riding on the large-scale surface waves. Flat plates, a few Bragg wavelengths in size, model the radar's interaction with the surface. The plates tilt and move based on the local slope and motion of the large-scale wave surface (From Wackerman & Clemente-Colon, 2004).

12

Bathymetry is estimated using SAR by determining the amount of wave refraction that occurs in the images and using propagation models that predict wave refraction as a function of depth. Waves refract as they move from deep water toward the shore at an angle to the bathymetric contours, which forces them to turn and align with the shore. This turning is due to a differential interaction with the ocean bottom (i.e., one end of the wave front reaches shallower water before the other end and, therefore, slows down sooner). The faster the depth decreases, the more quickly the wave will turn and become parallel to the coast. Since refraction will not occur if the waves start out parallel to the shore in deep water, this method is ineffective in those instances (Wackerman & Clemente-Colon, 2004).

3. Aerial Photography (Using Radiometric Techniques)

A third modern method relies on radiometric techniques to extract water depth in shallow areas from multispectral optical imagery. These techniques are based on applying algorithms to interpret the radiance received by the imager. This method requires fairly clear water to work, so it is not useful in the many turbid nearshore locations around the globe.

A simple water reflectance model that accounts for most of the received signal is represented by:

$$L_i = L_{si} + k_i r_{Bi} e^{-K_i f z} , \tag{7}$$

where L_{si} is the radiance over deep water; k_i is a constant that accounts for the solar irradiance, the transmittance of the atmosphere and the water surface, and refraction at the surface; r_{Bi} is the bottom reflectance; K_i is the effective attenuation coefficient for water; f is a geometric factor to account for the path length through the water; and z is the water depth (Lyzenga, 1978). Using this equation to solve for z is the obvious way to determine the depth.

A ratio algorithm was developed to help remove the effect of changes in bottom reflectance on the depth calculation, so the model can be applied to scenes in which the bottom composition changes. The algorithm can be represented by:

$$z = \frac{1}{(K_1 - K_2)f} \left[\ln\left(\frac{k_1}{k_2}\right) - \ln\left(\frac{R}{R_b}\right) \right], \tag{8}$$

where R is the ratio of the bottom-reflected signals in two bands:

$$R = (L_1 - L_{s1}) / (L_2 - L_{s2}), \tag{9}$$

and R_b is the ratio of the bottom reflectances in the same two bands. The assumption is made that the two bands chosen have the same bottom reflectance ratio for all the bottom types in the scene, which is a decent assumption for multispectral systems. This algorithm is used with moderate success over relatively clear water on data collected from both satellites and aircraft (Lyzenga, 1978).

To increase operational flexibility and improve performance, a more general, albeit more complex, algorithm was developed that modified the preceding model to include the effects of scattering in the water and internal reflection at the water surface. It depends on proper classification of the bottom types in the scene, which is done prior to the depth computation, and it is at least as good as the ratio model at doing this for the case of two bands (Lyzenga, 1978). Arguably, using more bands would improve the performance of the bottom classification portion of the algorithm.
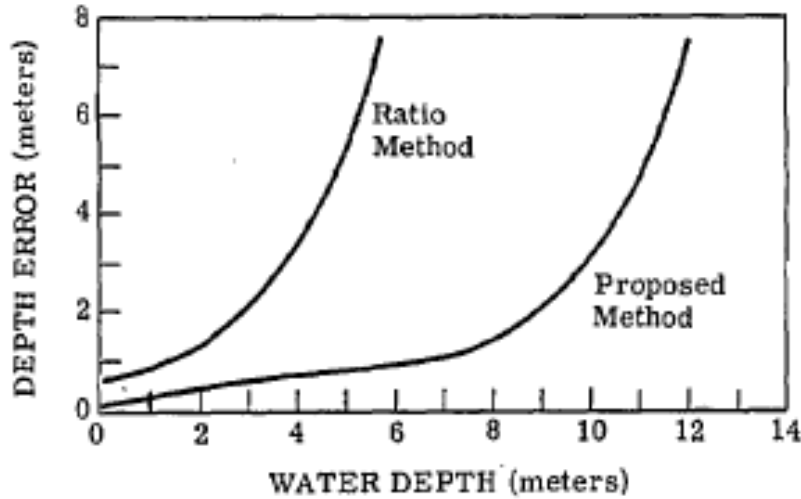
Figure 7.   Depth error comparison of the ratio and modified methods (From Lyzenga, 1978).

14

Once the bottom is classified, the depth, z, is calculated using:

$$Y_N = B_m - Cz,$$ (10)

where Y_N is the set of depth dependent variables, B_m is a function of the bottom composition (and its value is determined via the aforementioned classification), and C characterizes the water attenuation. This procedure introduces error both through noise associated with Y_N and if there happens to be any misclassification of the bottom (Lyzenga, 1978). Compared to the ratio method, which is subject to much higher noise errors, its performance is much improved (Figure 7).

THIS PAGE INTENTIONALLY LEFT BLANK

III. EXPERIMENT DESIGN

A. PROBLEM DEFINITION

Using satellite optical imagery to view wave motion in order to extract the bathymetry of nearshore areas using the linear dispersion relation for surface gravity waves has its advantages in certain situations. When IHO standards are not required, it is much more cost effective and efficient to use this method rather than LIDAR-equipped aircraft or sonar-equipped vessels. There is no need to dispatch expensive, hard-to-get assets to remote locations, since the existing low earth orbiting satellites will be overhead most locations every few days. It is especially good for denied or hostile areas because the satellites do not attract attention and remain safely out of the range of most weapons, unlike aircraft and ships.

Table 1.   Comparison of bathymetry methods using remote sensing (From Abileah, 2006).

	Depth accuracy	Horizontal resolution	Airborne/Satellite	Turnaround (months)[1]	Cost / sq km[1]	Turbid waters	Day/ night
Airborne Bathymetric Lidar	IHO-1	IHO-1	Airborne	6-12	>$100 0	X	✓
Photobathymetry	Variable	10-30 m	Both	1-2	$50	X	X
Currents interaction	Variable	25 m²	Both	1	$10	✓	✓
Wave refraction	10-20%	1 km	Both	1	$10	✓	✓
WKB	5-10%	50-200 m	Both	1-2	$50	✓	✓[3]

Notes: [1]Rough-order-of-magnitude assuming satellites, except ABL, which is on aircraft. [2]Ref: Argoss website (www.argoss.nl). [3]WKB with the satellite imagery described in this paper is daytime only. However nighttime is possible with long wave IR (Farber, 1995), nautical X-band radars (see text), and theoretically possibly with space SAR.

Other satellite remote sensing techniques offer these same advantages. However, they each have limitations that make each method suitable only in certain situations. Table 1 compares some of the properties of each method. The optical radiance method (Lyzenga, 1978), referred to as photobathymetry in the table, is good for relatively clear water during cloudless, daytime passes and has one of the best horizontal resolutions, but

it is not a good option for turbid waters, cloudy regions, or nighttime passes. It also requires in situ knowledge for calibration purposes, negating its usefulness in inaccessible areas (Abileah, 2006).

The wave refraction SAR method (Wackerman & Clemente-Colon, 2004) is a good all-weather, day or night option, and it does not rely on water clarity; but it has the least horizontal resolution and is not the most accurate method. The WKB method in this study, works fine in turbid waters, but is not a good option when the scene is obscured by clouds or for nighttime passes (when optical imagery is used), or when ocean waves are not present (harbors, calm seas, etc.). It has decent depth accuracy and horizontal resolution, and does not need in situ data for calibrating, making it well suited for denied areas. In order to optimize the wave contrast in the images, the camera should point in the direction of the sun while avoiding the 20–30° sun glint cone (Abileah, 2006).

This study assesses a WKB computer algorithm that automates the nearshore bathymetry extraction on imagery of the southeastern portion of the Hawaiian island of Oahu, obtained by the WorldView-2 satellite.
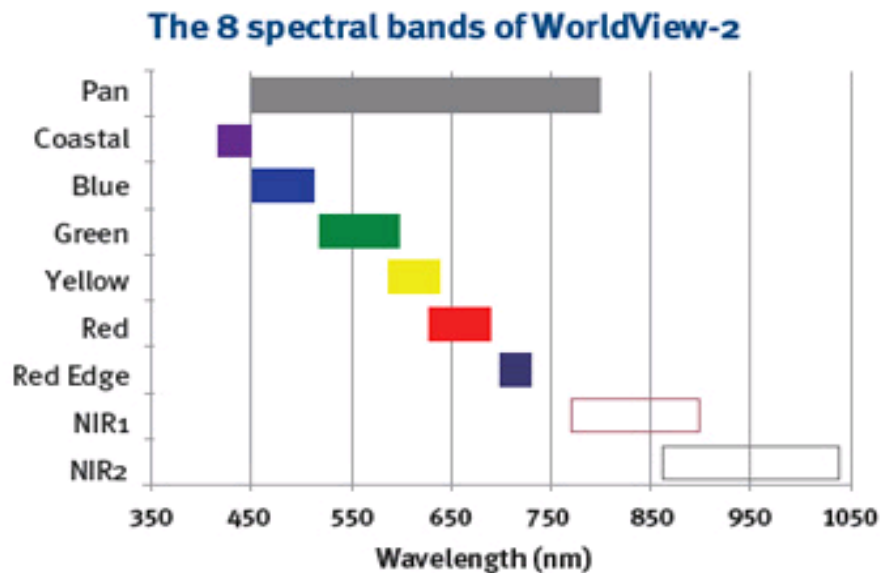
Figure 8.   WorldView-2 sensor bands showing their relative positions and overlap in the electromagnetic spectrum (From DigitalGlobe, 2011b).

B. MATERIALS

1. WorldView-2 Satellite

The WorldView-2 satellite was launched into a 770 km high, sun synchronous orbit in October 2009 from Vandenberg Air Force Base. The third in DigitalGlobe's commercial imaging satellite constellation, it has a state-of-the-art multispectral optical imager and provides approximately 2 m multispectral and 0.5 m panchromatic resolution imagery. The panchromatic and eight multispectral bands and their relative positions and overlap in the electromagnetic spectrum are illustrated in Figure 8. The sensor has a revisit time of 1–4 days, depending on desired viewing angle and resolution. It collects imagery in a swath 16.4 km wide at nadir and can slew 200 km in 10 seconds. Some additional key specifications are listed in Table 2 (DigitalGlobe, 2011a).

Table 2.   Key WorldView-2 specifications (After DigitalGlobe, 2011a)

Sensor Bands	Panchromatic: 450 - 800 nm 8 Multispectral: Coastal: 400 - 450 nm Red: 630 -690 nm Blue: 450 - 510 nm Red Edge: 705 - 745 nm Green: 510 - 580 nm Near-IR1: 770 - 895 nm Yellow: 585 - 625 nm Near-IR2: 860 - 1040 nm
Sensor Resolution	Panchromatic: 0.46 m GSD at nadir, 0.52 m GSD at 20° off-nadir Multispectral: 1.85 m GSD at nadir, 2.07 m GSD at 20° off-nadir
Dynamic Range	11-bits per pixel
Swath Width	16.4 km at nadir
Attitude Determination and Control	3-axis stabilized Actuators: Control Moment Gyros (CMGs) Sensors: Star trackers, solid state IRU, GPS
Pointing Accuracy and Knowledge	Accuracy: <500 m at image start and stop Knowledge: Supports geolocation accuracy below
Retargeting Agility	Acceleration: 1.43 deg/s/s Rate: 3.86 deg/s Time to Slew 200 km: 10 sec
Onboard Storage	2199 Gb solid state with EDAC
Communications	Image and Ancillary Data: 800 Mbps X-band Housekeeping: 4, 16 or 32 kbps real-time, 524 kbps stored, X-band Command: 2 or 64 kbps S-band
Max Viewing Angle / Accessible Ground Swath	Nominally +/-45° off-nadir = 1651 km wide swath Higher angles selectively available
Max Contiguous Area Collected in a Single Pass (30° off-nadir angle)	Mono: 138 x 112 km (8 strips) Stereo: 63 x 112 km (4 pairs)
Revisit Frequency (at 40°N Latitude)	1.1 days at 1 m GSD or less 3.7 days at 20° off-nadir or less (0.52 m GSD)
Geolocation Accuracy (CE90)	Specification of 5.0 m CE90 at less than 30° off-nadir, with predicted performance in the range of 4.6 to 10.7 m (15 to 35 ft) CE90, excluding terrain and off-nadir effects With registration to GCPs in image: 2.0 m (6.6 ft)

2. SHOALS Bathymetry

In order to properly assess the results obtained with the WKB algorithm, a comparison to ground truth depths was necessary. LIDAR bathymetry, obtained for the purpose of coral reef mapping by JALBTCX using the CHARTS system, is provided as ground truth. The survey was conducted in 2000 using an Optech, Inc., SHOALS-3000 LIDAR instrument integrated with an Itres CASI-1500 hyperspectral imager. SHOALS capabilities meet U.S. Army Corps of Engineers Hydrographic Survey accuracy requirements for Class 1 surveys and the IHO nautical charting standards for Order 1. The positional accuracy was +/- 3 m in the horizontal and +/- 15 cm in the vertical with a resolution of 0.00000001 degrees in latitude and longitude and 0.1 m in depth (JALBTCX, 2011).

For comparison, it is preferable to have recent data to ensure that the bathymetry has not evolved. The SHOALS data are the most recent available for the area of interest and was collected over 10 years before the satellite pass that produced the images analyzed in this study. This may be a source of error, depending on bathymetric evolution during this interval. Another potential source of comparison error is UTM coordinate in-accuracies, causing slight differences in the pixel locations between the two data sets. Another consideration is the bathymetry derived from the satellite data set includes tide effects, whereas the SHOALS data are referenced to mean lower low water (MLLW). The satellite data must be corrected to account for tide height. According to National Oceanic and Atmospheric Administration tide tables, the tide varied between 0.06 m at low tide and 0.50 m at high tide on March 31, 2011, and was approximately 0.37 m above MLLW at Waimanalo Beach at the time of the collection.

3. WKB Algorithm

The WKB algorithm is a patent-pending method for generating maps of nearshore depth and surface currents from a variety of imaging inputs from various platforms (Abileah, 2011). As of December 11, 2011, it is composed of almost 100 subroutines written in MathWorks' MATLAB software and is a work in progress with several updates planned over the coming months.

Figure 9.   STK snap shot of WorldView-2 collection pass.

C.   METHOD

The imagery was collected at about 2200Z on March 31, 2011, by the WorldView2 satellite. A Satellite Tool Kit (STK) snap shot shows the geometry part way through the collection (Figure 9). The satellite is viewing a swath of the southeast tip of Oahu and the adjacent ocean from the west looking toward the east in the direction of the sun, which is the ideal geometry for high signal-to-noise ratio (SNR) as long as the sun glint cone is avoided. The fact that the waves are propagating east to west toward the sensor also improves SNR. The scene is mostly cloud-free over the water and has adequate ocean waves present, both necessary conditions for WKB. The Waimanalo Beach area, covered by zone 8 in the SHOALS bathymetry (Figure 10), was chosen as the test area.

The imagery consists of two sets of three pairs of panchromatic and multispectral images taken approximately 10 seconds apart, and was obtained from DigitalGlobe via

the National Geospatial-Intelligence Agency. The images were provided in Basic 1B, ortho-ready format and geographic latitude-longitude coordinates. An example image from the multispectral set is shown in Figure 11. The images were orthorectified and converted to UTM coordinates for the WKB algorithm. A summary of the multispectral images is given in Table 3. To take advantage of their ability to increase wave contrast by reducing subsurface noise and atmospheric path radiance, the red and near-infrared bands (5 through 7) are used for the bathymetry extraction. The panchromatic images, which are not listed in the table, have the same metadata; however, the filenames contain a "P" rather than an "M."

Figure 10.   SHOALS 2000 survey of Oahu (From JALBTCX, 2011).

The images are pre-processed prior to entering the WKB algorithm by cropping to a user-defined size, loading the cropped images into a data cube, verifying the time interval between successive images in the set, registering the images to each other, conducting a deep water spectral analysis, and determining which pixels are water and

which are not. Then the program conducts a WKB extraction on the data bundle(s) using the specified tile size(s) (this determines the horizontal resolution of the resulting depth and current fields).

Table 3.   Summary of image files.

Image Name	First Line Time	Mean Sat Az	Mean Off-nadir View Angle	90-mean Sat El	meanSatE1
Set 1					
11MAR31215059-M1BS-052517305060	21:50:59	311.80	38.5	44.2	45.8
11MAR31215109-M1BS-052517305010	21:51:09	306.10	37.4	42.8	47.2
11MAR31215119-M1BS-052517305030	21:51:19	300.00	36.5	41.8	48.2
Set 2					
11MAR31215155-M1BS-052517305050	21:51:55	276.30	35.9	41.0	49.0
11MAR31215204-M1BS-052517305040	21:52:05	270.10	36.4	41.7	48.3
11MAR31215214-M1BS-052517305020	21:52:14	264.20	37.2	42.7	47.3
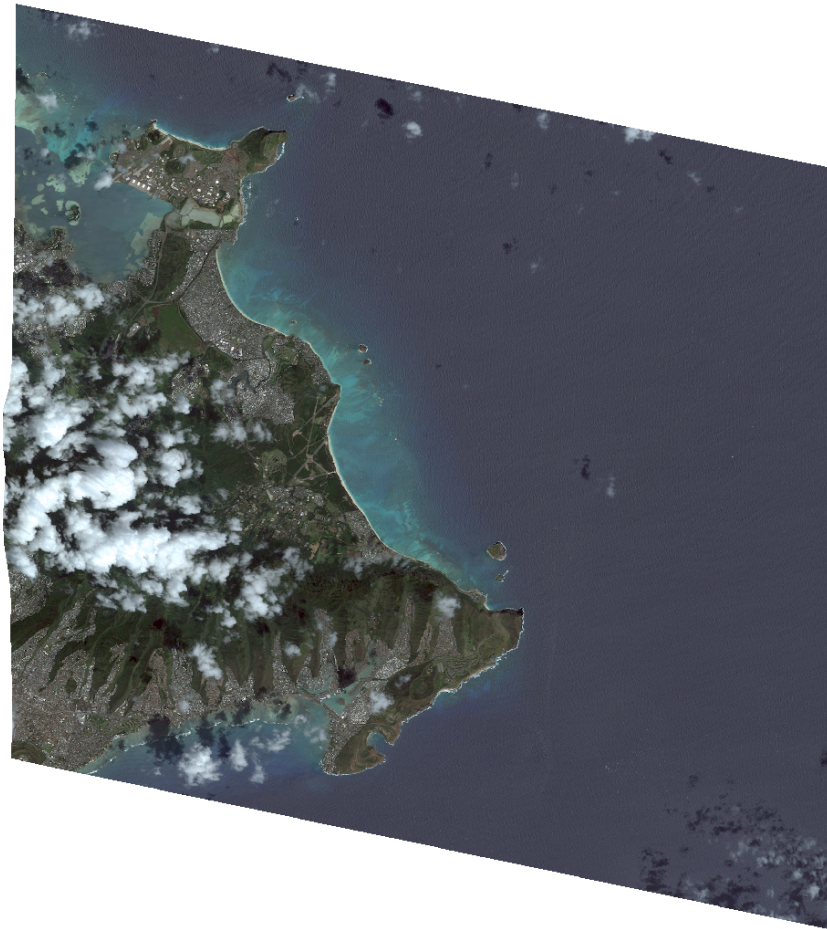
Figure 11.   Example WorldView-2 multispectral image.

1. Pre-Processing

The pre-processing ensures the images are ready for the WKB algorithm. The current version is described, but it need not be done exactly as it is today. The multispectral and panchromatic image sets are processed separately. First, the image files in each set are inventoried. At least two are required and can be multispectral or panchromatic (but they have to be the same type with the current version).

A graphical user interface (GUI) allows several user inputs to be entered during the process. The area for processing is defined by cropping a Google Earth picture (Figure 12). The cropped images are then loaded into analysis data cubes (one for each set) at a down-sampled resolution that increases efficiency but still resolves the smallest waves so as to not lose any wave energy (3 m for the multispectral and 1.5 m for the panchromatic data). During the loading process, the images are stitched together to create full scenes if they were partitioned into smaller strips by the vendor (such was the case with this imagery).
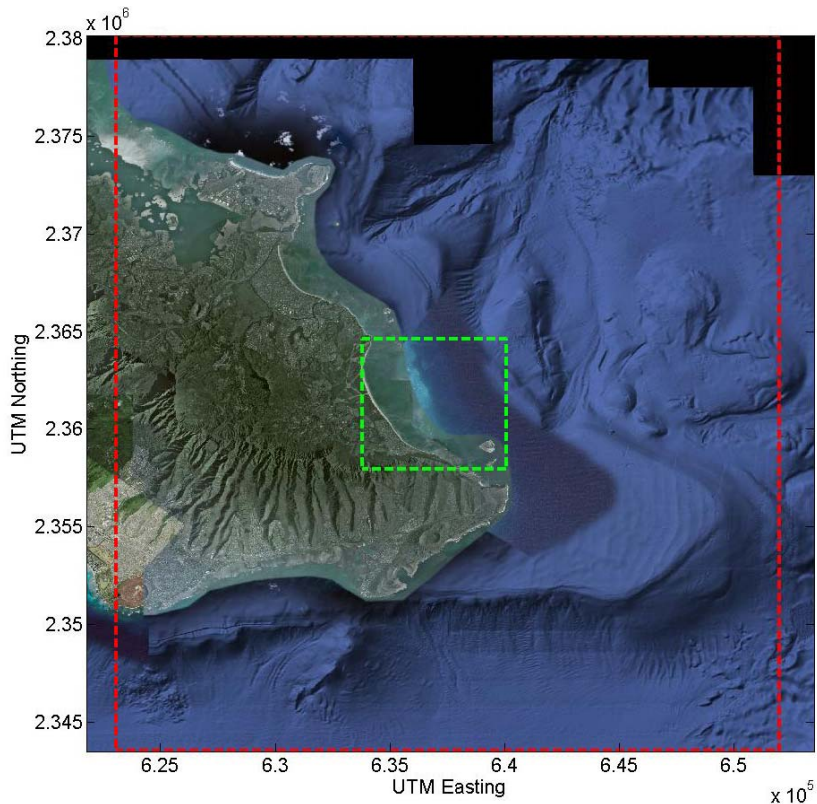
Figure 12.   Example cropped area (in green).

24

To get the timing precisely correct for the wave propagation, the time each scan line was imaged is determined, based on the first line time and the scan rate in the image metadata. Without accurate timing, wave speed will not be correct and the resulting calculations for both current and depth will be off.

Image registration is performed using fixed land features to properly align the image frames with each other. The area chosen should be close to sea level and have buildings or other fixed structures in it (Figure 13). Registration calculates the mis-registration and shifts the images to ensure the pixels at the same geographic location on each image are overlaid on top of the each other, to within sub-pixel accuracy. The panchromatic images are used to compute the registration shift because of their higher resolution, but the multispectral could also be used if panchromatic imagery is not available. The multispectral images are shifted by the same amount as the panchromatic ones. It should be noted that, if the registration is off slightly, it will simply lead to a current bias that does not impact the bathymetry determination.

Figure 13.   Registration GUI

A deep water box is then analyzed to determine the time interval between images and to compare the spectra of the multispectral and panchromatic sets (Figure 14). The interval is calculated using the fact that, per the dispersion relation as applied to deep water, wave speed is constant for a given frequency. Therefore, it is important to pick a spot where depth is at least half of a wavelength of the primary waves to get an accurate time interval (usually about 50 m). This calculation would be unnecessary if the timing metadata were more precise. It is important to determine the timing very precisely for the wave speed calculation. The interval timing is combined with the time offset determined earlier to obtain very accurate time spacing for pixels in different images. Other analyses are conducted with regard to radiance that are not important for this work, but may be of interest to researchers using radiometric techniques.
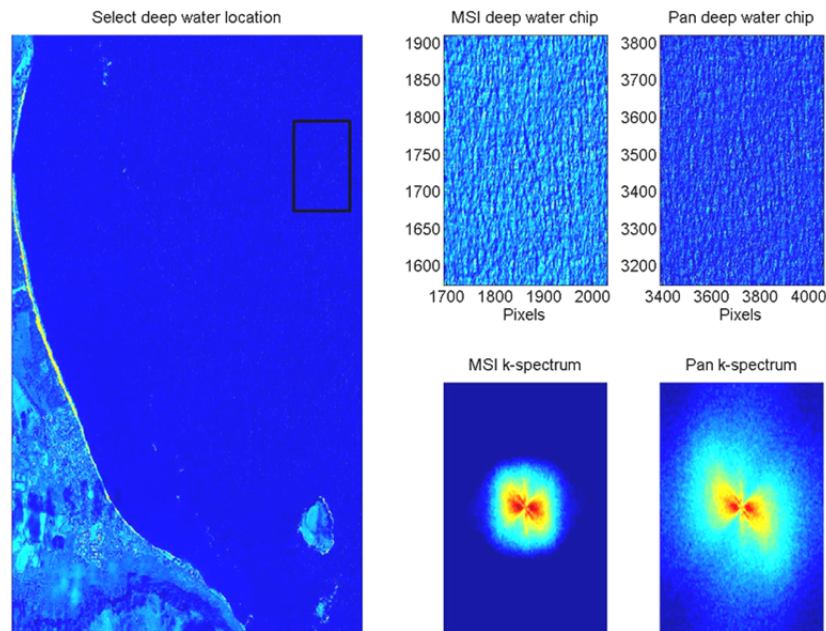
Figure 14.   Deep water analysis

The final pre-processing function creates a mask that prevents pixels that are not water from being included in the spectral analysis (Figure 15). The various bands of the multispectral images are compared to determine if a pixel most likely contains land, water, clouds, a boat or some other interfering phenomenon. With the "bad" pixels

removed, and all the other adjustments made during pre-processing, the images are ready to go into the WKB algorithm for extraction of the bathymetry.

2. WKB Extraction

WKB is rooted in the fact that surface gravity waves decrease in speed as they move to shallower depths, according to the linear dispersion relation given by Equation 1. By capturing images of ocean waves at short, precisely known time intervals, their horizontal displacement can be observed and celerity calculated. Depth is inferred from the dispersion relation. WKB becomes less useful in the cases where depths approach the height of the waves, such as in the surf zone (due to non-linear effects that are not incorporated in the linear dispersion relation); and where depths are greater than half the wavelength of the longest detectable waves (the region where wave speed is independent of depth).
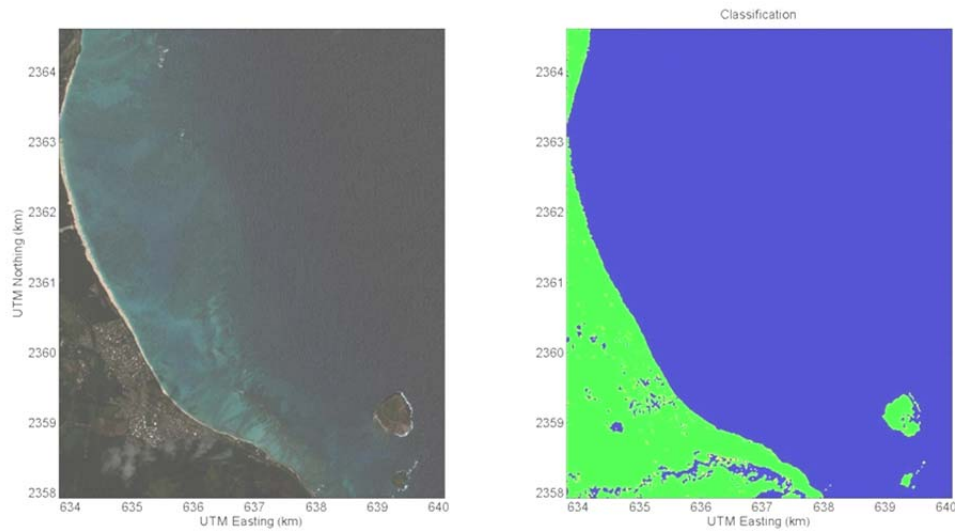
Figure 15.   True color image (left) with corresponding land mask (right)

The key to extracting bathymetry from the information contained in the images is the Fourier transform. Most commonly, 3-D Fourier analysis is applied to transform

27

image data from two-dimensional space-time into wavenumber-frequency spectra. This technique requires long time series lengths, or dwell times ~100 seconds (Dugan et al., 2001a).

Two-dimensional Fourier analysis is more appropriate for satellite imagery, which, due to the rapidly changing geometry, has effective dwell times equal to the time between images. The 2-D analysis allows for these much shorter ~10 second dwell times without adversely increasing the error. This is because the depth accuracy does not depend on dwell time so the frequency resolution is not relevant (Abileah & Trizna, 2010). In this case, the 2-D data are transformed into 2-D wavenumber spectra. In both methods, the image is broken into 2-D tiles, the dimensions of which are driven by a compromise between maximizing spatial resolution and minimizing depth error (Abileah, 2011). Tiles that are too small provide better resolution at the expense of depth accuracy. Large tiles produce better accuracy, but resolution suffers since one depth is calculated per tile.

The 2-D algorithm, a modification of which is applied in this study, applies a propagation kernel to the 2-D Fourier transforms of the N images $\{S_1(\bar{x}), S_2(\bar{x}), ..., S_N(\bar{x})\}$, $F_n(\bar{k}) = \Im_2[S_n]$. The propagation kernel moves the waves forward or backward in time and is defined as,

$$\Phi_{\pm}(k_x, k_y \mid d, \bar{u}) \equiv e^{\pm i\omega_0(k_x, k_y \mid d, \bar{u})\tau}, \tag{11}$$

where d is depth, $\bar{u}$ is the surface current, τ is the time interval between compared images, and k_x and k_y are the x and y components of the wavenumber. The sign in the exponent determines whether the waves propagate forward or backward. The term $\omega_0(k_x, k_y \mid d, \bar{u})$ in the exponent comes from the linear gravity wave dispersion relation in this form:

$$\omega_0(\bar{k} \mid d, \bar{u}) = \sqrt{g \mid k \mid \tanh(\mid k \mid d)} - \bar{k} \cdot \bar{u}, \tag{12}$$

28

which also accounts for modification of the waves by ocean currents. Using the propagation kernel, the Fourier transform at time *n* is related to the next at time *n+m* by

$$F_{n+m} = \Phi_{\pm}^m F_n \ \text{(Abileah \& Trizna, 2010).} \tag{13}$$

Wave energy in the transform space tends to be distributed along a dispersion surface and the depth and current can be found by finding the best fit of the dispersion formula to this measured power spectrum. One way to find the best fit is by minimizing the difference between successive Fourier transforms by tuning the propagation kernel to the correct depth and current. Mathematically, this is done by minimizing the objective function

$$\arg\min_{d,\bar{u}} J_\Delta = \sum_{k_x,k_y} W(\bar{k}) \sum_{n=1}^{N-m} |F_{n+m} - \Phi^m F_n|^2 \tag{14}$$

where $W(\bar{k})$ is a weighting filter that increases the accuracy of the solution by increasing the SNR. It does this by masking much of the background noise by keeping those wavenumbers where the wave energy is concentrated and eliminating those where it is not. Since waves are located where the energy adds coherently in wavenumber space when the images are propagated to the same time, this determination is done by seeing for which wavenumbers this is true. The objective function also includes a provision for more than two image pairs by including a summation over frame intervals, *m*, from *n* = 1 to *N-m* (Abileah, 2011).

A patent-pending technique, which is a modification of the 2-D algorithm, overcomes the accuracy-resolution compromise discussed above by adding a 2-D inverse Fourier transform operation, $\Im_2^{-1}$, to the objective function (Abileah, 2011). By transforming the data from wavenumber space back into spatial coordinates, a depth is obtained for every image pixel rather than for every tile. In fact, it eliminates the need to tile the images, although this has not yet been incorporated into the code. To expedite implementing the new method, the existing code was modified rather than generating new code, which is computationally inefficient but yields the same results. A more efficient revision is forthcoming.

Besides better spatial resolution and less computation time, another benefit of the new method is it is less susceptible to interference from non-water pixels because, unlike in wavenumber space, in spatial coordinates the waves can be separated spatially from the interfering phenomena.

As before, the 2-D Fourier transform is applied to the (in this case, tiled) images, converting them into 2-D wavenumber spectra. (New implementations can forgo the tiling step; however, tiling may still be desired to take advantage of the multiple processors in parallel computing settings.) Minimizing the revised objective function:

$$\arg\min_{d,\bar{u}} J_\Delta(\bar{x}) = \left| \mathfrak{I}_2^{-1} \left[W(\vec{k})(F_1(\vec{k}) - \Phi^{-1} F_2(\vec{k})) \right] \right|^2 , \tag{15}$$

again by tuning Φ, produces the best depth and current solution for each x (Abileah, 2011).

Although W eliminates much of the noise, some is still present after the filtering. To further improve the results, a sliding window $A(\bar{x})$ is applied. The window size can be adjusted as necessary to improve SNR; however, a larger window will reduce resolution, but not to the degree the tiles did in the old method. With the appropriate $A(\bar{x})$, spatial resolution with the new method can be 10 m (Abileah, 2011). The code implemented herein used 250 m tiles with 50% overlap, creating an effective spatial resolution of about 125 m.

For instances where more than two images are available, SNR can be increased further by averaging across the images, $n = 1$ to N-m, not unlike in the old method. For data sets with long interval times, and as was done for this study with 10 seconds between images, consecutive images are used, meaning $m = 1$. Still another improvement through averaging is to sum over a set of interval spacing values, M, so multiple image separation options are available. The final, general form for the objective function that includes all these possibilities is (Abileah, 2011):

$$\arg\min_{d,\bar{u}} J_\Delta(\bar{x}) = \sum_{m \in M} \sum_{n=1}^{N-m} \sum_{A(\bar{x})} \left| \mathfrak{I}_2^{-1} \left[W(\vec{k})(F_1(\vec{k}) - \Phi^{-1} F_2(\vec{k})) \right] \right|^2 . \tag{16}$$

Choosing an *m* other than one creates comparisons of images that are not consecutive. Since this increases the time interval between compared images, effectively decreasing the sampling rate, it should be done with the following consideration in mind. In wavenumber space, a phase shift is equivalent to wave displacement in spatial coordinates. Using Equation 11, the measured phase shift leads to the depth result obtained with Equation 16. In theory, a very small time interval is all that is necessary to determine the phase shift. In the real ocean, where noise complicates the wave signal, however, a longer time is required to accurately measure the phase shift amidst the background noise. On the other hand, too long of an interval allows the waves to become less coherent as they become modified by wind, refraction, bottom friction, etc. Therefore, a time interval of at least one second, but not more than several seconds, is a good compromise. Ideally, the 10-second interval time between the images in this study should be shorter to ensure less wave modification. With this in mind, an *m* larger than one would only be appropriate for data sets having image interval times (or sampling times) of one second or less between images. This can also be extended to using sets of different values of *m* (Abileah, 2011).

There are a couple of ways to implement the objective function tuning, which involves searching for the depths and current speeds that minimize Equation 16. One method attempts this by trying every possible combination of depth and current speed. This option is computationally intensive since it has to loop through three variables, depth and both the x and y components of the current velocity, in computing the propagation kernels for use by Equation 16 (Abileah, 2011).

Another way to do it that reduces the computation time significantly (and the way the current revision accomplishes it) is to separate the current search from the depth search. To do this, a low wavenumber filter is applied to isolate the higher wavenumbers (short wind waves) because they are effectively deep water waves and unaffected by depth. This removes the need to include depth in the first search and allows any deviation from the dispersion relation predicted wave propagation to be attributed to the current. Once the current is known, the images are shifted, similar to the registration

31

process, to remove any wave displacement caused by the current. Then the search for depth is done to complete the solution (Abileah, 2011).

Of note, in execution of Equation 13, the current code does not propagate the waves in one image to the time of the other image being compared. Rather, it propagates the waves in both images, one forward and one backward, to the time half-way between the two (Abileah, 2011). This was done purely for cosmetic reasons.

The output of the WKB program includes several figures, some of which are shown above, a diary that contains a chronological account of the program's operations, image registration movies that show the shift being applied to the images, and image data cubes that contain the image data at various stages of the process. The main output figure is a quad chart that displays wave direction on the top left, a true color multispectral image of the area processed on the top right, the extracted bathymetry on the bottom left, and the extracted ocean currents on the bottom right (Figure 16). Another key figure, which will be discussed in Chapter IV, shows how the WKB derived bathymetry compares to the SHOALS bathymetry.
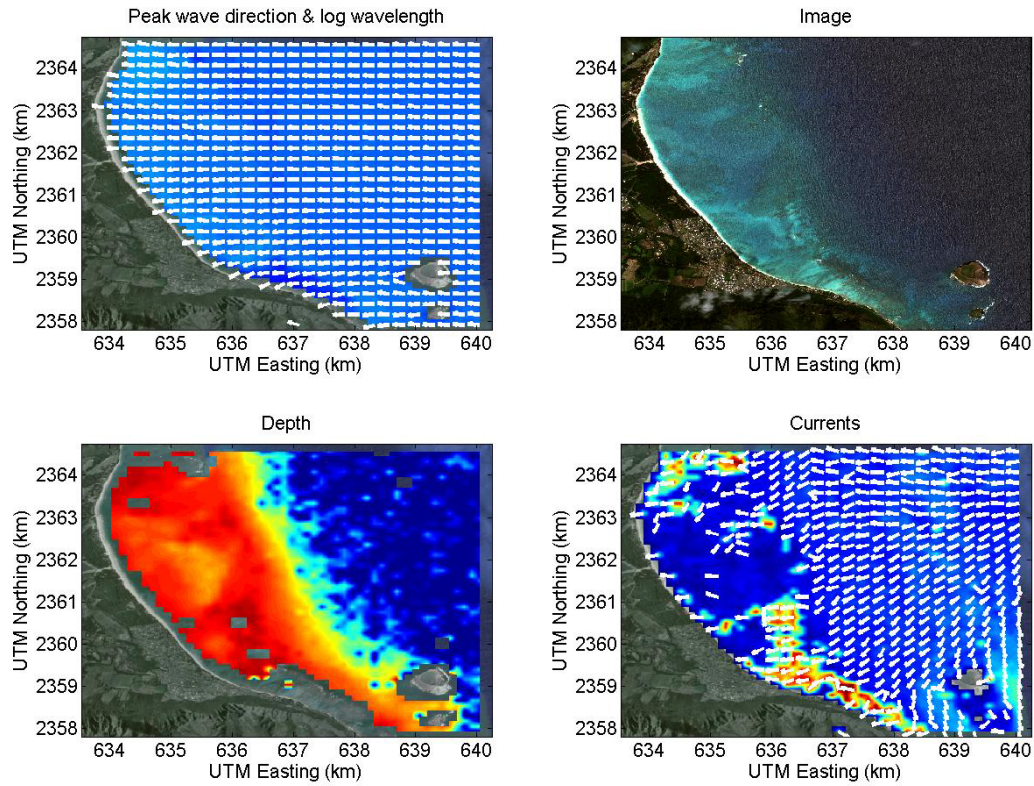
Figure 16.   Image Set 1 case 3MSI WKB output showing wave direction (top left), a true color image (top right), extracted bathymetry (bottom left), and extracted ocean currents (bottom right)

THIS PAGE INTENTIONALLY LEFT BLANK

IV. ANALYSIS RESULTS

A. GENERAL APPROACH

For the comparison analysis of WKB extracted bathymetry to SHOALS bathymetry, two data runs were conducted by ingesting two different image sets into the WKB algorithm. The first set consisted of the first three multispectral images in Table 3 and their corresponding panchromatic images, while the second set consisted of the last three multispectral images and their corresponding panchromatic images. While it was not practical to make the user-selectable items identical between runs, the cropped area of interest, registration box, and deep water box were carefully chosen to minimize differences between the two sets. This way, any differences in the results would be mostly attributable to differences in the images.

Four cases were produced in each of the two data runs, two using multispectral images and two using panchromatic images. The four cases, named for how many of each type of image were ingested, are: two multispectral images (2MSI), three multispectral images (3MSI), two panchromatic images (2Pan), and three panchromatic images (3Pan). For the two-image cases, the first two images in each set were the ones ingested.

The WKB extracted depth fields were compared to the SHOALS bathymetry using side-by-side area maps. These figures show the SHOALS map on the left and the WKB map on the right and allow a quick visual comparison of the WKB field with ground truth field (Figure 17).

East-west transects were chosen to investigate a few sample cross-sections for each case. For each transect, the WKB depth is plotted with the SHOALS depth as a measure of the similarity between them along the east-west slice. The depth error is calculated for each transect, as well. This graph aids in identifying where along the transect the greatest deltas are located. A third graph for each transect is the relative depth error, which shows depth error as a percentage of depth. This allows visualization of where the error has more or less significance (Figure 18).
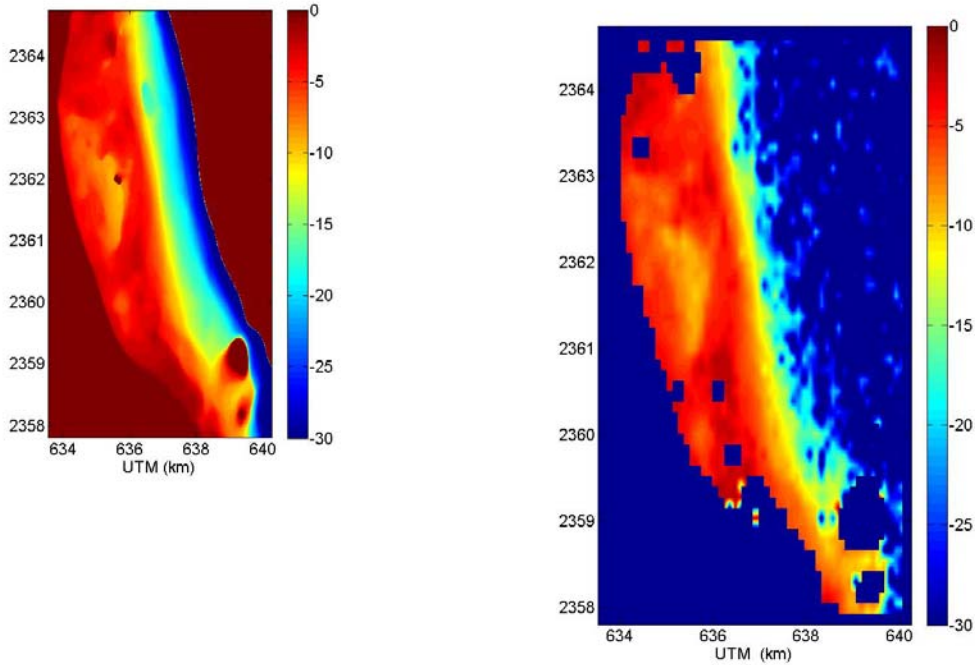
Figure 17.   Comparison maps of SHOALS (left) and 3MSI WKB for Image
Set 1 (right)

In addition to transects, each case was analyzed using all the valid depths in the
entire subject area. Scatter plots show the distribution of the data and their correlation.
Since the data field consists of millions of points, resulting in saturated plots, the data
were thinned out by picking out every thousandth point to plot. The plots specify the
slope of the linear regression line, its y-intercept, and R^2, the square of the correlation
coefficient for the SHOALS-observed and WKB-predicted values.

The regression line slope and R^2 are indicators of WKB performance. If WKB
were perfect, its depths would be exactly correlated to the SHOALS depths, which would
yield slope and R^2 values of 1.0. The less perfectly WKB performs, the less correlated
the WKB and SHOALS depths will be, and the further these values decrease from 1.0.
The scatter plots have a second panel that filters out all SHOALS depths greater than 15
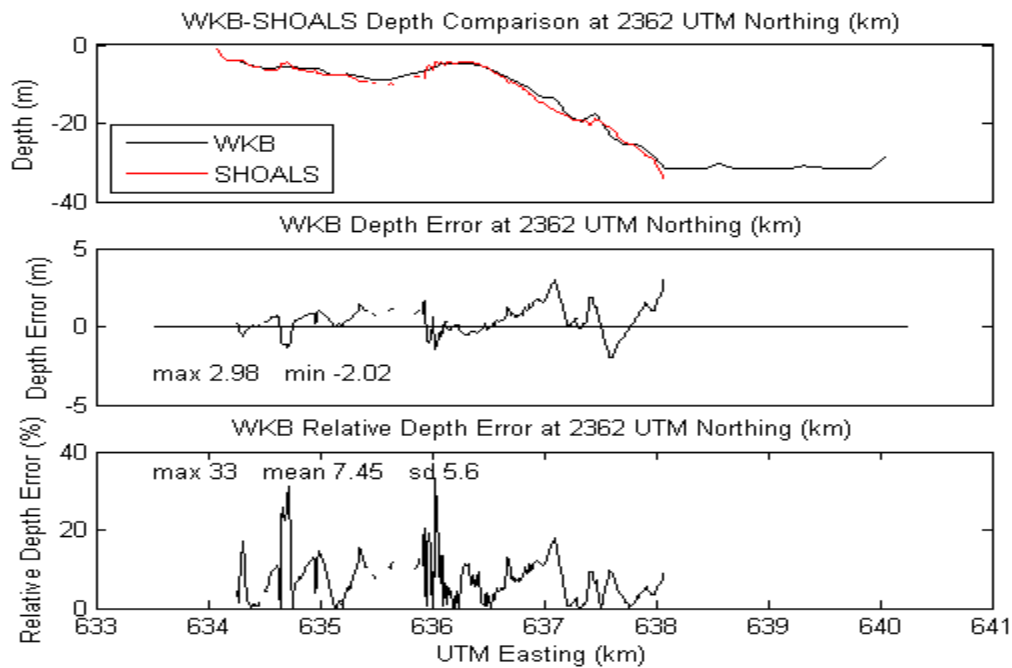m, for reasons discussed later (Figure 19).

36

Figure 18.　　Transect from Image Set 1 case 3MSI showing WKB depth plotted with SHOALS depth (top); the difference between them, or depth error (mid); and depth error as a percentage of depth, or relative depth error (bot)
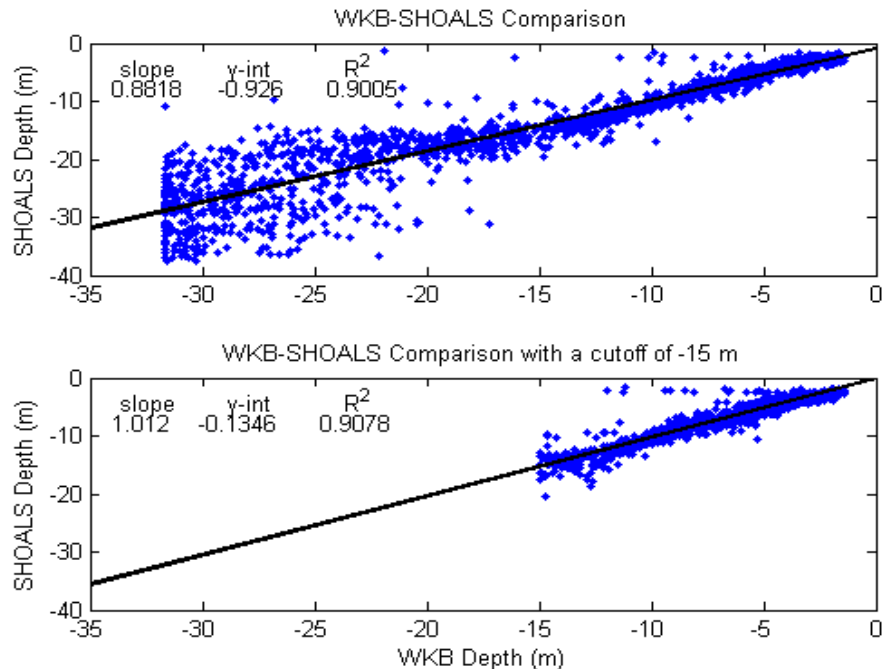

Figure 19.　　Scatter plot from Image Set 1 case 3MSI showing thinned data for all depths (top) and for just depths less than 15 m (bottom)

In addition, a bar graph was produced that shows, for each case, the mean error for several depth partitions, or bins. The bins are one to 2 m, followed by every 2 m up to 20 m, with the last bin including all depths greater than 20 m. This aids in determining at which depths the algorithm worked better (Figure 20).
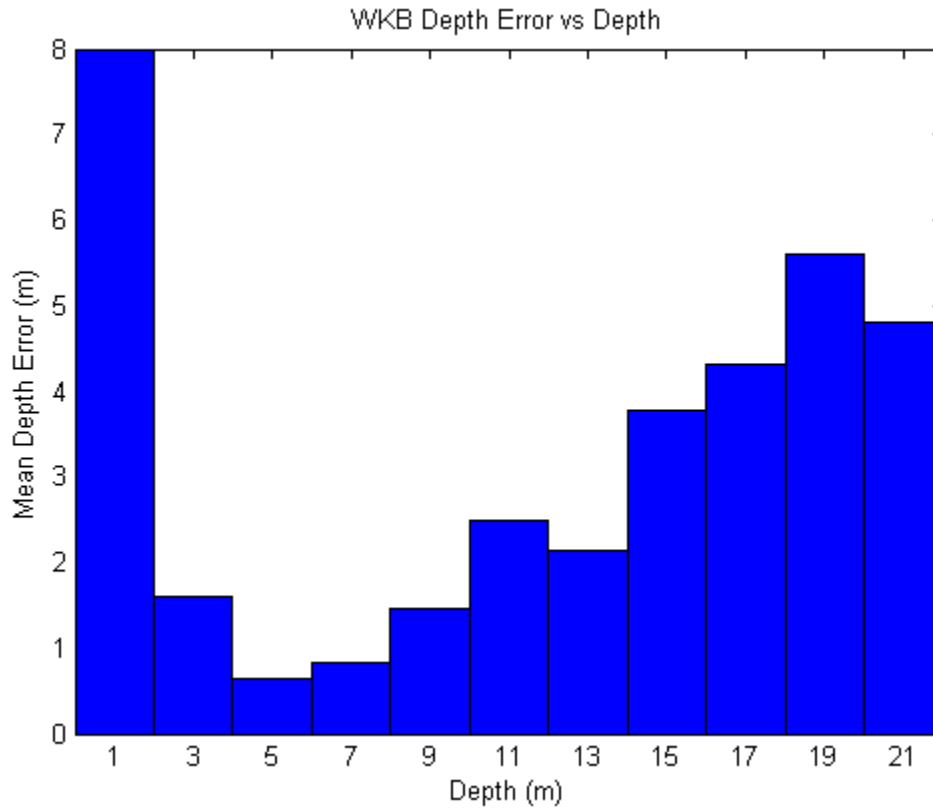

Figure 20.   Bar graph from Image Set 1 case 3MSI showing the mean depth
error for several depth bins

B.   IMAGE SET 1

A quick glance at the comparison map for 3MSI (Figure 17) shows that, overall, WKB did a good job of depicting the main bathymetric features, such as the elongated trough (yellow feature) near the center of the map and the shallower spots to the south of it (dark red). The abrupt, steeper slope beyond the more gently sloping beach is also well depicted where the red quickly turns yellow a couple of kilometers from the beach.

Image Set 1 results are summarized in a line graph that consolidates the mean depth errors in the bar graphs of all four cases on one chart (Figure 21), in a table listing the mean depth error and relative error ranges for each depth bin (Table 4), and in a table listing the R^2 values for each case (Table 5). The results highlight some of the strengths and weaknesses of the method. The complete series of graphs for Image Set 1 is found in Appendix A.
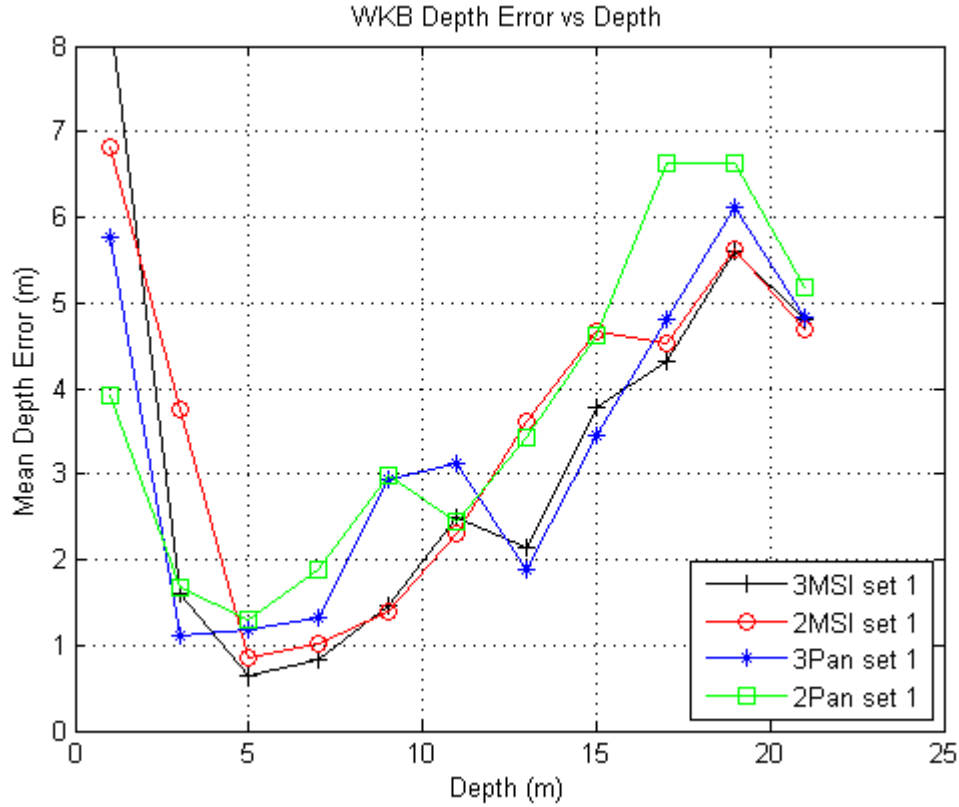

Figure 21.   Mean depth errors for all four Image Set 1 cases

Understandably, the 1–2 m bin for all cases is dominated by extremely large mean depth errors. The nonlinear processes in the surf zone render the linear dispersion relation inaccurate, and therefore, WKB less effective at predicting depths below about 2 m. To improve WKB in this regime would require it to account for nonlinearities as the depth approaches the height of the waves. This could be done by applying a correction within the linear dispersion relation (Hedges, 1976), but would still be an approximation.

Other factors contributed to error at these shallow depths, including an ambiguity caused by a sampling time that is equivalent to the period of some of the waves, and insufficient short waves for current estimation.

Table 4.   Mean depth error and relative error ranges for each depth bin in Image Set 1

Case	<2m		2-4m			4-6m			6-8m		
2MSI	6.8	341%	3.8	94%	188%	0.9	14%	21%	1.0	13%	17%
3MSI	8.4	420%	1.6	40%	80%	0.6	11%	16%	0.8	10%	14%
2Pan	3.9	196%	1.7	42%	84%	1.3	22%	33%	1.9	24%	32%
3Pan	5.8	288%	1.1	28%	55%	1.2	20%	29%	1.3	16%	22%

Case	8-10m			10-12m			12-14m		
2MSI	1.4	14%	17%	2.3	19%	23%	3.6	26%	30%
3MSI	1.5	15%	18%	2.5	21%	25%	2.1	15%	18%
2Pan	3.0	30%	37%	2.4	20%	24%	3.4	24%	29%
3Pan	2.9	29%	37%	3.1	26%	31%	1.9	14%	16%

Case	14-16m			16-18m			18-20m			>20m	
2MSI	4.7	29%	33%	4.5	25%	28%	5.6	28%	31%	4.7	23%
3MSI	3.8	24%	27%	4.3	24%	27%	5.6	28%	31%	4.8	24%
2Pan	4.6	29%	33%	6.6	37%	41%	6.6	33%	37%	5.2	26%
3Pan	3.5	22%	25%	4.8	27%	30%	6.1	31%	34%	4.8	24%

Table 5. R^2 values for Image Set 1

Case	R^2	$R^2 < 15\,m$
2MSI	0.8681	0.8909
3MSI	0.9005	0.9078
2Pan	0.8603	0.8453
3Pan	0.905	0.911

Another limitation occurs at the other end of the depth field, where mean depth errors were relatively high. At depths greater than half the wavelength, waves are not affected significantly by the bottom, so they are dispersive and the dispersion relation is not helpful for determining depth. Therefore, WKB can only determine depth up to the point where the water depth allows gravity waves to become nondispersive. If fewer longer waves are present in the wave field, this will occur at shallower depths. If longer waves are abundant, then WKB will be effective at deeper depths.

Therefore, WKB is limited on its ability to extract depth as determined by the wave spectrum detected by the sensor. In this instance, it appears that the spectrum lacks sufficient energy in waves longer than about 40 m, so that by a depth of about 16 m, the mean depth errors are consistently above 4 m with relative errors of 25% and greater. This assumption is supported by The Coastal Data Information Program (CDIP) of Scripps Institution of Oceanography, which indicates the sea on 31 March off of nearby Mokapu Point was relatively calm with very little long wave swells (Figures 22 and 23).
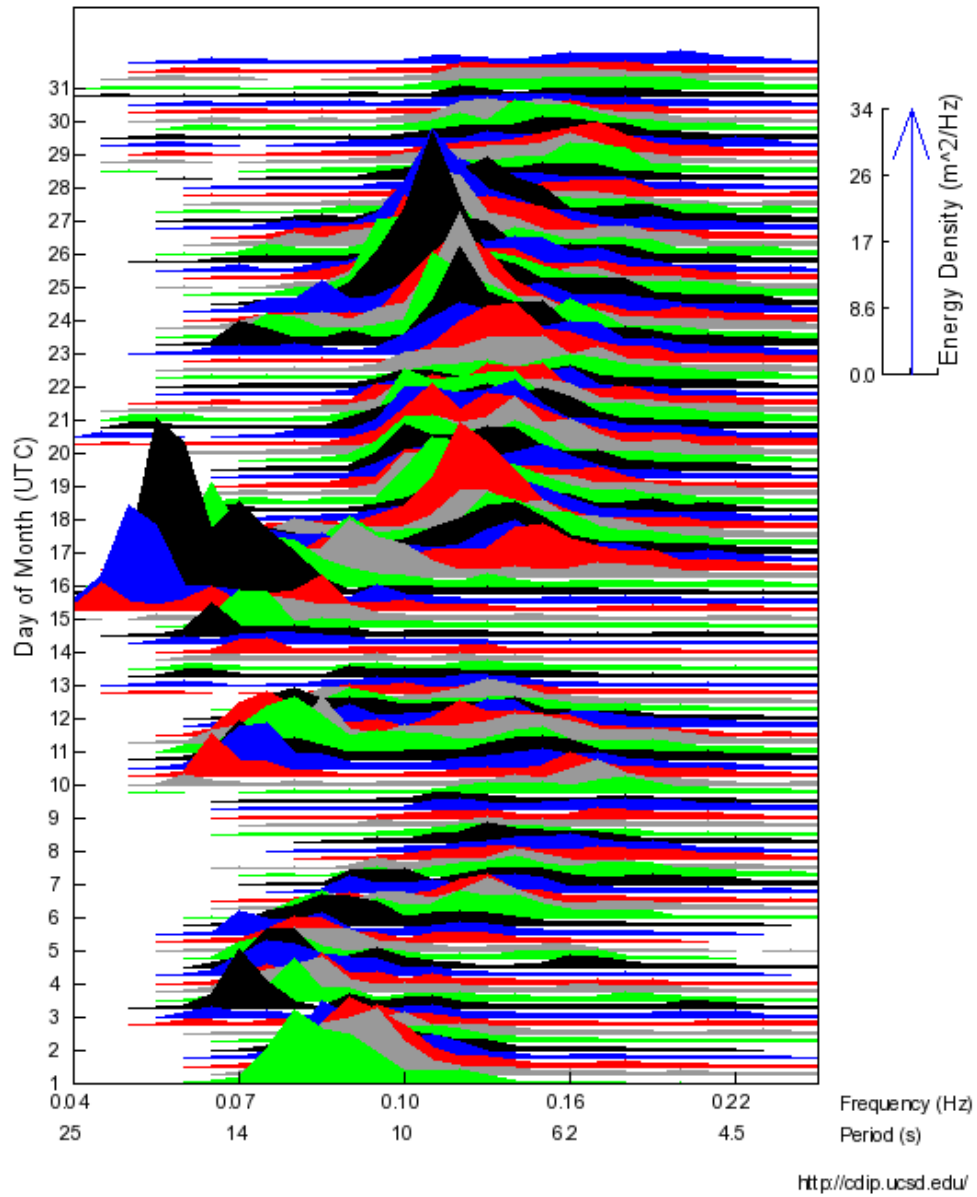
Figure 22.   Energy spectrum from Mokapu Point buoy for March 2011, showing larger swell events earlier in the month, but relatively little swell on the date of collection (31 March) (From CDIP, 2012)
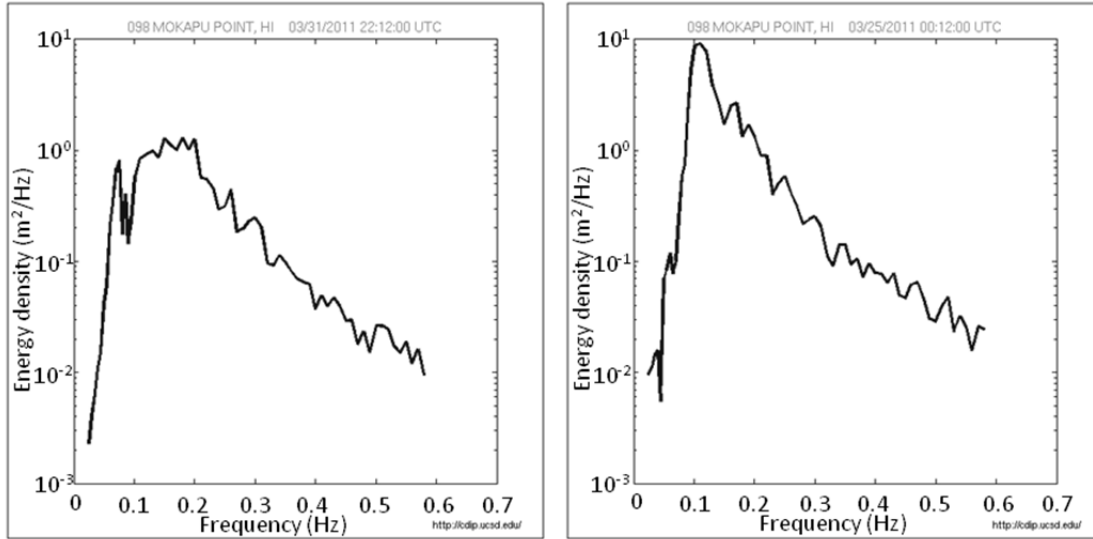
42

Figure 23.   Energy spectra from Mokapu Point buoy for the time of collection (left) and a swell event a few days prior (right), showing an order of magnitude difference in energy at the low frequencies (From CDIP, 2012)

In between these limits, performance was much better. 3MSI had the best overall performance, with a mean depth error of 1.8 m from 2–16 m, a regression line slope of 1.01 and R^2 of 91%. The next best was 3Pan with 2.1 m mean depth error, slope of 1.06 and R^2 of 91%. The two-image cases did the worst with mean depth errors of 2.5 m and 2.6 m for 2MSI and 2Pan, respectively. It was expected that the three-image cases would perform better than the two-image ones because of the averaging technique that increases SNR with multiple image pairs.   However, the multispectral outperforming the panchromatic was unexpected and is addressed shortly.

In the shallower depths outside the surf zone, the multispectral cases performed quite well. From about four to 10 m, mean depth errors were 1.5 m, or less, and relative errors were in the 10–20% range. By 10 m, the best panchromatic case (2Pan in this depth bin) did as well as the multispectral cases, all having mean depth errors of about 2.4 m and relative errors in the 20–25% range. A bit of an anomaly, this was the only instance where 2Pan was better than 3Pan. Looking at the comparison maps in Appendix A, it may be due to 3Pan doing a slightly worse job in the area west of Manana Island in the southeast corner, an area which is primarily 10–12 m in depth.

The expectation was that the panchromatic cases would outperform the multispectral cases because of their higher resolution images being able to better resolve the shorter waves leading to a more accurate current determination. This, in turn, would produce more accurate depths. A possible reason for the multispectral cases' better performance has to do with water clarity. The ocean bottom can be seen quite clearly in the shallower regions in Figure 11. This certainly added to the non-gravity wave noise in the panchromatic cases with a corresponding reduction in SNR. The multispectral cases were partially immune to this problem by screening out most of the subsurface noise by using only bands 5 through 7. What the multispectral cases lacked in resolution, they made up for in band selectivity and vice versa for the panchromatic cases. In the deeper water, where bottom radiance was less significant, the panchromatic cases did better.

In line with this reasoning, 3Pan performed the best in the 12–16 m region, edging out 3MSI by a couple tenths of a meter in depth error. Mean depth errors were about 2 m in the 12–14 m bin and 3.5 m in the 14–16 m bin for these two cases. The worse-performing two-image cases had well over 3 m errors in the 12–14 m bin and well over 4 m in the 14–16 m bin.

C.   IMAGE SET 2

Image Set 2 yielded similar results to set one, with some notable differences. Again, WKB did a good job of depicting the main bathymetric features, as seen in the comparison maps in Appendix B, where a complete series of Image Set 2 graphs are found. As was done for Image Set 1, Image Set 2 results are summarized in a line graph of all four cases that consolidates the mean depth errors on one chart (Figure 24), in a table listing the mean depth error and relative error ranges for each depth bin (Table 6), and in a table listing the R^2 values for each case (Table 7).

The same limitation in the surf zone is apparent in Image Set 2's results, with the 1–2 m bin for all cases dominated by extremely large mean depth errors. In the deeper region, although the same limitations applied to this set, better results were achieved with set two. For instance, a respectable mean depth error of 3.0 m and corresponding relative error of 17–19% was obtained by 3MSI in the 16-18 m bin. In comparison, all cases in

set one had errors well above 4.0 m and greater than 23% by 16 m depth. In fact, 3MSI performed better in the 18–20 m bin in set two than it did in the 16–18 m bin in set one. It was not until the final greater-than-20 m bin that 3MSI's performance degraded above the poorer set one values. The performance may have been aided by geometry more favorable for enhancing long wave contrast. If this was the case, the wave spectrum has a higher SNR in the long wave portion, allowing for deeper bathymetry extraction. However, this is purely speculative.
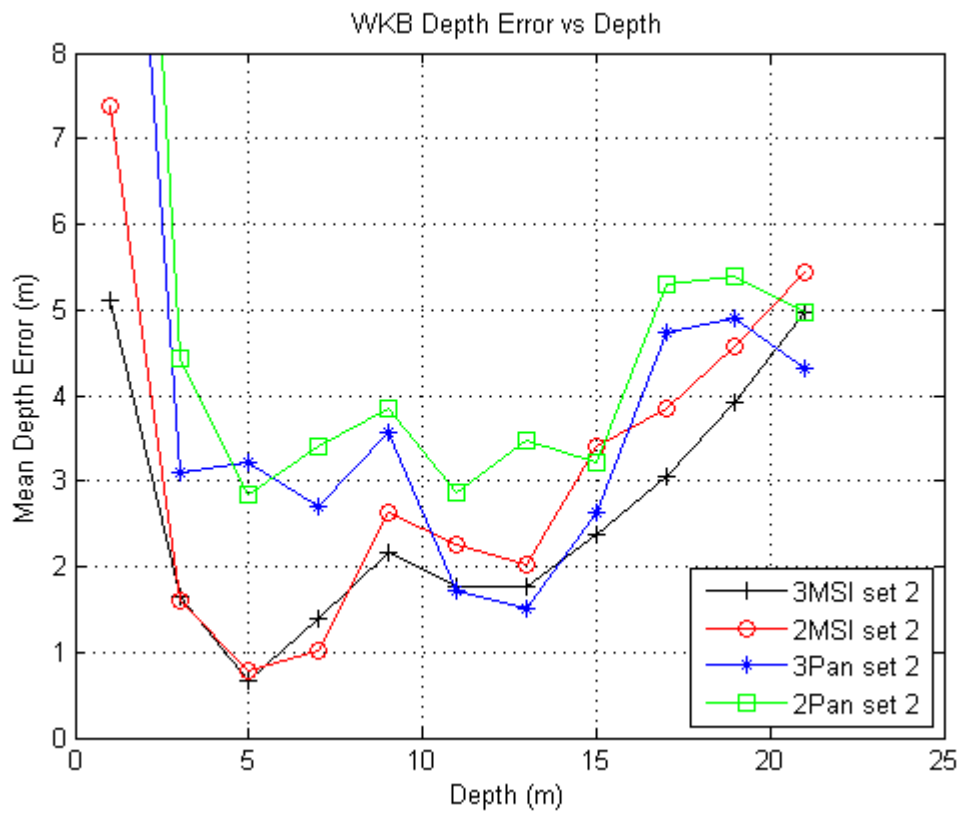
Figure 24.   Mean depth errors for all four Image Set 2 cases

As in set one, the three-image cases outperformed their two-image counterparts almost exclusively. Also like set one, 3MSI had the best overall performance in between the surf zone and the deeper limit, with a mean depth error of 1.7 m from 2–16 m, and an only slightly larger 1.9 m when expanded to include 16–18 m. Regression line slope and R^2 for 3MSI were 1.13 and 88%, respectively. The next best for set two was 2MSI, rather than 3Pan as was the case with Image Set 1. It had a mean depth error of 2.0 m for

the range of 2-16 m and similar regression line slope and R^2. The panchromatic cases did the worst this time with 2.6 m and 3.4 m for 3Pan and 2Pan, respectively. These figures are quite a bit worse than the 2.1 m and 2.6 m achieved with set one.

Table 6.   Mean depth error and relative error ranges for each depth bin in Image Set 2

Case	<2m			2-4m			4-6m			6-8m		
2MSI	7.4	369%		1.6	40%	80%	0.8	13%	20%	1.0	13%	17%
3MSI	5.1	256%		1.6	41%	82%	0.7	11%	16%	1.4	18%	23%
2Pan	18.1	903%		4.4	111%	222%	2.8	47%	71%	3.4	43%	57%
3Pan	14.5	726%		3.1	77%	155%	3.2	54%	80%	2.7	34%	45%

Case	8-10m			10-12m			12-14m		
2MSI	2.6	26%	33%	2.3	19%	23%	2.0	14%	17%
3MSI	2.2	22%	27%	1.8	15%	18%	1.8	13%	15%
2Pan	3.8	38%	48%	2.9	24%	29%	3.5	25%	29%
3Pan	3.6	36%	45%	1.7	14%	17%	1.5	11%	13%

Case	14-16m			16-18m			18-20m			>20m	
2MSI	3.4	21%	24%	3.8	21%	24%	4.6	23%	25%	5.4	27%
3MSI	2.4	15%	17%	3.0	17%	19%	3.9	20%	22%	5.0	25%
2Pan	3.2	20%	23%	5.3	29%	33%	5.4	27%	30%	5.0	25%
3Pan	2.6	16%	19%	4.7	26%	30%	4.9	25%	27%	4.3	22%

Table 7. R^2 values for Image Set 2

Case	R^2	$R^2 < 15\,m$
2MSI	0.8825	0.8858
3MSI	0.9092	0.8825
2Pan	0.8096	0.8595
3Pan	0.8627	0.8683

After examining the multispectral true color images on the top right of the WKB output figures in Appendices A and B, it is apparent that the ocean bottom appears brighter in the Image Set 2 images. This is most likely due to the difference in collection angle as the spacecraft moved over the area, with the angle becoming more favorable for bottom reflection as the pass evolved. This would have exacerbated the bottom generated noise issue for the panchromatic cases, leading to the further degradation in performance.

The individual depth bin values tell a similar story, with the multispectral cases doing considerably better than the panchromatic cases through a depth of 10 m, where mean depth errors were nominally 1–2 m better and relative errors were 10–40% better in the multispectral cases. Above 10 m, the 3Pan case performed better than the 3MSI case, with mean depth errors of 1.5–1.7 m, until 14 m depth where 3MSI took honors again. Strangely, the multispectral cases did not degrade as rapidly as the panchromatic cases above 16 m, unlike in set one where they degraded roughly equally.

THIS PAGE INTENTIONALLY LEFT BLANK

V.   CONCLUSIONS AND RECOMMENDATIONS

A.   CONCLUSIONS

A WKB algorithm was investigated to determine its effectiveness in extracting bathymetry from WorldView-2 satellite optical imagery. This initial analysis indicates that the technique described herein is promising. The analysis involved comparing WKB extracted depths to SHOALS LIDAR survey obtained depths at Waimanalo Beach in Hawaii.

The algorithm performed well in the midrange depths of 2–14 m, its best cases managing as little as 0.6 m and no worse than 2.3 m of mean depth error in any depth bin. Excluding the 2–4 m bin, relative errors for the best cases ranged from a best of 10% to a worst of 27%, with most being in the 10–17% range.   The best regression line slope achieved was 1.01 with an associated R^2 of 91%.

The best analysis results came from the use of three multispectral images, the worst results came from the use of two panchromatic images. The panchromatic cases would certainly have performed better in a more turbid water or dark bottom area, where the bottom would not have contributed to a poor wave SNR. The three-image cases did better than the two-image cases in all but a couple of instances.

There may have been some error introduced into the comparisons through a conversion of the original imagery from latitude-longitude geographic coordinates to UTM coordinates, which may have differed from the SHOALS UTM coordinates by several meters. Understanding that the bathymetry hardly changes in that amount of horizontal distance, and that the WKB algorithm produced depths at an effective spatial resolution of about 125 m, this error should be insignificant. Another, perhaps more significant, source of error is the elapsed time between the SHOALS survey and the imagery collection. During this almost 11-year period, the bathymetry may have changed, perhaps significantly in some portions.

In spite of these potential sources of error and given the fairly complex environment in which it was tested, the performance of the algorithm was notable.

Unlike many previous WKB studies, which were conducted in areas with simpler, nearly-constant sloping bottoms, often assumed cross-shore currents, and avoided wave refraction, Waimanalo Beach has fairly complex bottom topography, intricate surface currents, and noticeable wave refraction.

WKB is limited in its ability to do depth extraction in the surf zone (less than about 2 m) and beyond some deep limit determined by the surface wave spectrum. In this case, the lack of long wave swells limited WKB's ability to determine depth satisfactorily to approximately 15 m. A scene with more long wave swells in it probably would have produced more accurate depths out to 20 m or more.

B.   RECOMMENDATIONS FOR FUTURE WORK

The WKB algorithms and codes are still evolving. Continuing work will determine whether these changes improve the algorithm's results. Among the newly implemented updates is the fusion of panchromatic and multispectral images into the same depth extraction routine, whereas they were calculated separately before. This allows the algorithm to take advantage of the strengths of each image set, using the higher resolution panchromatic images for the current determination and the bands of the multispectral images that create the best SNR to determine the depth.

The code based on the tiling approach, used here, was recently replaced with code that makes the algorithm more computationally efficient with the non-tiling method. One way to really capitalize on this is to introduce parallel processing into the process. This would significantly speed up the computing time for larger areas and more image pairs.

Future improvements include: a wave contrast metric to help identify when contrast has played a role in the results; better logic to improve performance with multiple image pairs; a way to flag extremes and replace them with appropriate values to eliminate unreasonable depth conclusions in the surf zone or at the deep limits; and accuracy and spatial resolution improvements.

In addition to testing algorithm improvements, future work could investigate different combinations of multispectral bands to see which produces the best results by

better isolating the waves from the background. Perhaps principle component transforms of the images can be applied to increase wave visibility and SNR.

Improvements in data collection could also be explored. For example, reducing the time interval between subsequent image pairs would reduce wave propagation and the change in view angle from one image to the next. This will help with accuracy by reducing the opportunity for the waves to be modified by sources other than depth (making the dispersion relation a more exact predictor of the wave motion) and by allowing the multiple-image-pair averaging technique to have more success. It would also alleviate the ambiguity issue associated with sampling at the same time interval as the period of a bulk of the waves.

There are other ways to realize the last two gains if reducing the image collection time interval becomes too difficult. By incorporating a view-angle transfer function to account for the change in angle, the averaging technique could still produce improvement when averaging the image pairs. The ambiguity problem can probably be overcome with a better algorithm to more effectively deal with it.

Finally, better choices in the imagery product could improve future efforts. Receiving the imagery in the UTM format that WKB requires would eliminate the need to convert it, avoiding any error introduced in the process. Obtaining accurate timing details from the vendor to establish more precisely when each image line was scanned will remove the need to estimate during the pre-processing. While the estimation is good, knowing the timing exactly will help improve WKB accuracy.

THIS PAGE INTENTIONALLY LEFT BLANK

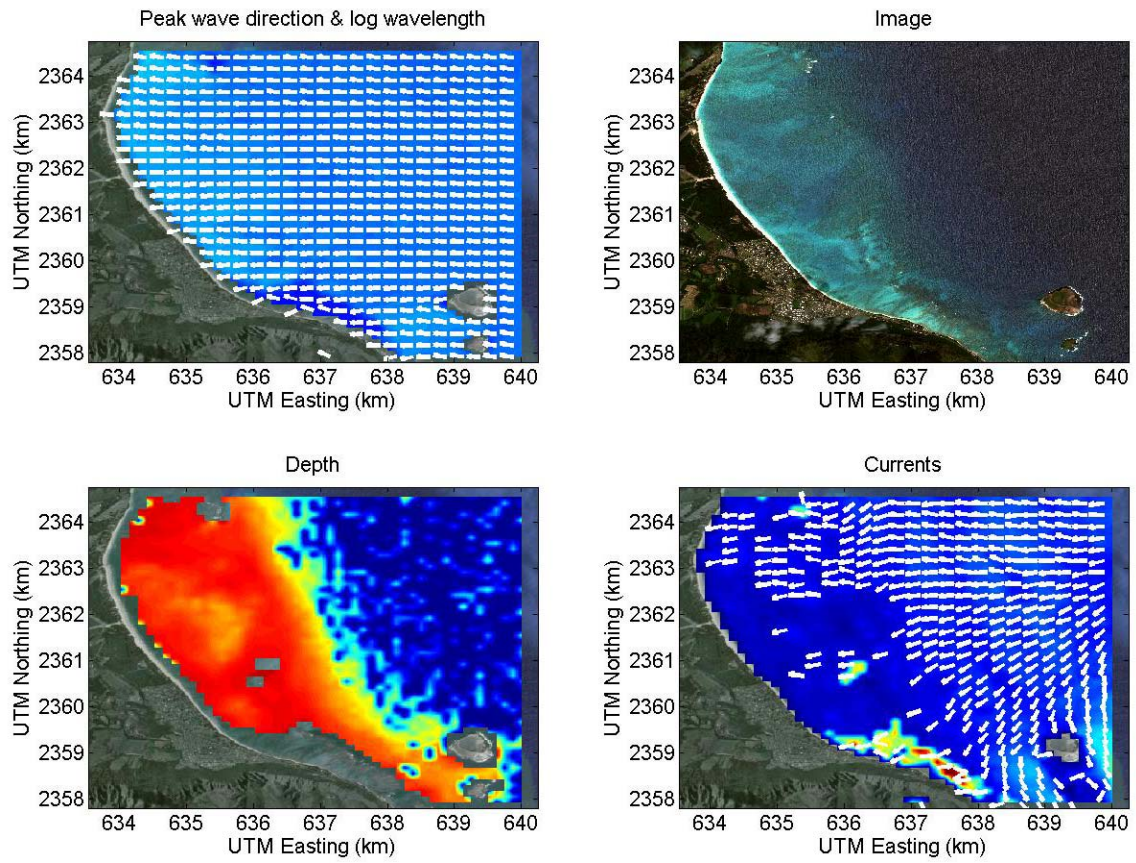# APPENDIX A. IMAGE SET 1

CASE: 2MSI
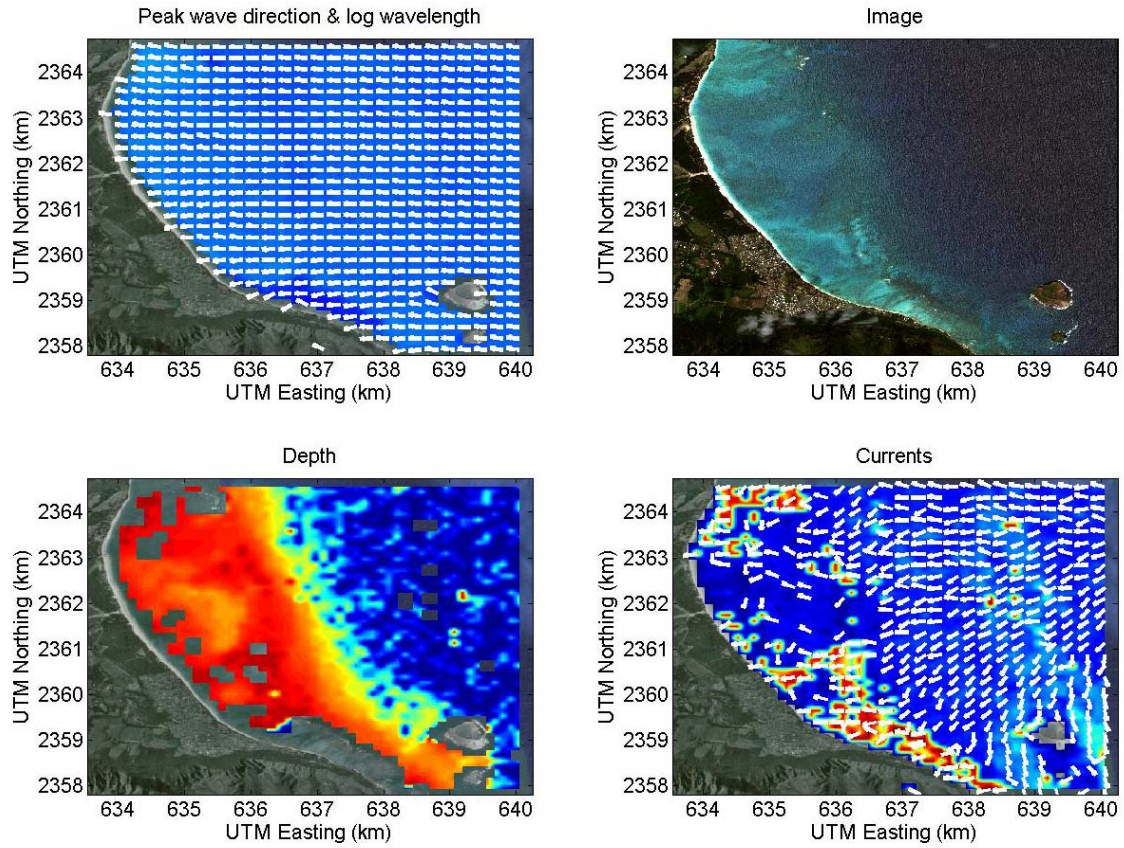
Figure 25.   2MSI WKB output showing wave direction (top left), a true color image (top right), extracted bathymetry (bottom left), and extracted ocean currents (bottom right)
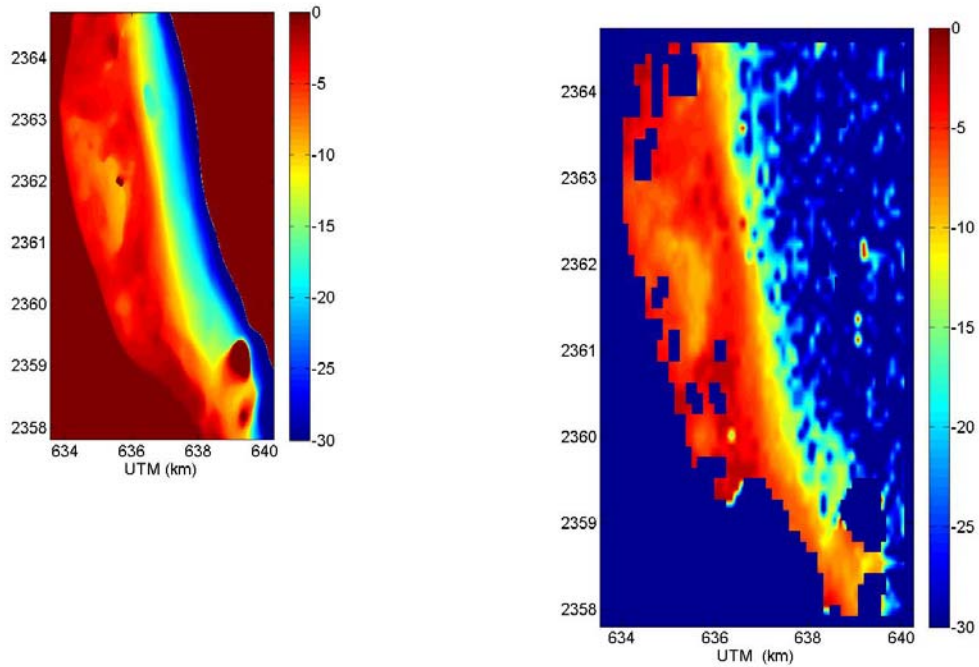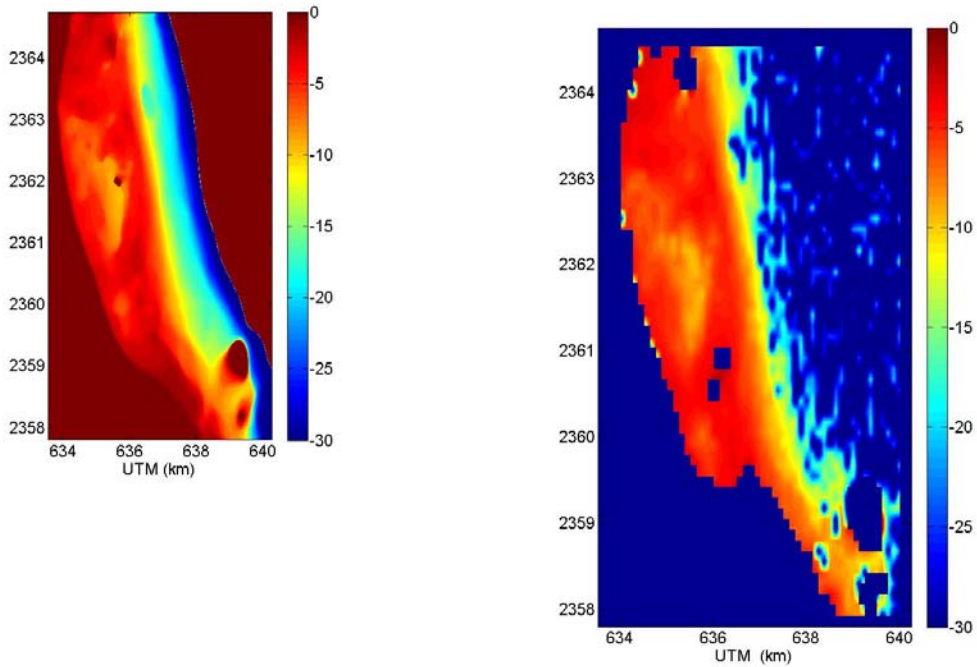
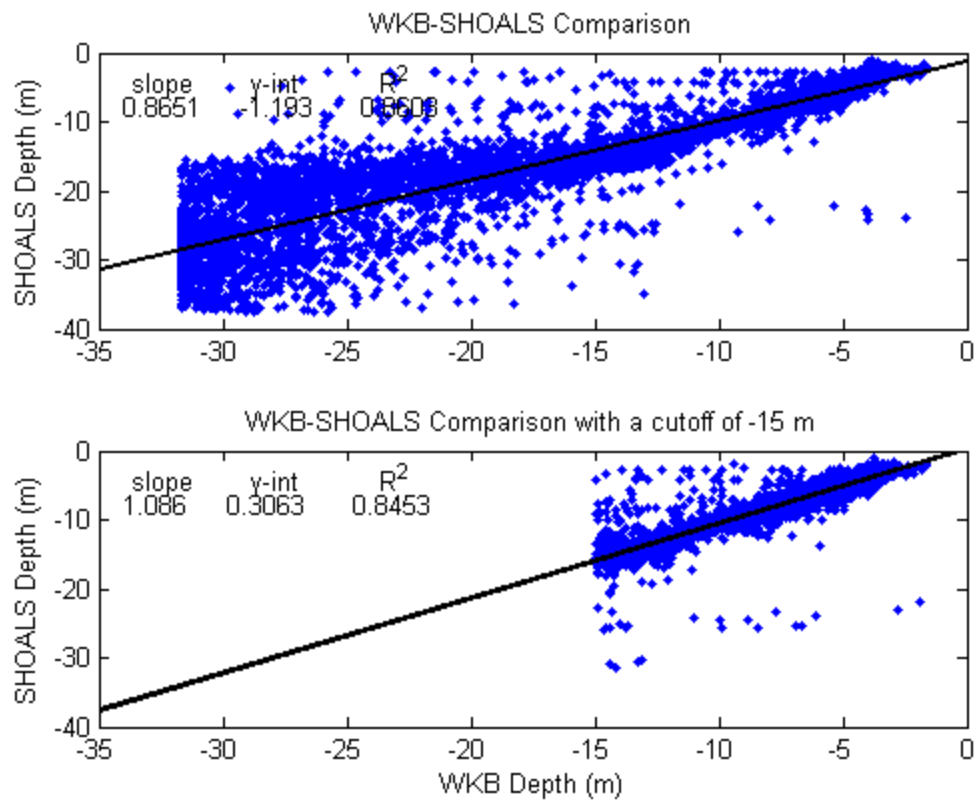Figure 26.   Comparison maps of SHOALS (left) and 2MSI WKB (right)
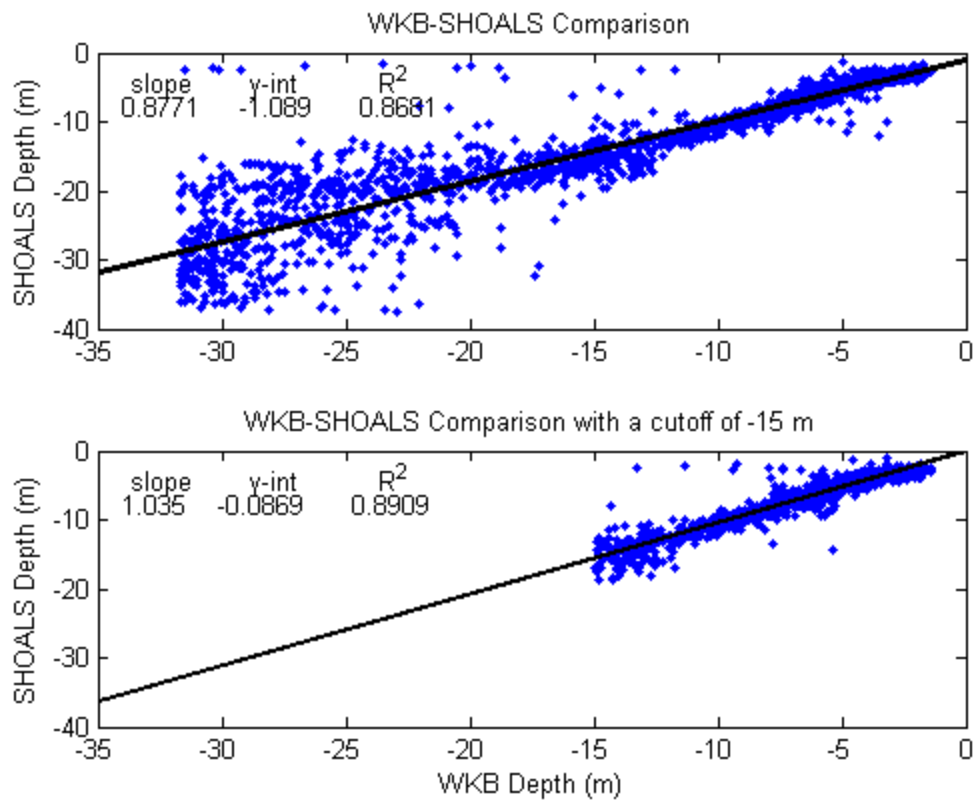
Figure 27.   2MSI scatter plot showing thinned data for all depths (top) and for just depths less than 15 m (bottom)
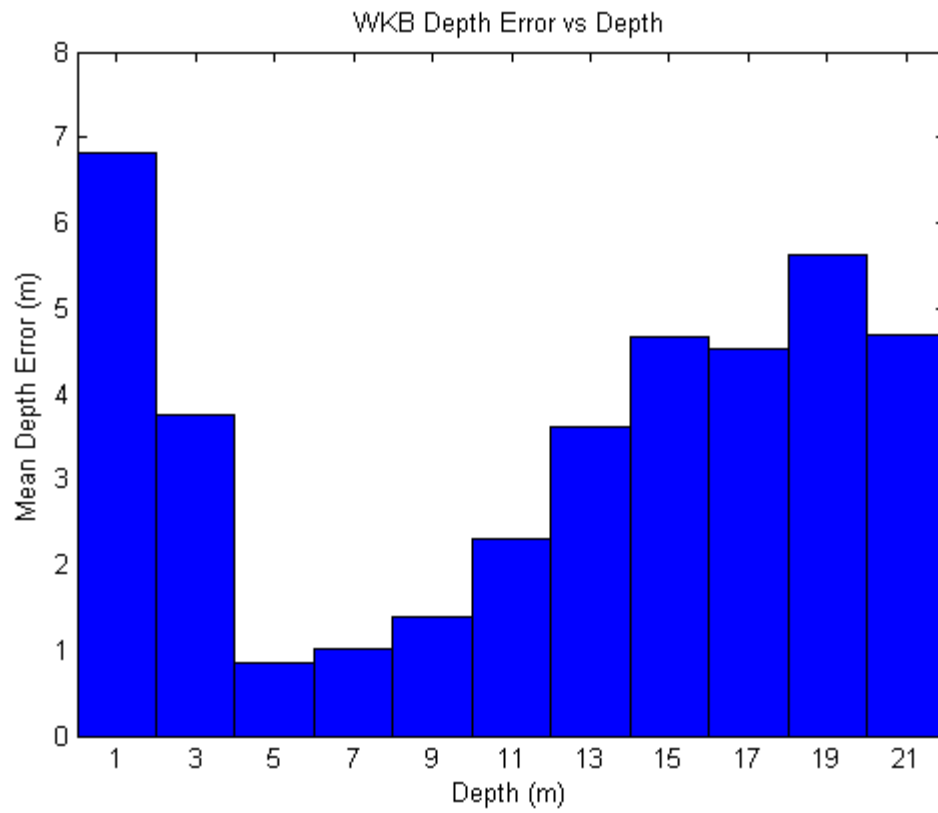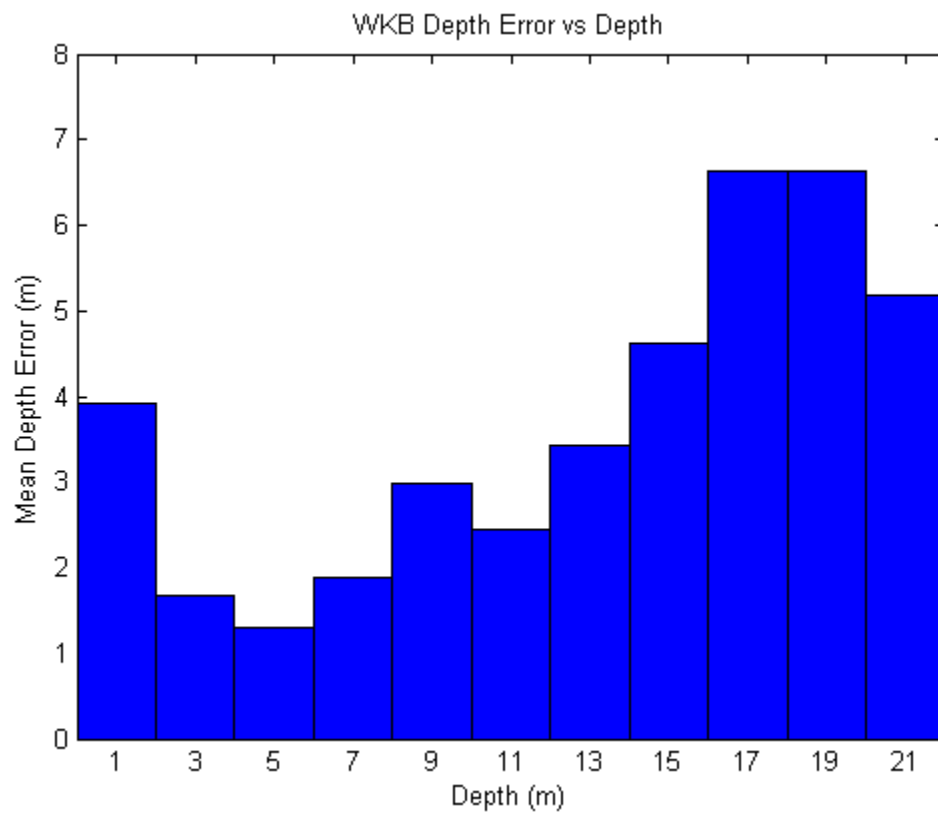
Figure 28.   2MSI bar graph showing the mean depth error for several depth bins
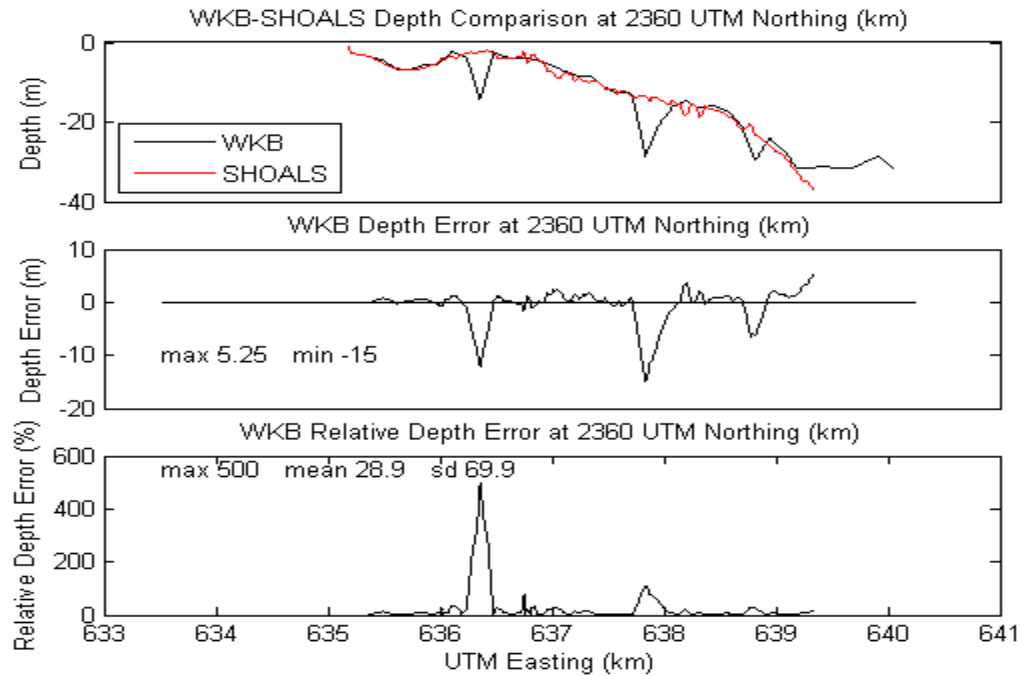
Figure 29.   Transect at specified location showing 2MSI WKB (see below for more explanation of the panels)
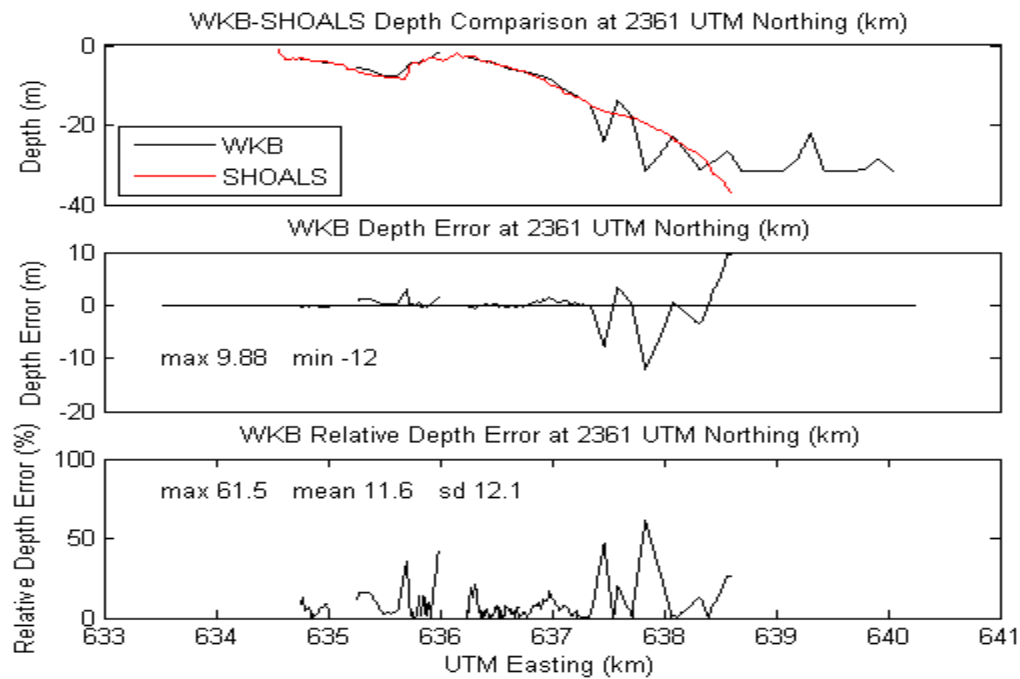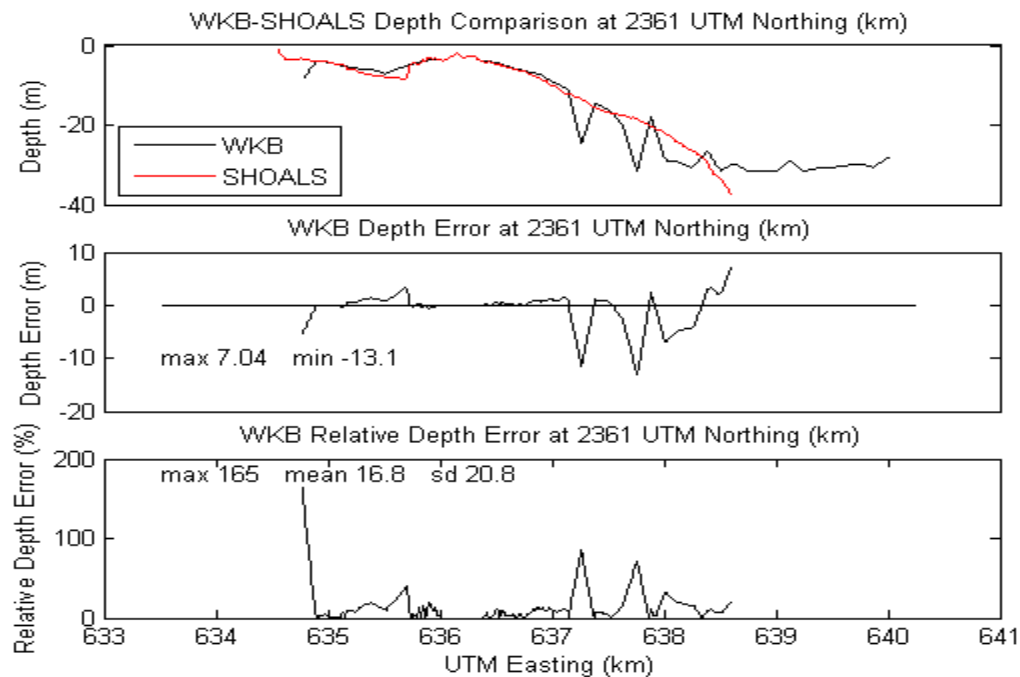

Figure 30.   Transect at specified location showing 2MSI WKB depth plotted with SHOALS depth (top); the difference between them, or depth error (mid); and depth error as a percentage of depth, or relative depth error (bot)
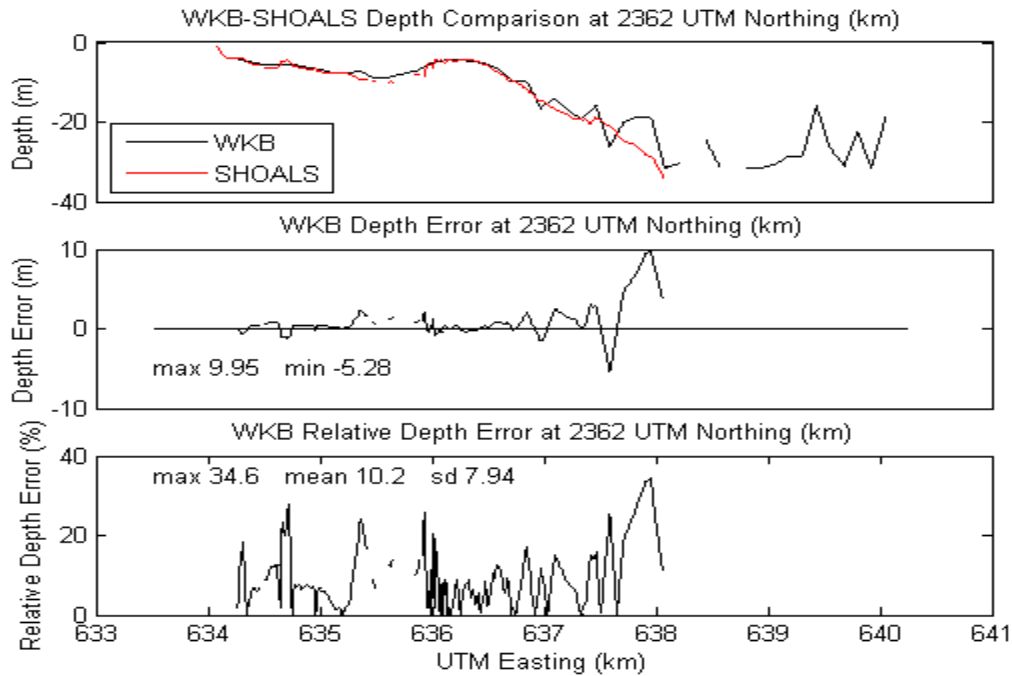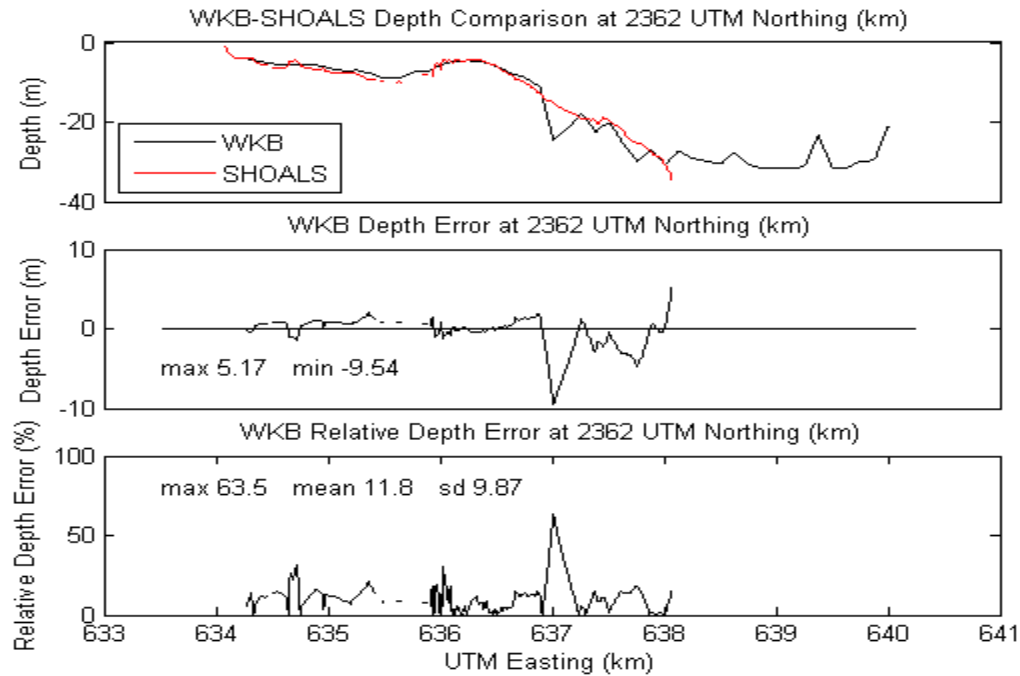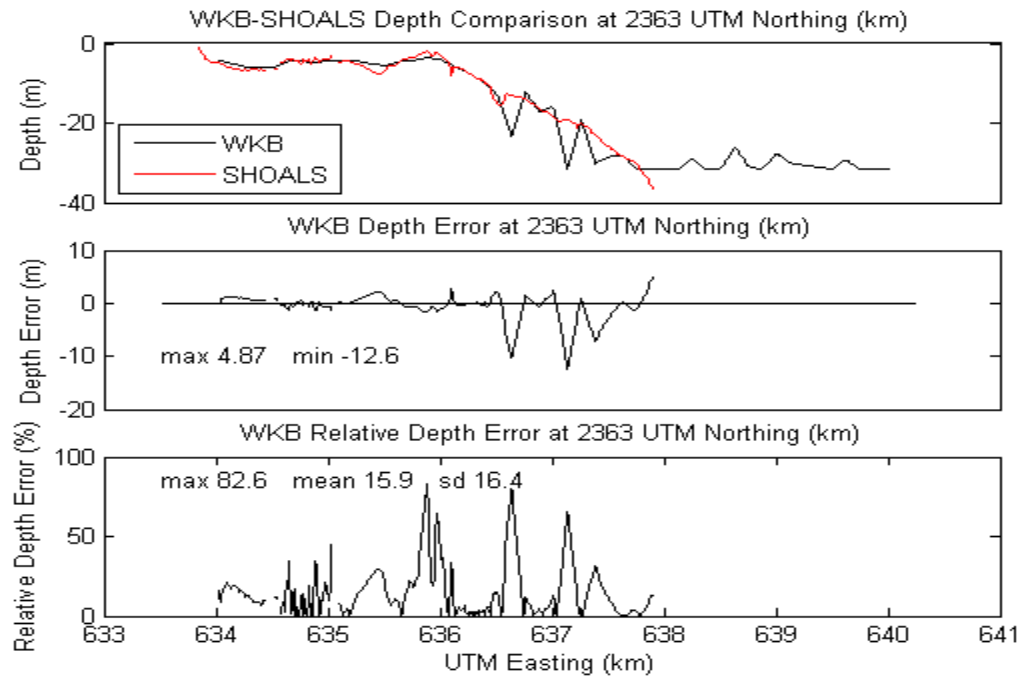
Figure 31.   Transect at specified location showing 2MSI WKB (see below for more explanation of the panels)
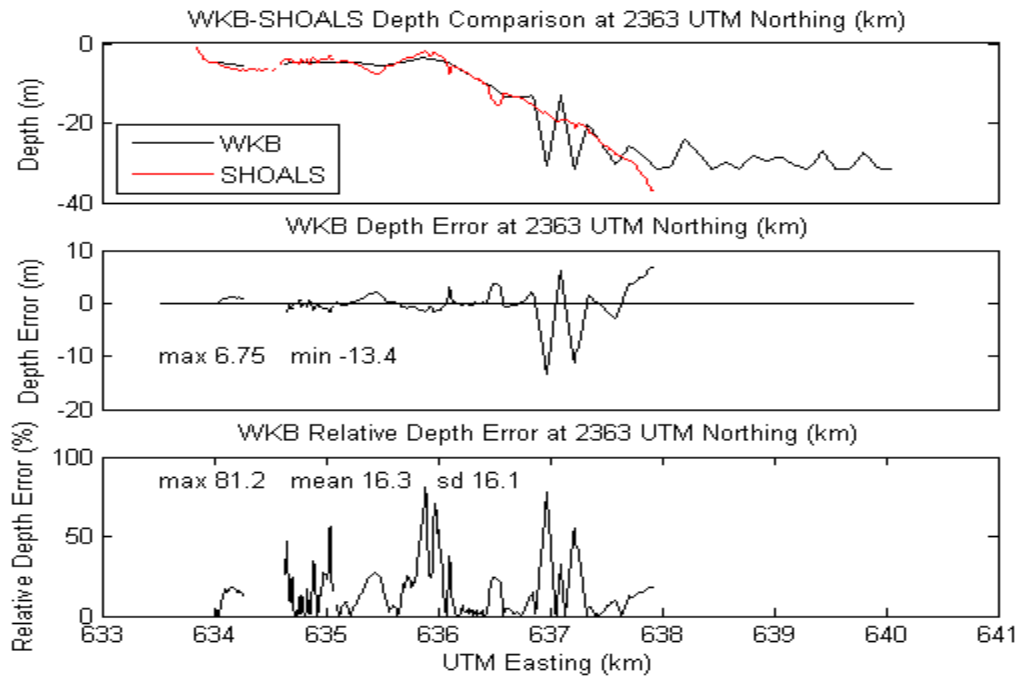
Figure 32.   Transect at specified location showing 2MSI WKB depth plotted with SHOALS depth (top); the difference between them, or depth error (mid); and depth error as a percentage of depth, or relative depth error (bot)
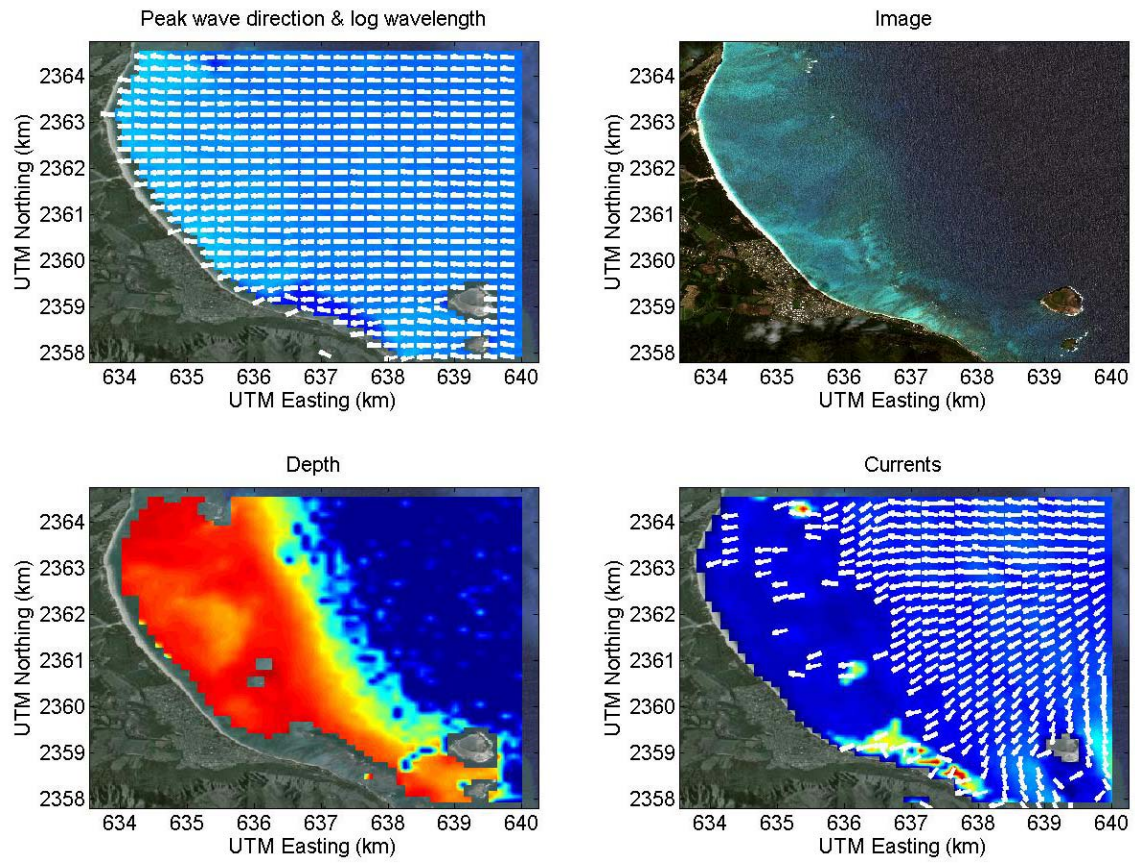
CASE: 3MSI
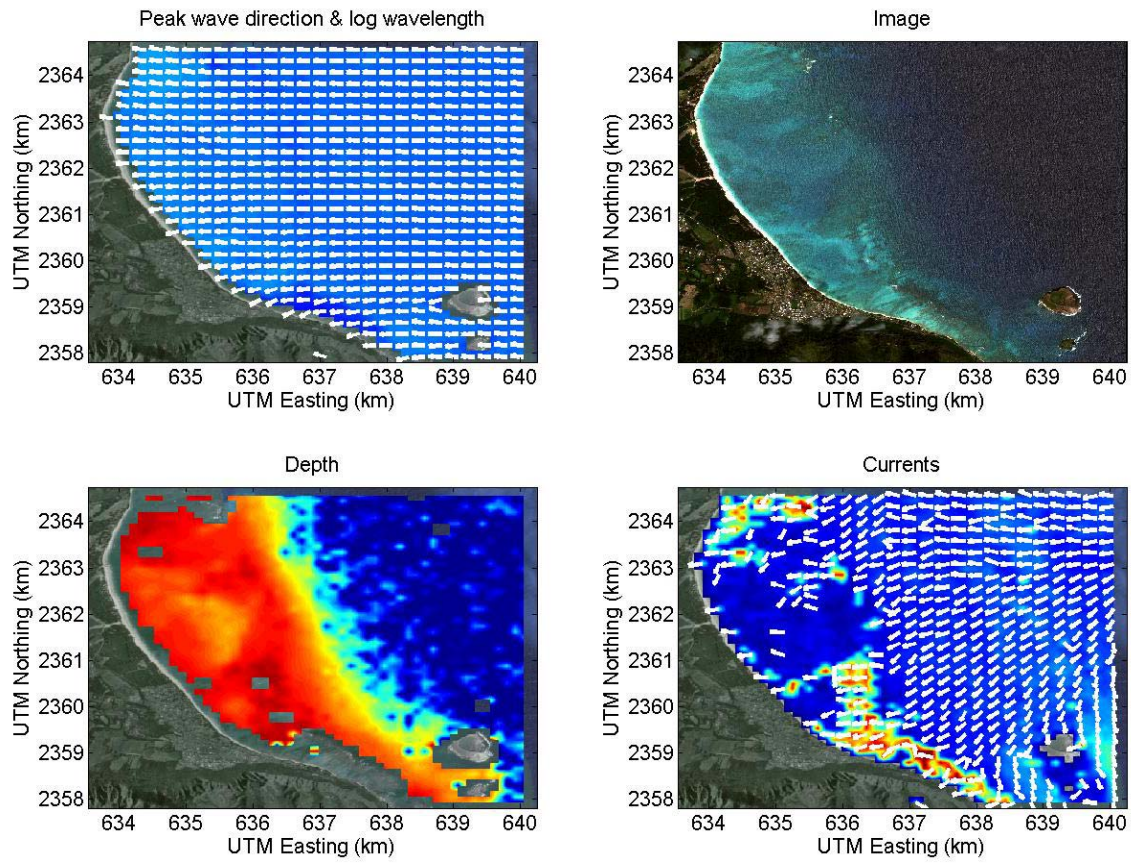
Figure 33.   3MSI WKB output showing wave direction (top left), a true color image (top right), extracted bathymetry (bottom left), and extracted ocean currents (bottom right)
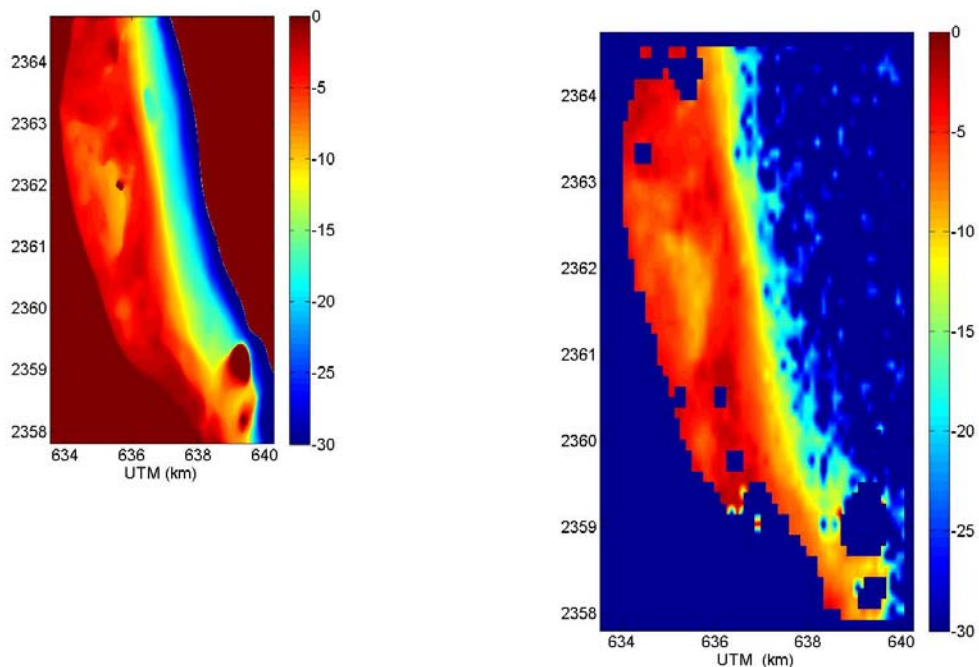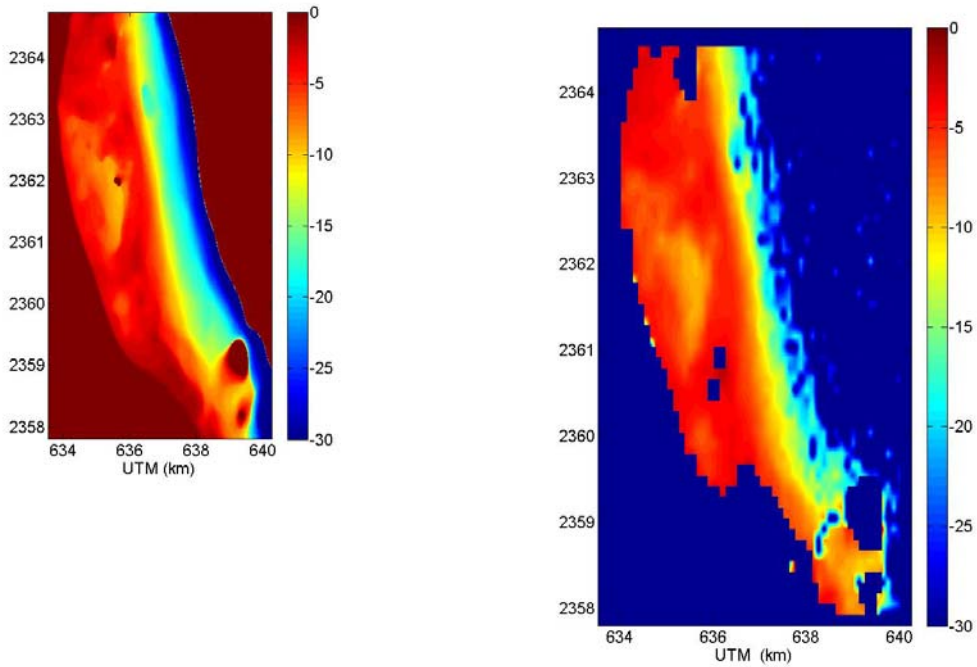
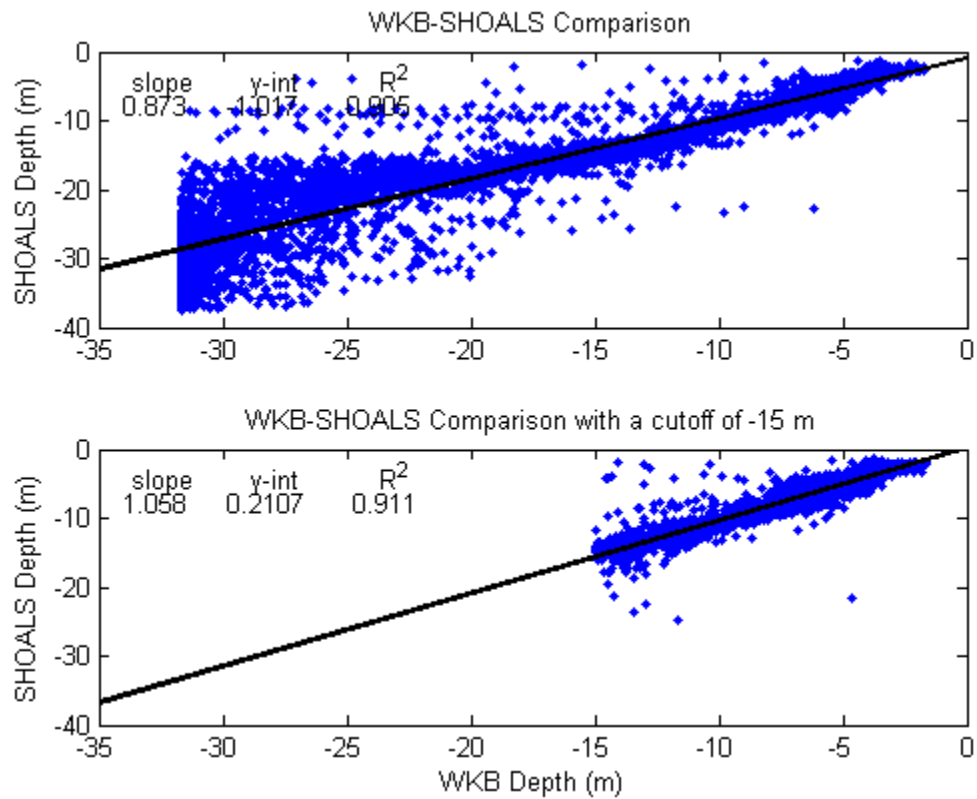Figure 34.   Comparison maps of SHOALS (left) and 3MSI WKB (right)
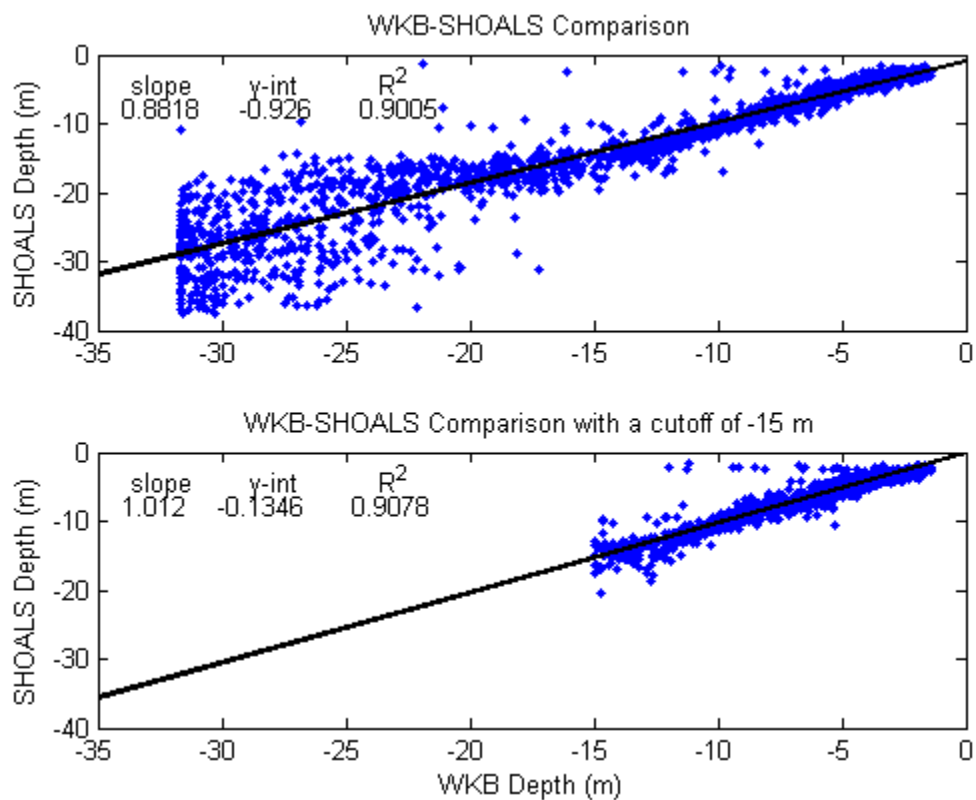
Figure 35.   3MSI scatter plot showing thinned data for all depths (top) and for
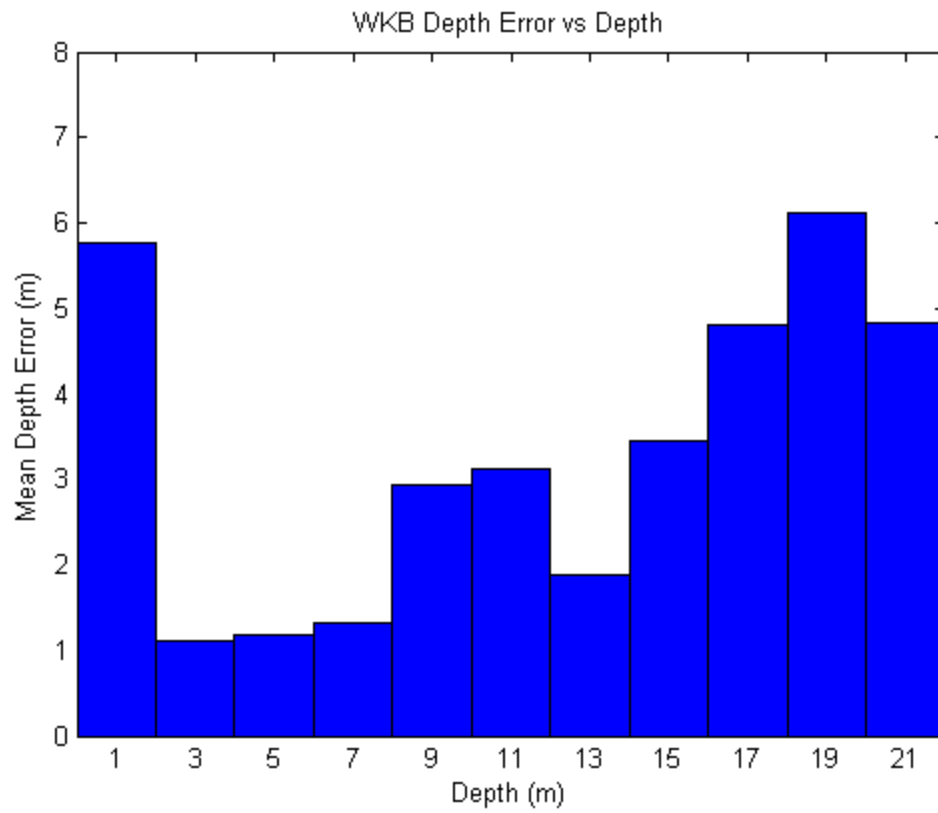just depths less than 15 m (bottom)
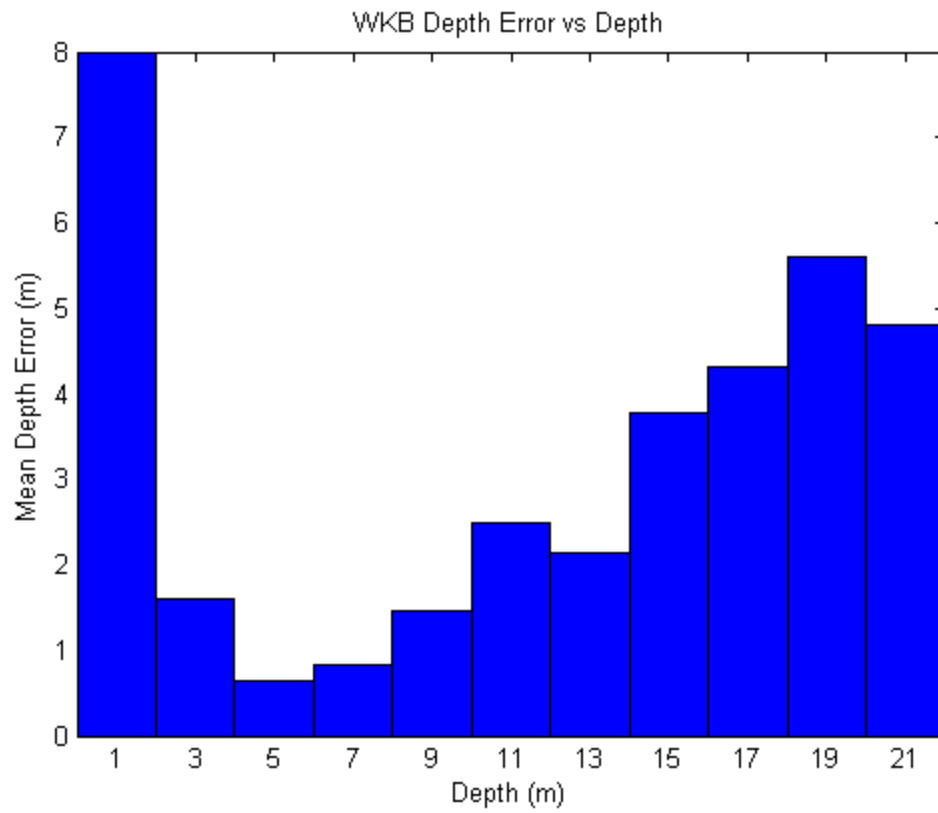
Figure 36.   3MSI bar graph showing the mean depth error for several depth
bins
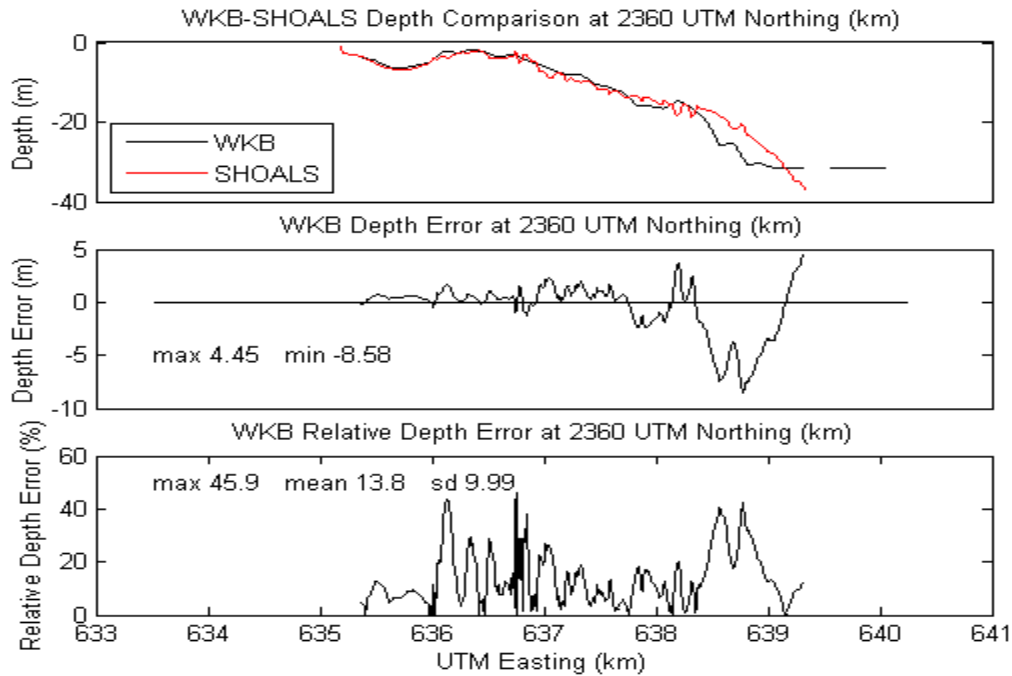
Figure 37.   Transect at specified location showing 3MSI WKB (see below for more explanation of the panels)
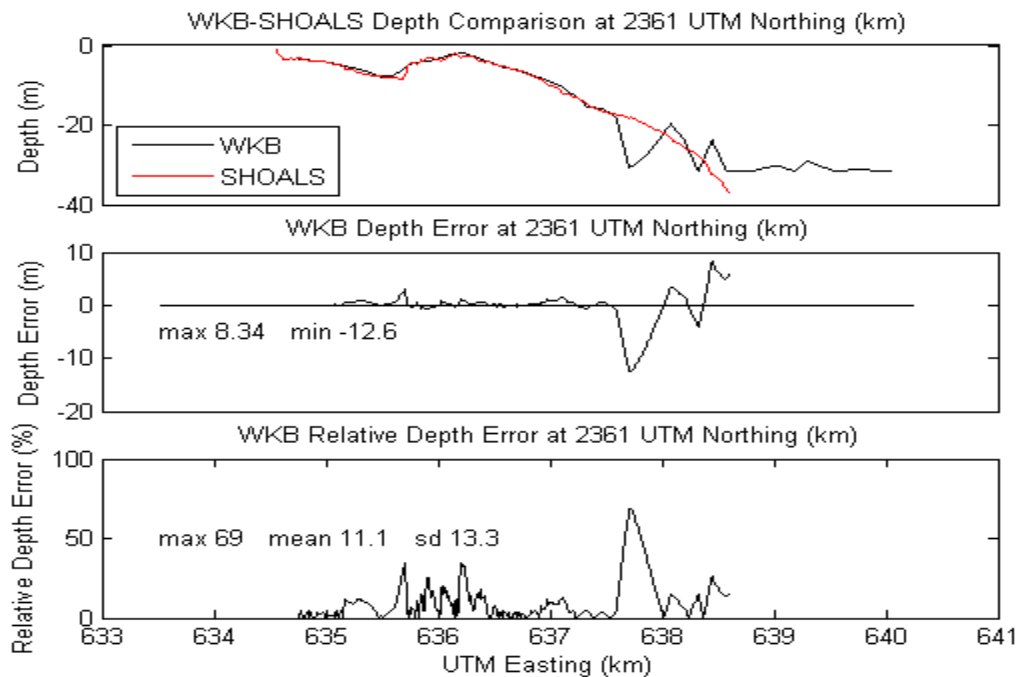
Figure 38.   Transect at specified location showing 3MSI WKB depth plotted with SHOALS depth (top); the difference between them, or depth error (mid); and depth error as a percentage of depth, or relative depth error (bot)
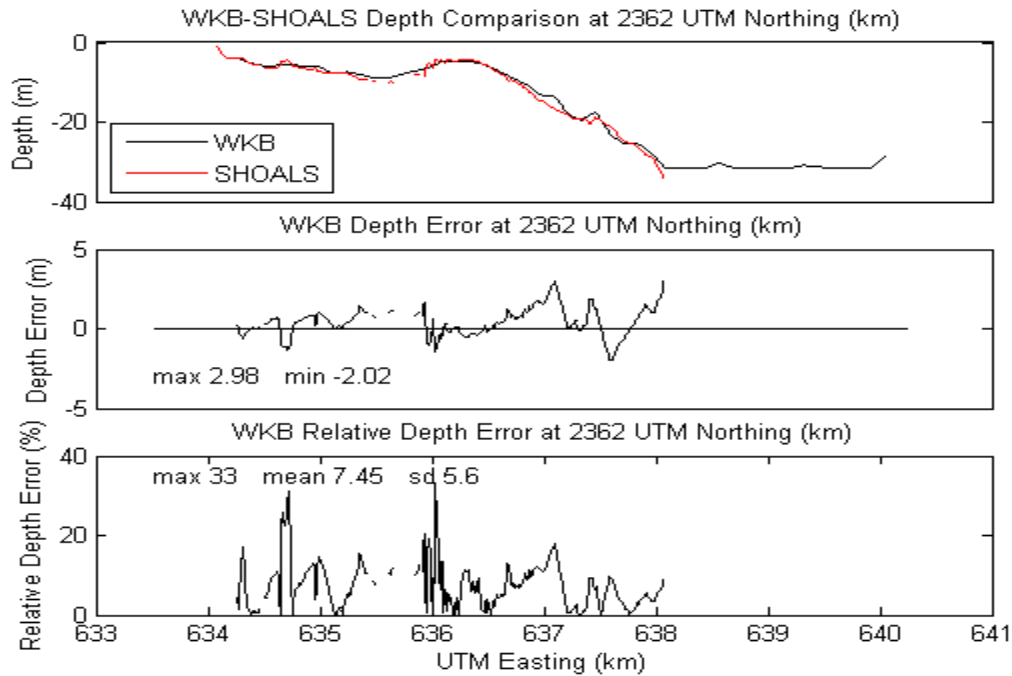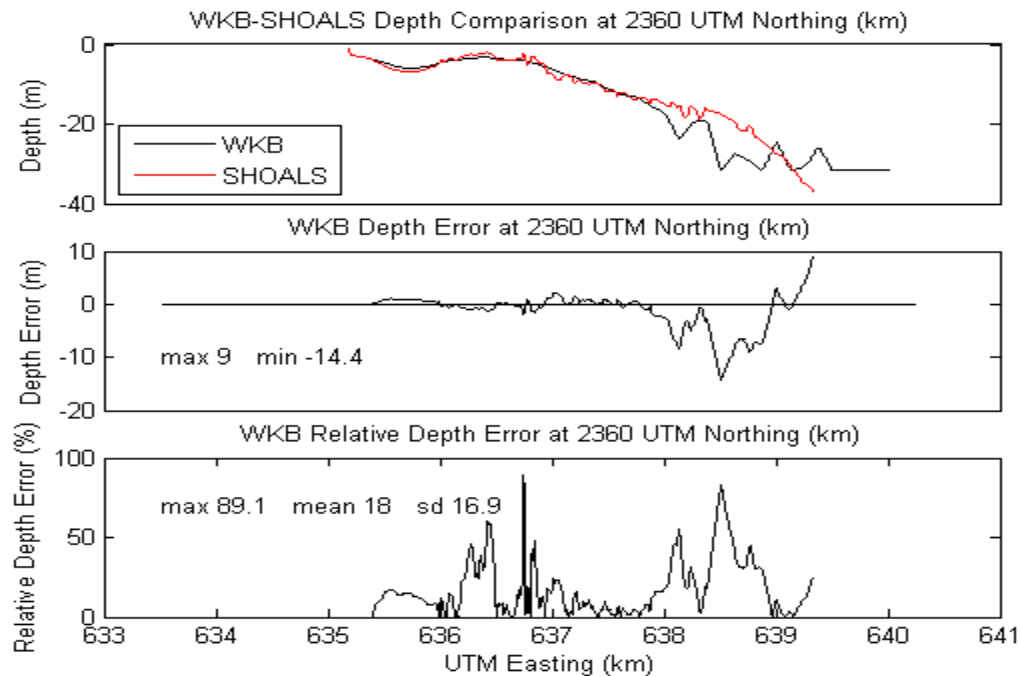
Figure 39.   Transect at specified location showing 3MSI WKB (see below for more explanation of the panels)
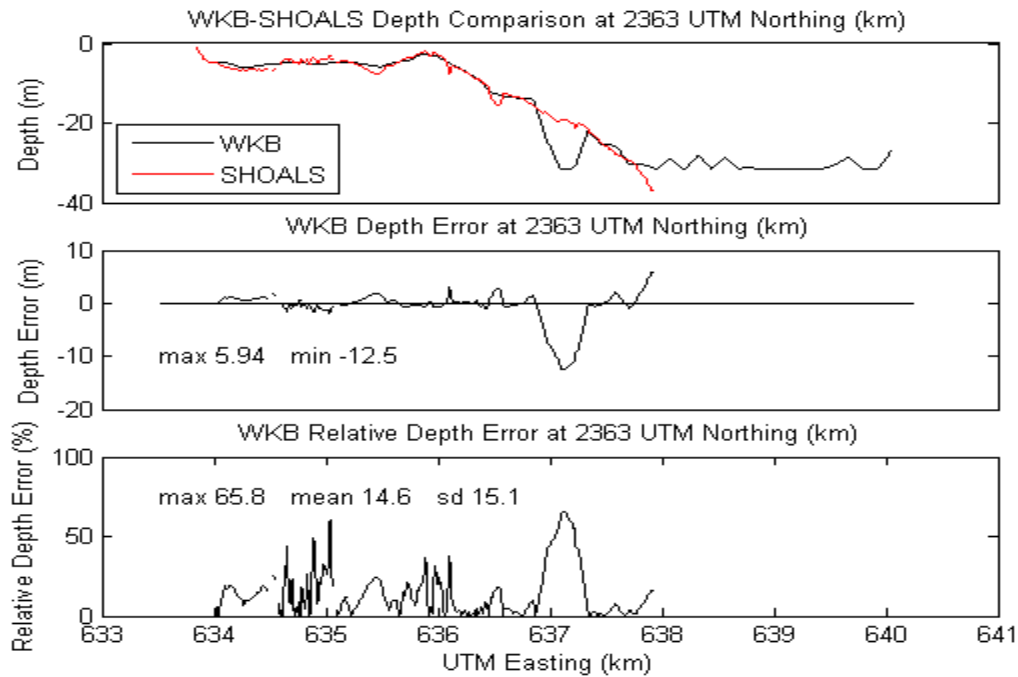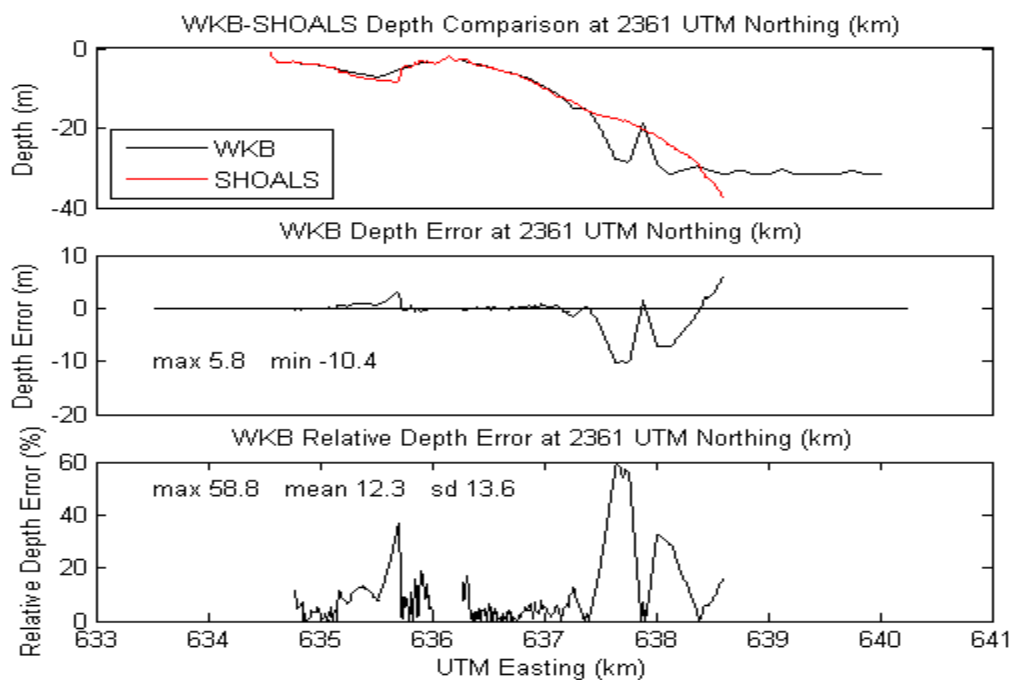

Figure 40.   Transect at specified location showing 3MSI WKB depth plotted with SHOALS depth (top); the difference between them, or depth error (mid); and depth error as a percentage of depth, or relative depth error (bot)
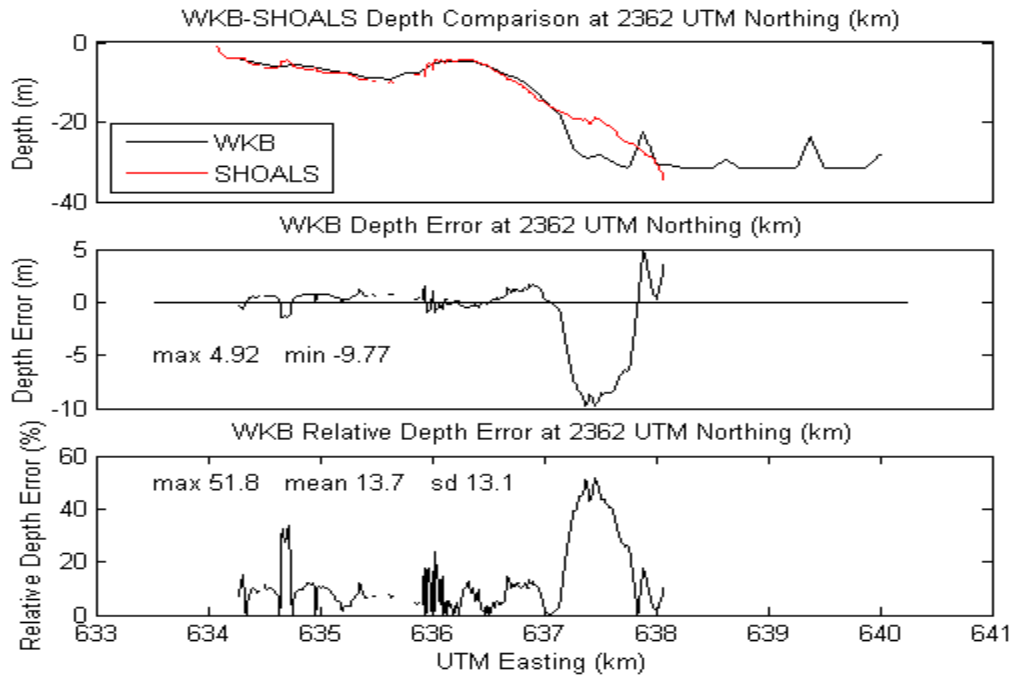
CASE: 2PAN

Figure 41.   2Pan WKB output showing wave direction (top left), a true color image (top right), extracted bathymetry (bottom left), and extracted ocean currents (bottom right)

Figure 42. Comparison maps of SHOALS (left) and 2Pan WKB (right)

Figure 43. 2Pan scatter plot showing thinned data for all depths (top) and for just depths less than 15 m (bottom)

Figure 44.   2Pan bar graph showing the mean depth error for several depth bins
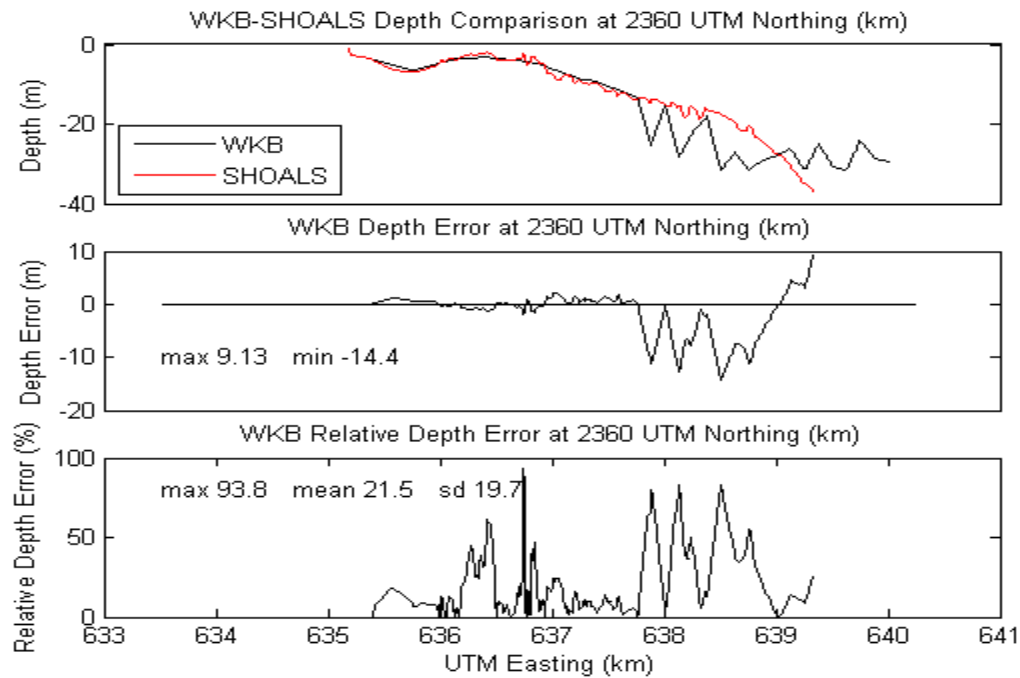
Figure 45. Transect at specified location showing 2Pan WKB (see below for more explanation of the panels)
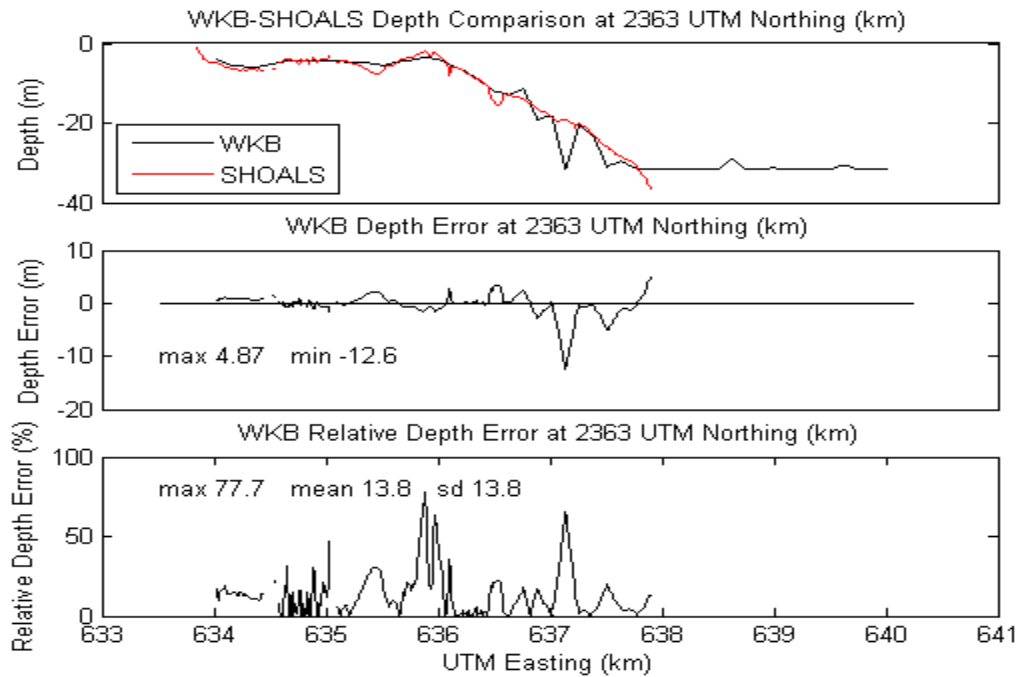

Figure 46. Transect at specified location showing 2Pan WKB depth plotted with SHOALS depth (top); the difference between them, or depth error (mid); and depth error as a percentage of depth, or relative depth error (bot)
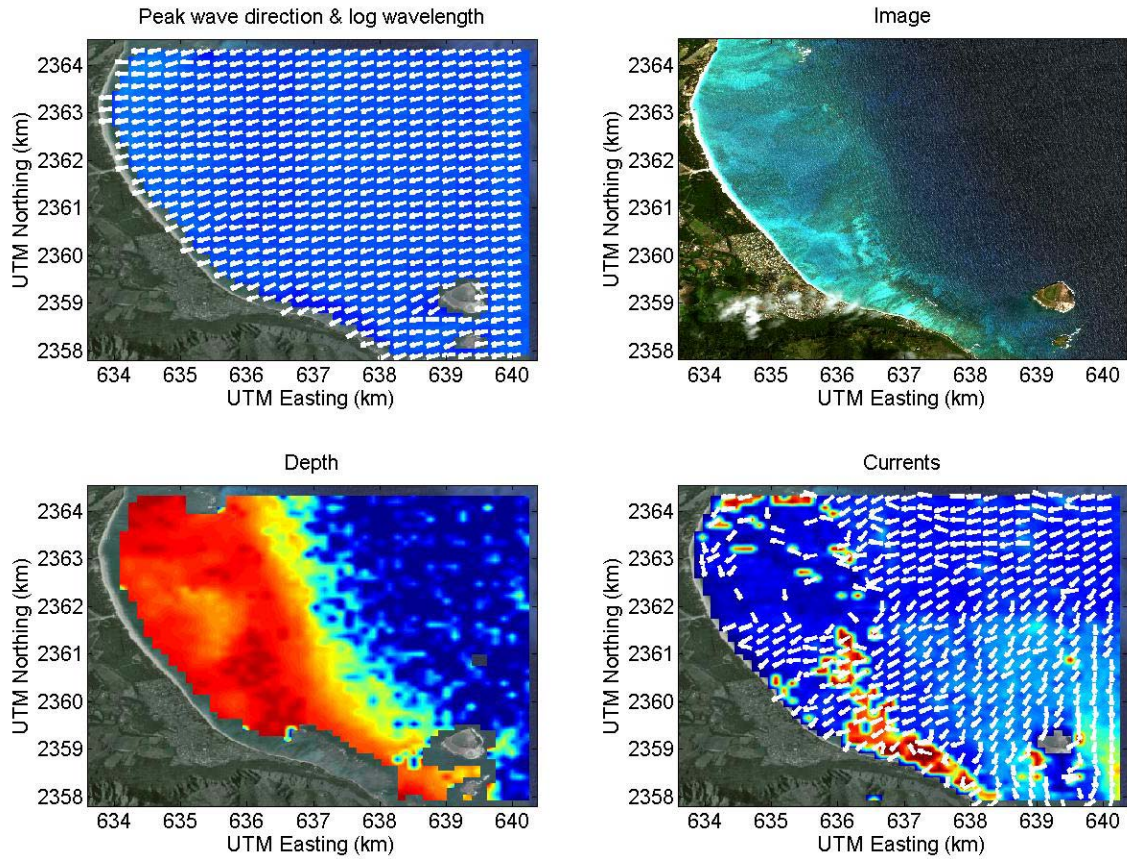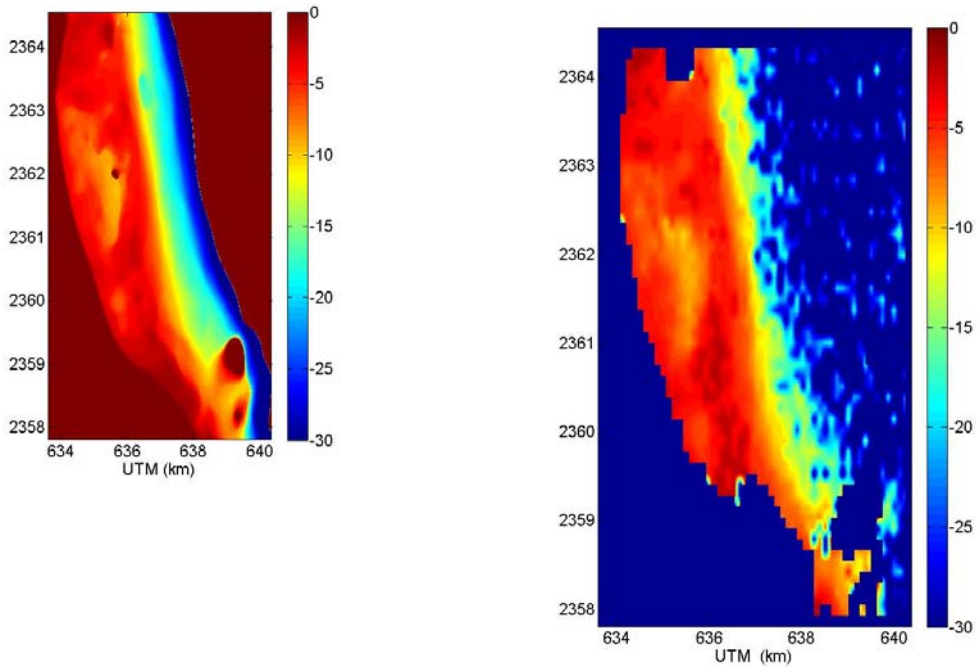
66

Figure 47.   Transect at specified location showing 2Pan WKB (see below for more explanation of the panels)

Figure 48.   Transect at specified location showing 2Pan WKB depth plotted with SHOALS depth (top); the difference between them, or depth error (mid); and depth error as a percentage of depth, or relative depth error (bot)

CASE: 3PAN

Figure 49.   3Pan WKB output showing wave direction (top left), a true color image (top right), extracted bathymetry (bottom left), and extracted ocean currents (bottom right)

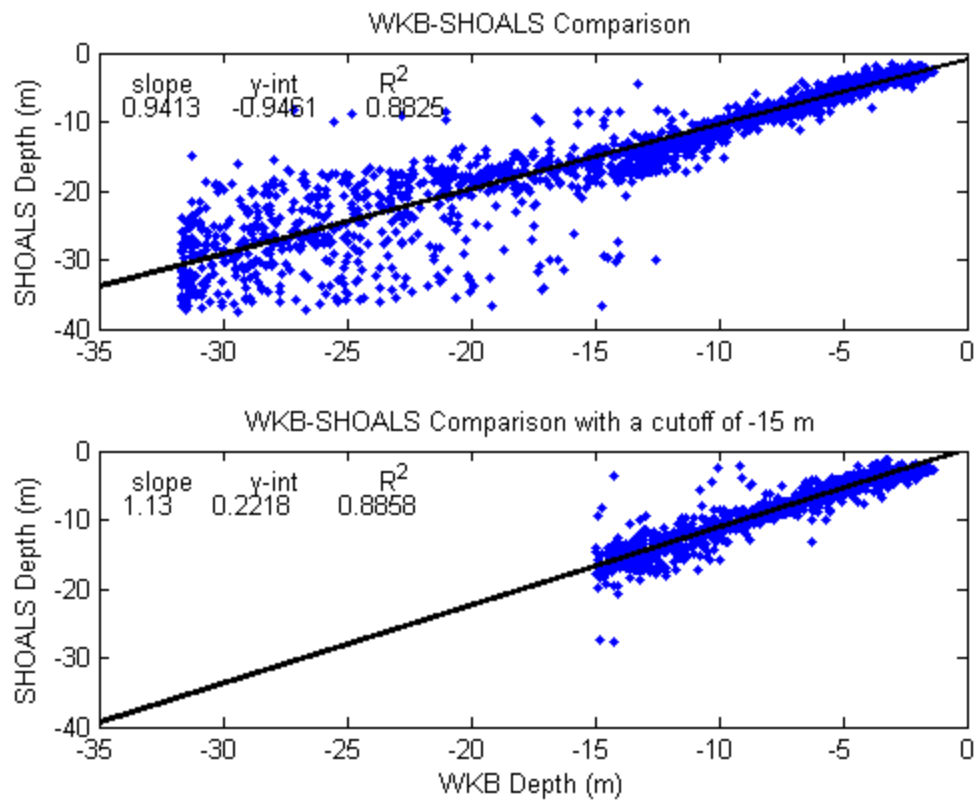Figure 50.   Comparison maps of SHOALS (left) and 3Pan WKB (right)

Figure 51.   3Pan scatter plot showing thinned data for all depths (top) and for just depths less than 15 m (bottom)
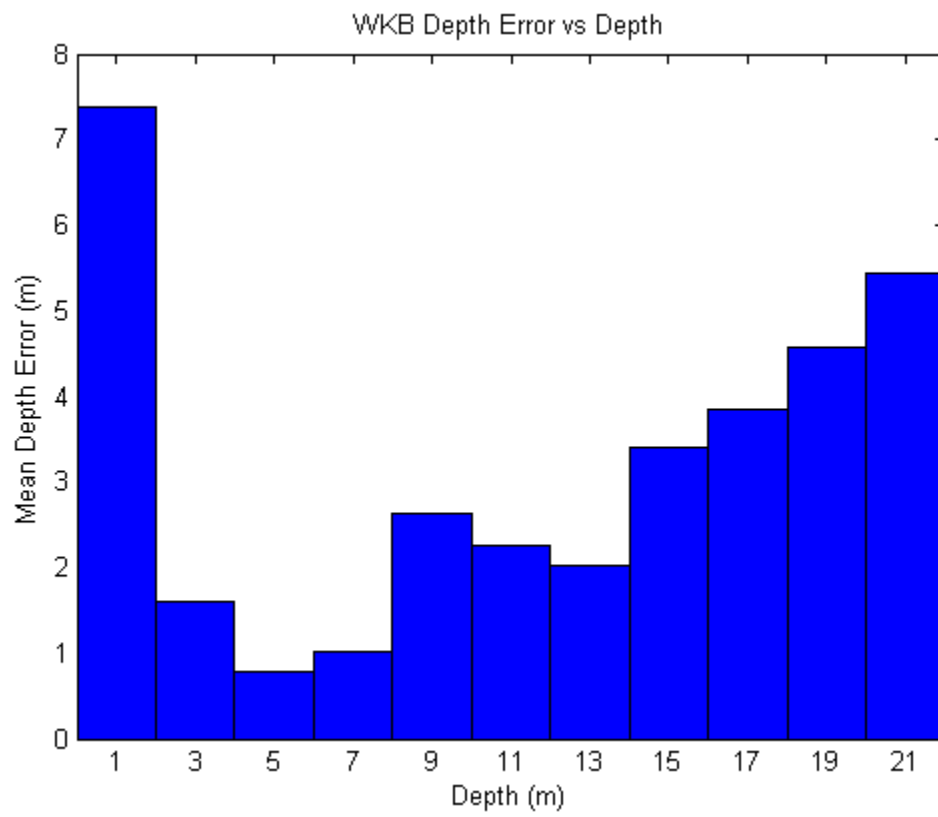
Figure 52.   3Pan bar graph showing the mean depth error for several depth bins
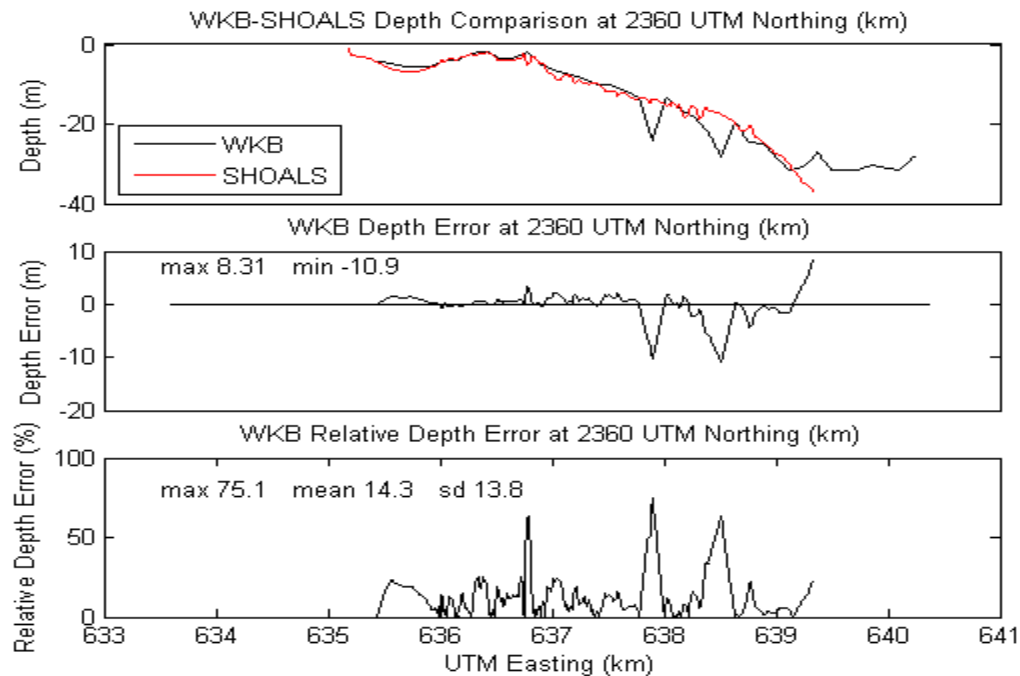
Figure 53. Transect at specified location showing 3Pan WKB (see below for more explanation of the panels)
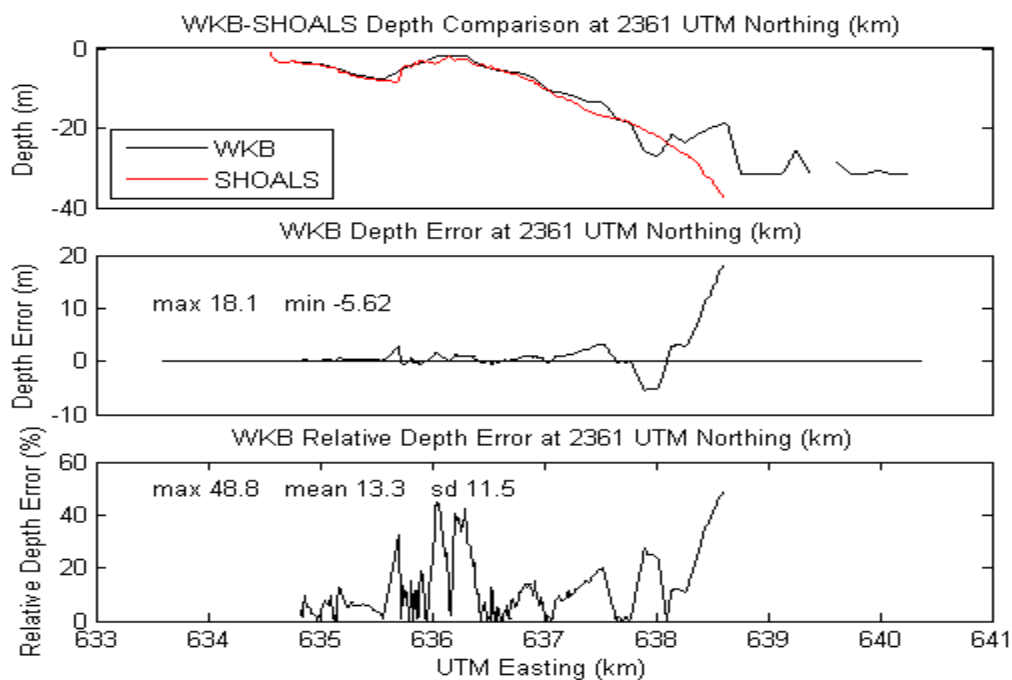

Figure 54. Transect at specified location showing 3Pan WKB depth plotted with SHOALS depth (top); the difference between them, or depth error (mid); and depth error as a percentage of depth, or relative depth error (bot)
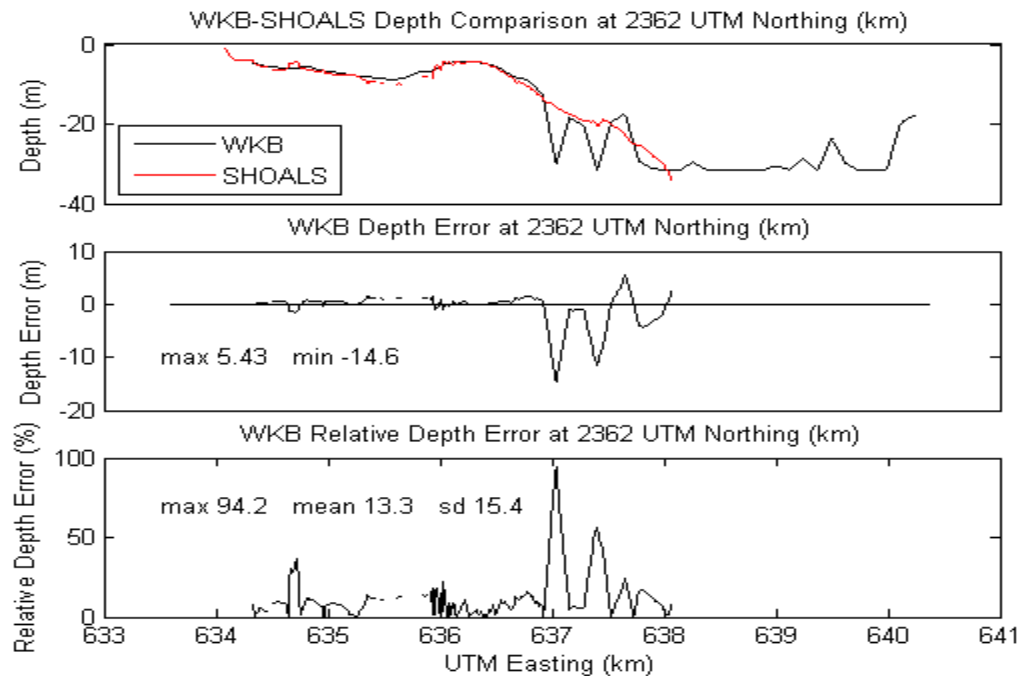
71

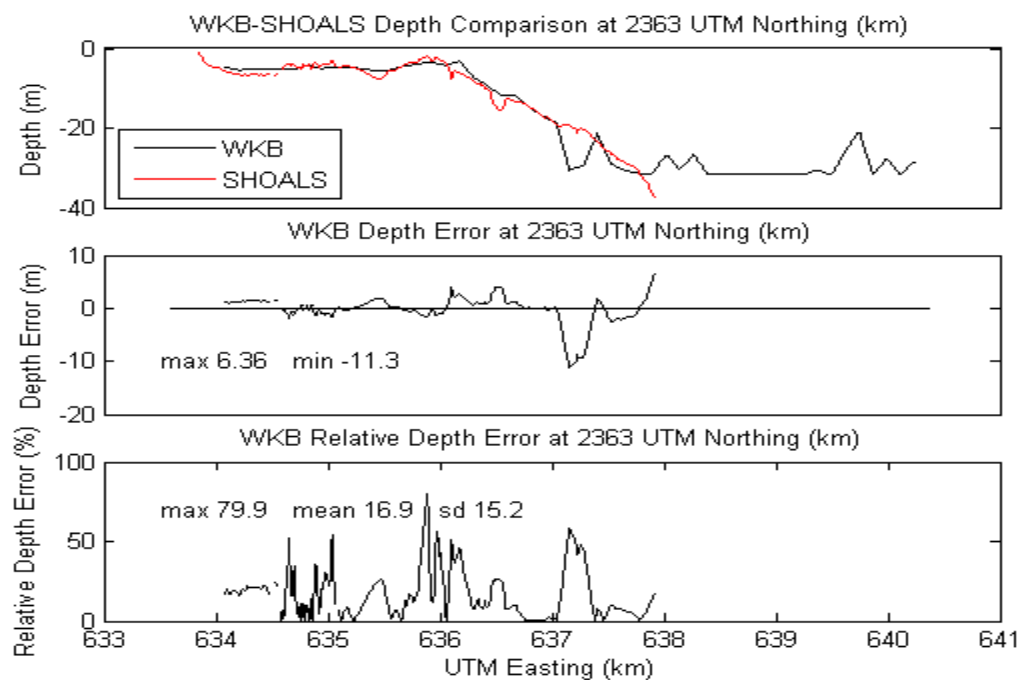Figure 55. Transect at specified location showing 3Pan WKB (see below for more explanation of the panels)

Figure 56. Transect at specified location showing 3Pan WKB depth plotted with SHOALS depth (top); the difference between them, or depth error (mid); and depth error as a percentage of depth, or relative depth error (bot)

72

APPENDIX B.   IMAGE SET 2
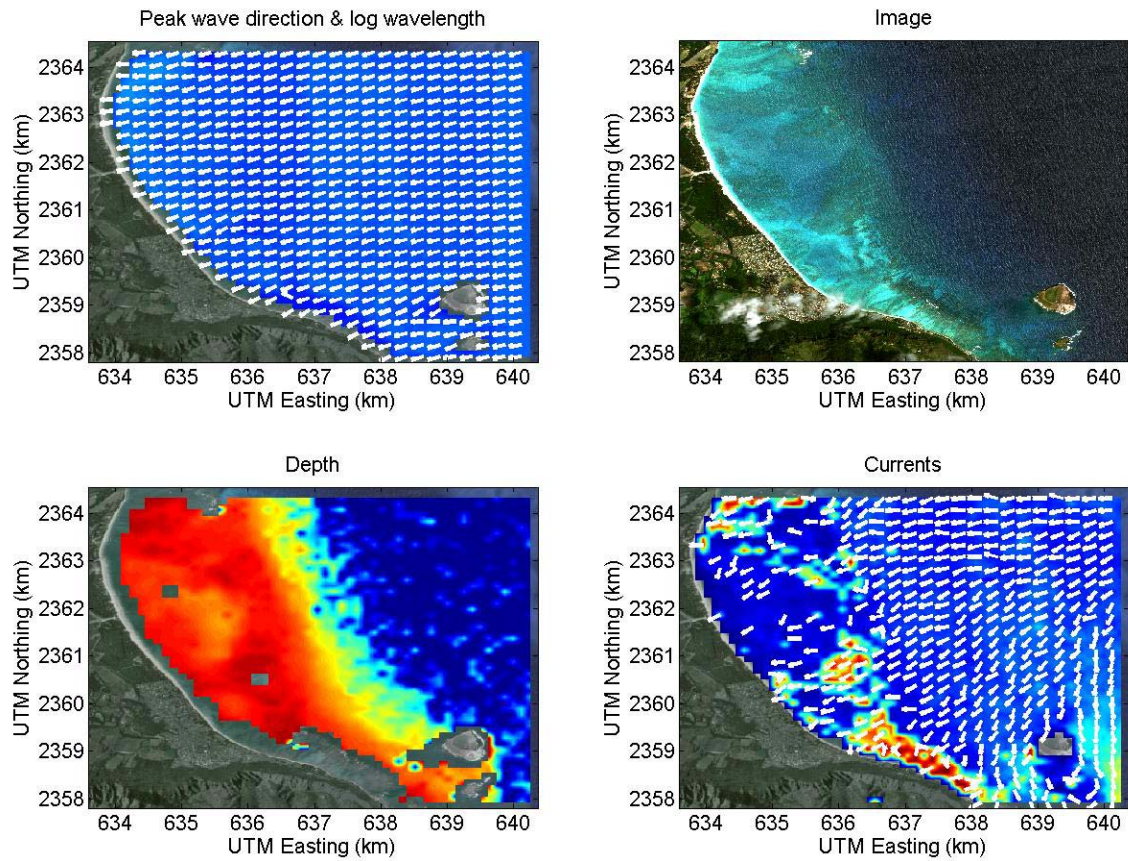
CASE: 2MSI

Figure 57.   2MSI WKB output showing wave direction (top left), a true color image (top right), extracted bathymetry (bottom left), and extracted ocean currents (bottom right)
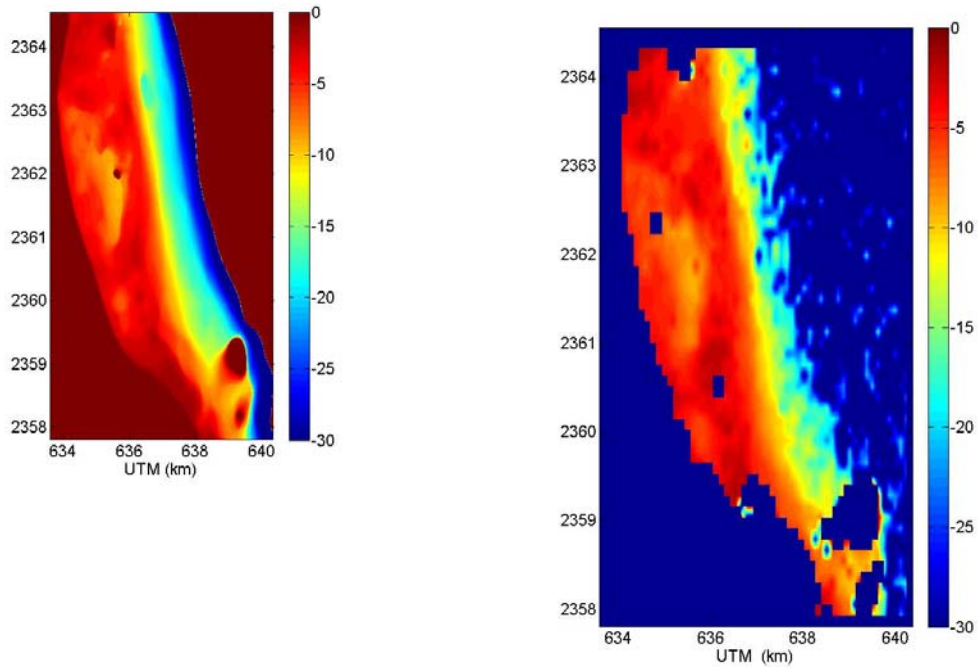
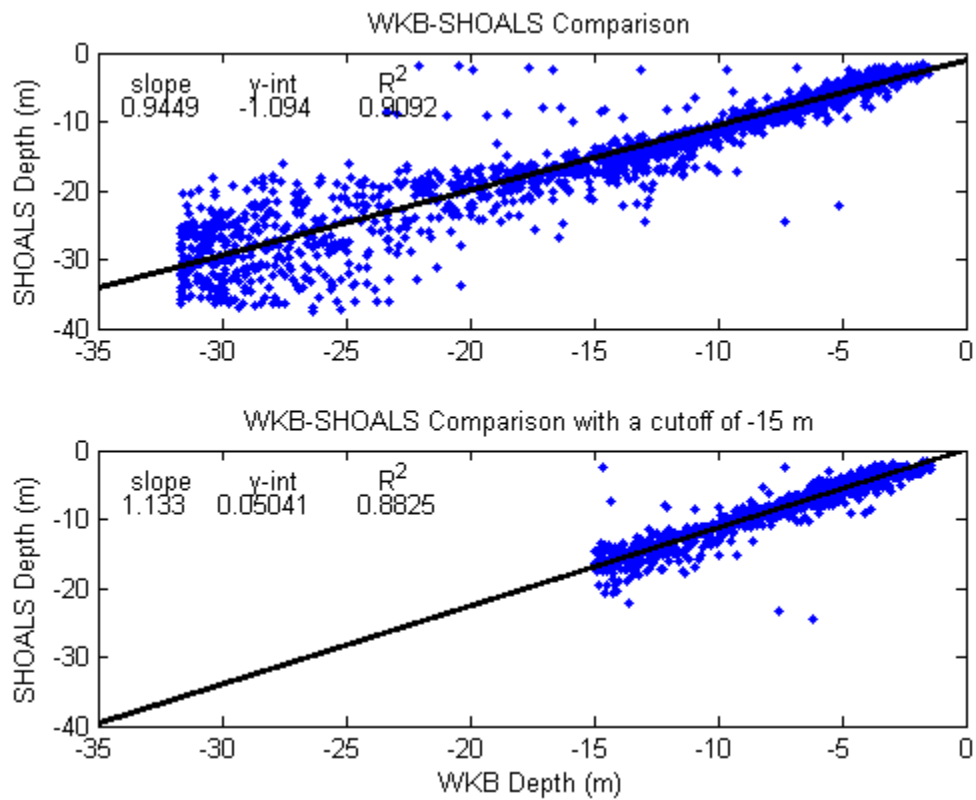Figure 58.   Comparison maps of SHOALS (left) and 2MSI WKB (right)

Figure 59.   2MSI scatter plot showing thinned data for all depths (top) and for
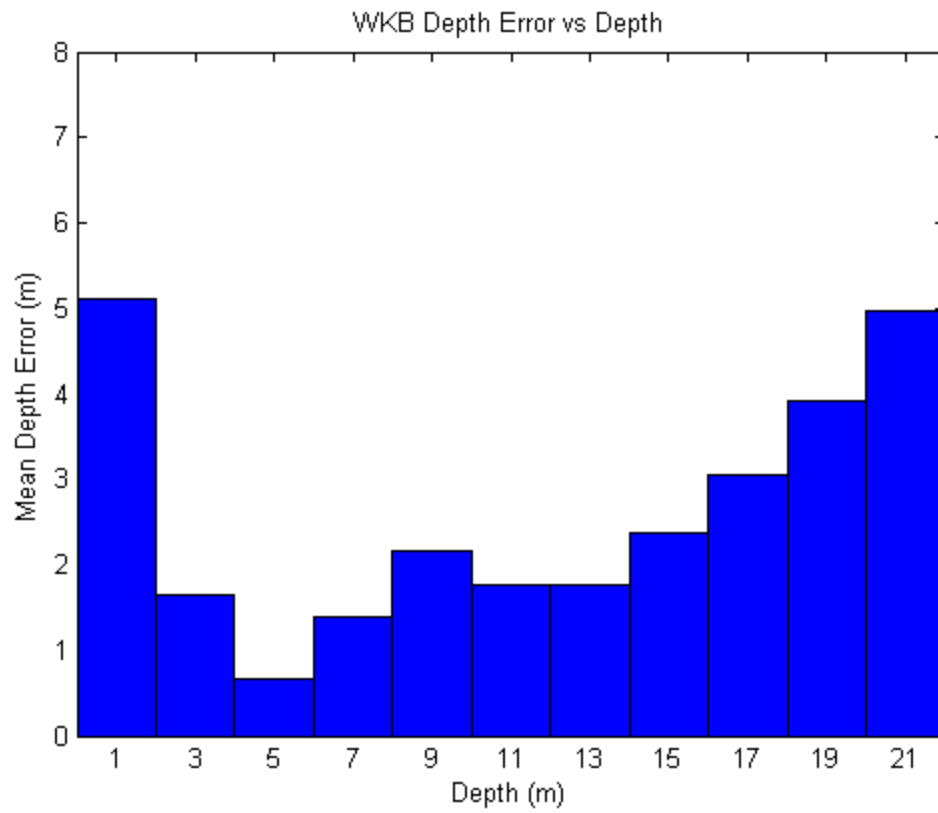just depths less than 15 m (bottom)

Figure 60.   2MSI bar graph showing the mean depth error for several depth bins

Figure 61. Transect at specified location showing 2MSI WKB (see below for more explanation of the panels)

Figure 62. Transect at specified location showing 2MSI WKB depth plotted with SHOALS depth (top); the difference between them, or depth error (mid); and depth error as a percentage of depth, or relative depth error (bot)

Figure 63.   Transect at specified location showing 2MSI WKB (see below for
more explanation of the panels)

Figure 64.   Transect at specified location showing 2MSI WKB depth plotted
with SHOALS depth (top); the difference between them, or depth error
(mid); and depth error as a percentage of depth, or relative depth error (bot)

77

CASE: 3MSI

Figure 65.   3MSI WKB output showing wave direction (top left), a true color image (top right), extracted bathymetry (bottom left), and extracted ocean currents (bottom right)

Figure 66.   Comparison maps of SHOALS (left) and 3MSI WKB (right)

Figure 67.   3MSI scatter plot showing thinned data for all depths (top) and for just depths less than 15 m (bottom)

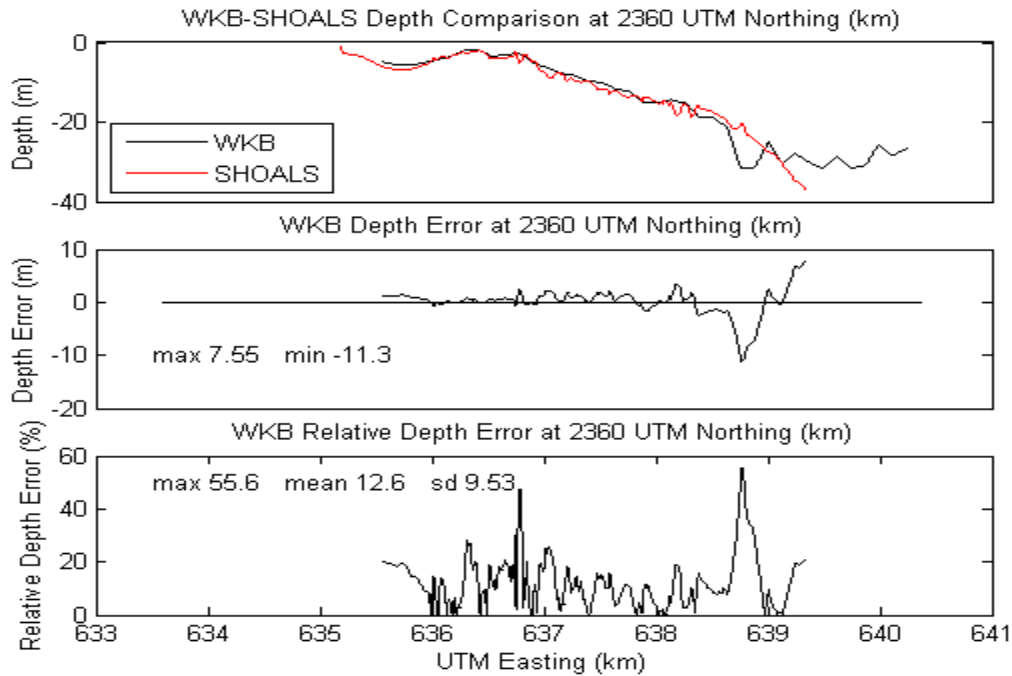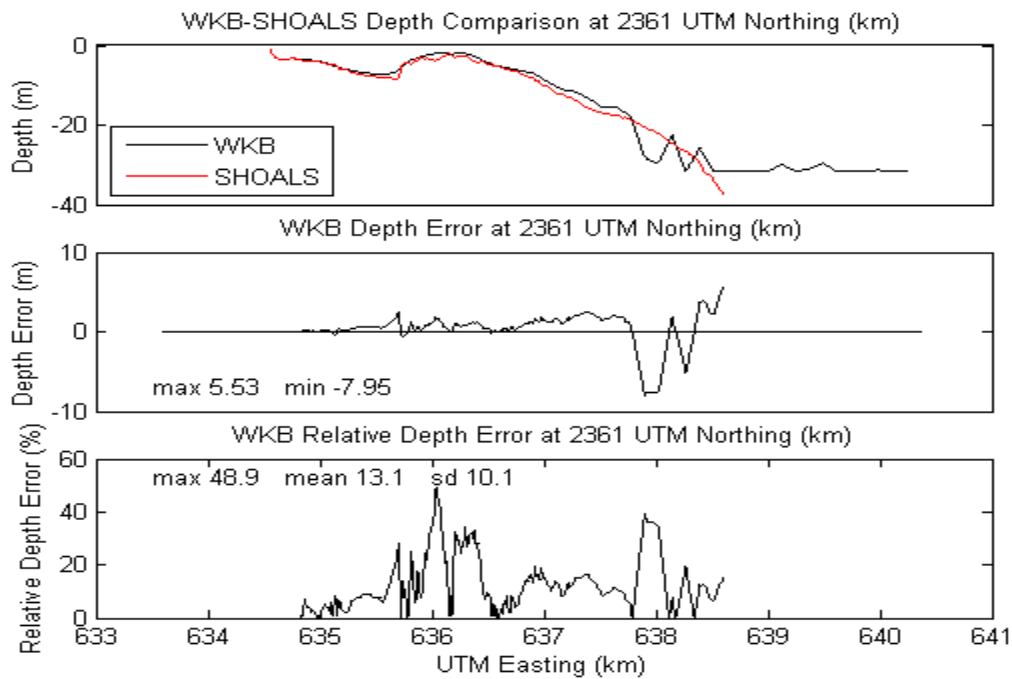Figure 68.   3MSI bar graph showing the mean depth error for several depth bins

Figure 69.   Transect at specified location showing 3MSI WKB (see below for more explanation of the panels)

Figure 70.   Transect at specified location showing 3MSI WKB depth plotted with SHOALS depth (top); the difference between them, or depth error (mid); and depth error as a percentage of depth, or relative depth error (bot)
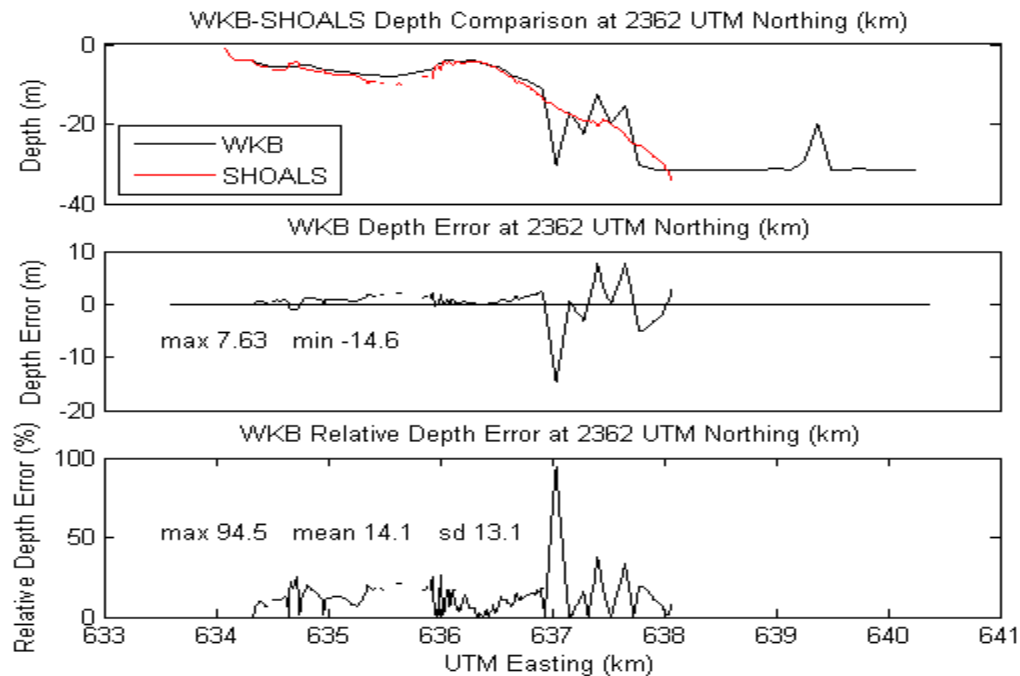
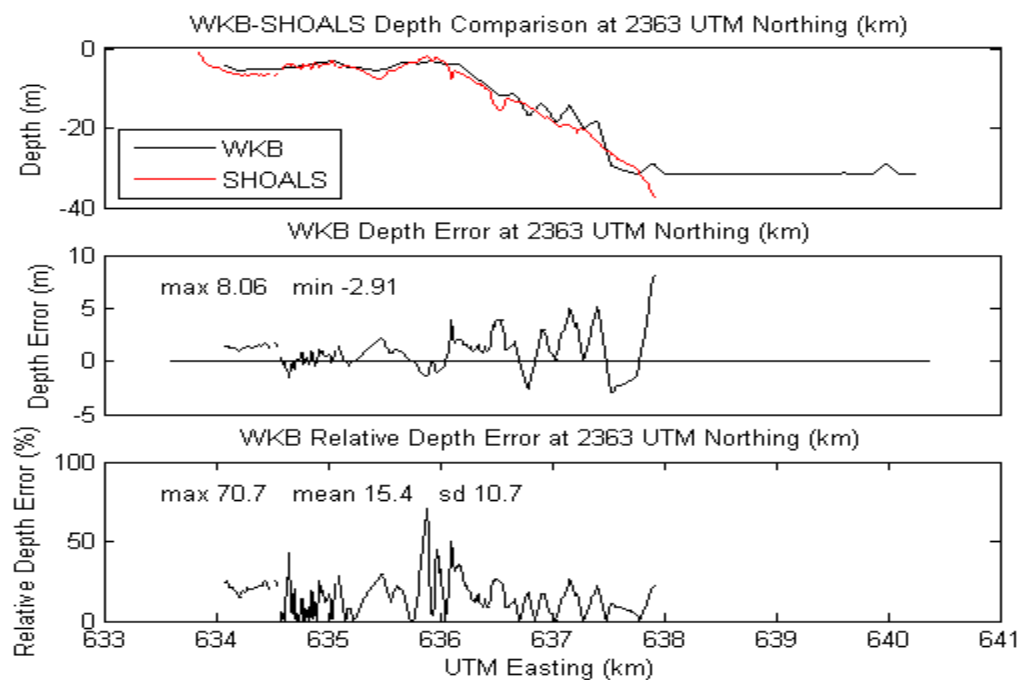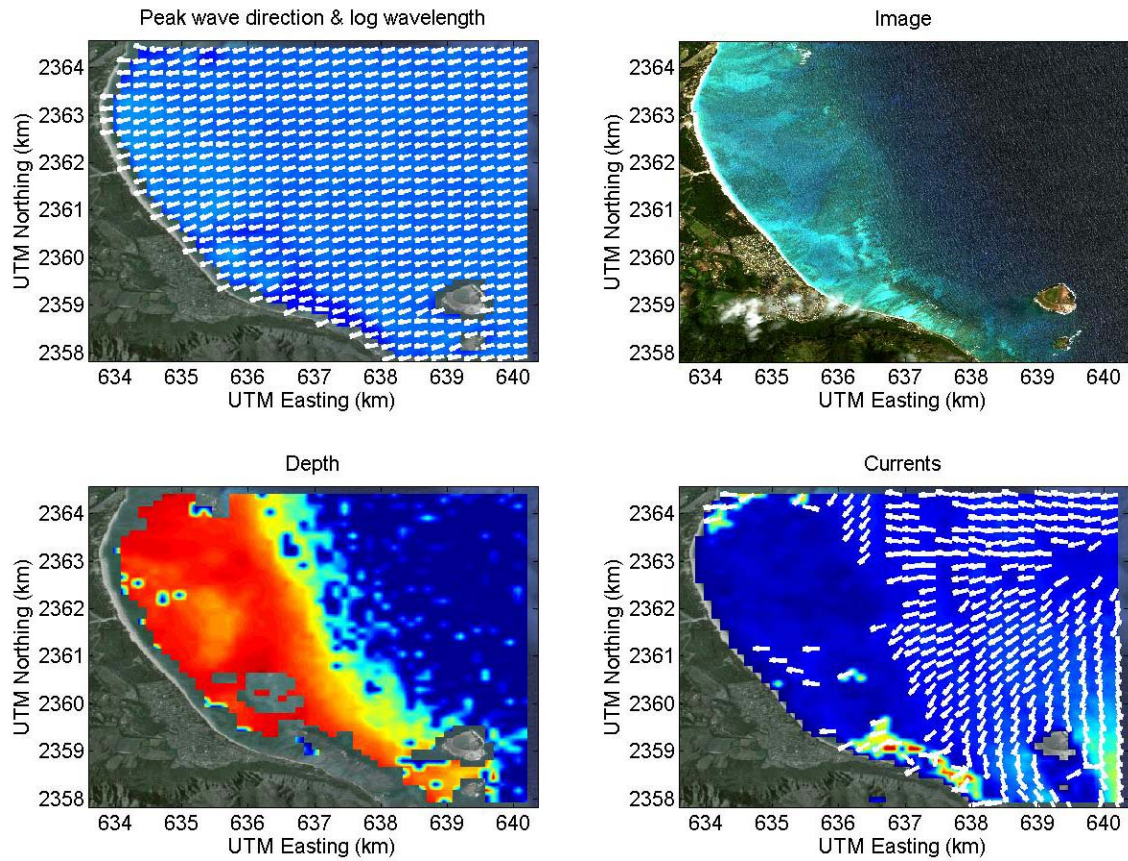Figure 71.　Transect at specified location showing 3MSI WKB (see below for more explanation of the panels)

Figure 72.　Transect at specified location showing 3MSI WKB depth plotted with SHOALS depth (top); the difference between them, or depth error (mid); and depth error as a percentage of depth, or relative depth error (bot)

CASE: 2PAN

Figure 73.   2Pan WKB output showing wave direction (top left), a true color image (top right), extracted bathymetry (bottom left), and extracted ocean currents (bottom right)
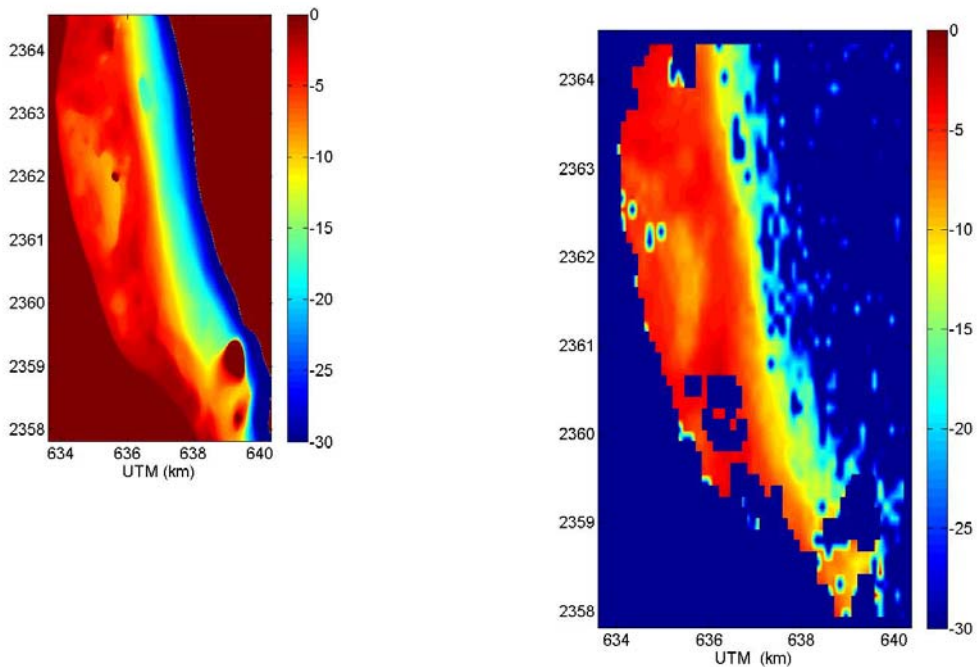
Figure 74.   Comparison maps of SHOALS (left) and 2Pan WKB (right)
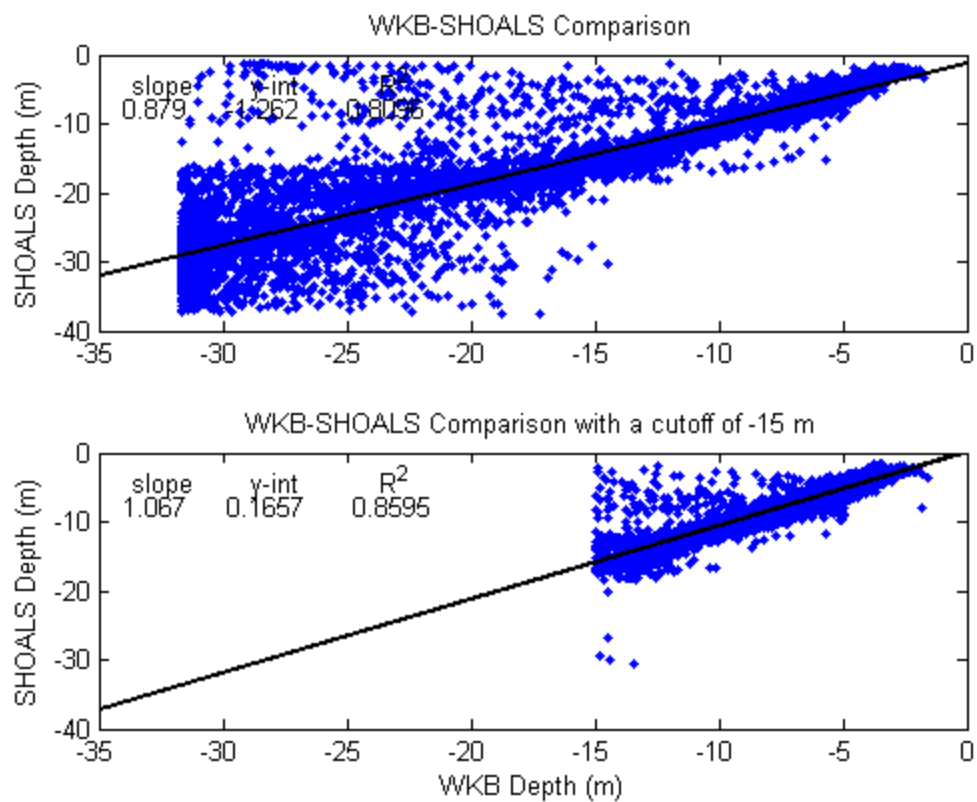

Figure 75.   2Pan scatter plot showing thinned data for all depths (top) and for just depths less than 15 m (bottom)
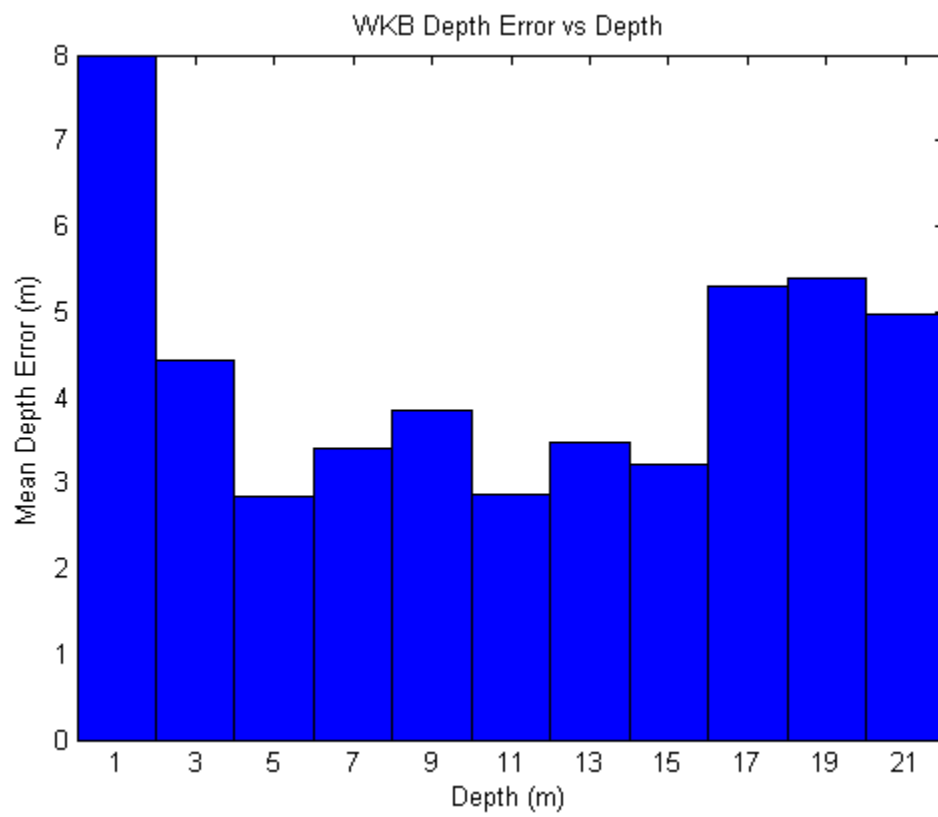
Figure 76.   2Pan bar graph showing the mean depth error for several depth bins
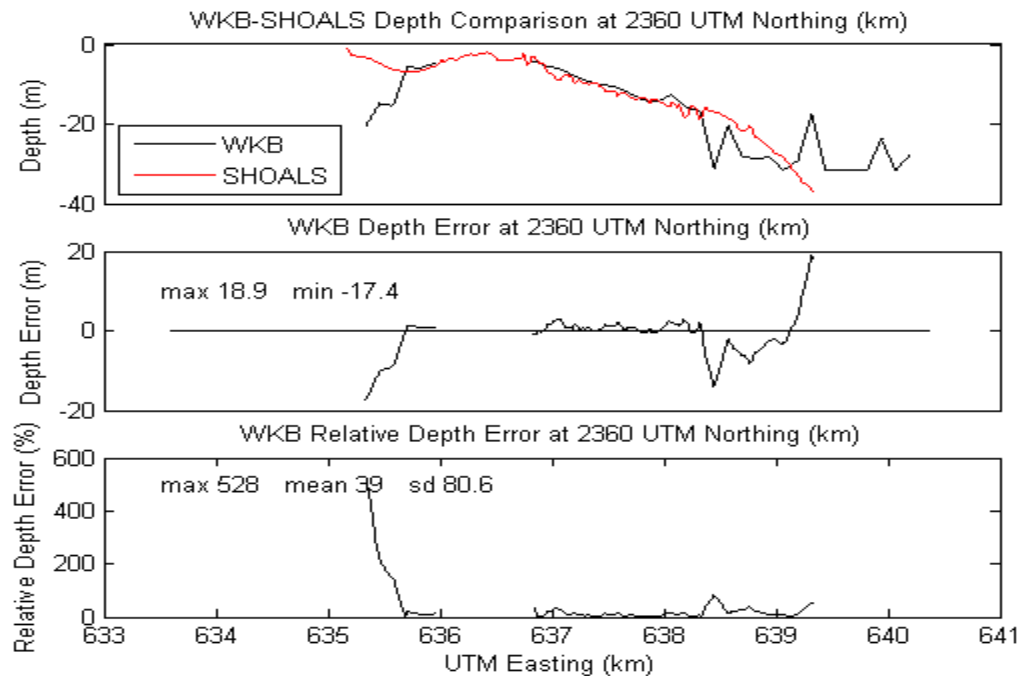
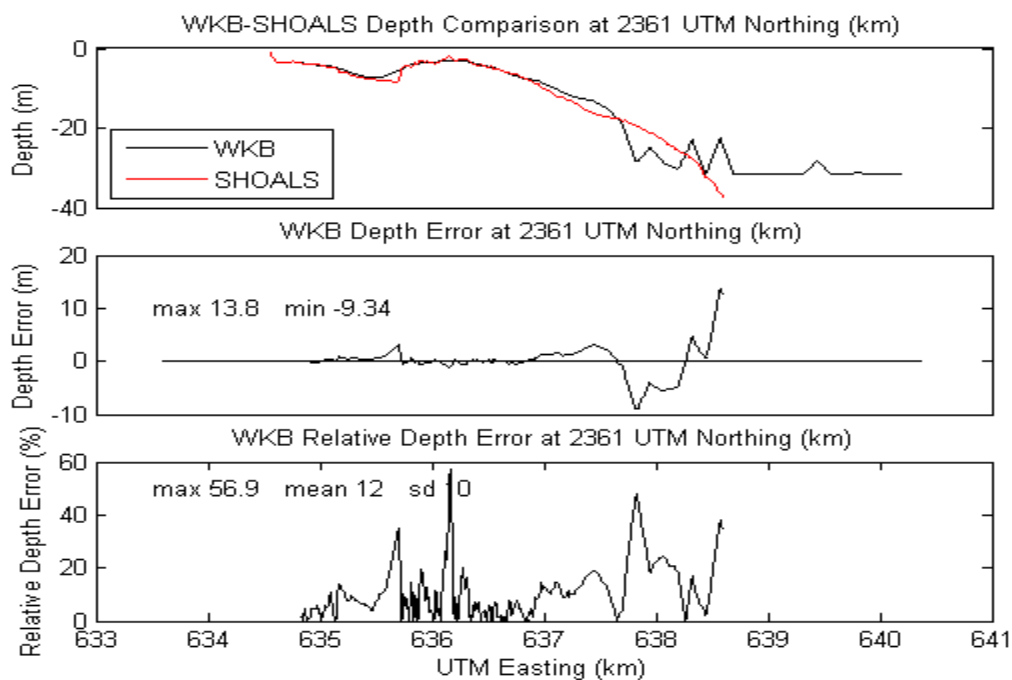Figure 77.　Transect at specified location showing 2Pan WKB (see below for more explanation of the panels)

Figure 78.　Transect at specified location showing 2Pan WKB depth plotted with SHOALS depth (top); the difference between them, or depth error (mid); and depth error as a percentage of depth, or relative depth error (bot)
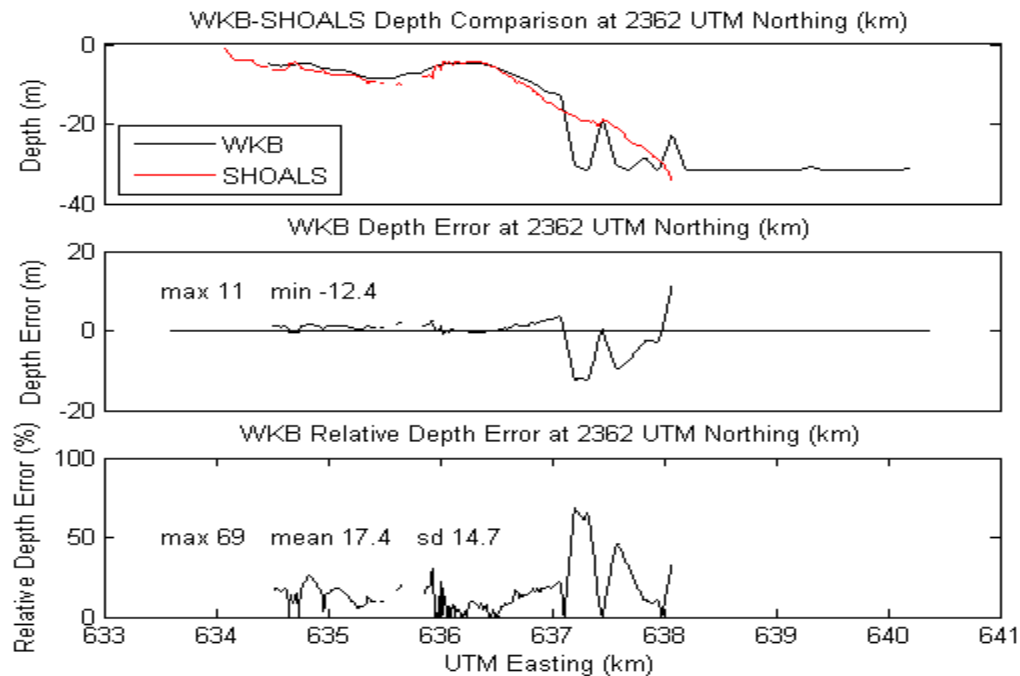
Figure 79.   Transect at specified location showing 2Pan WKB (see below for more explanation of the panels)
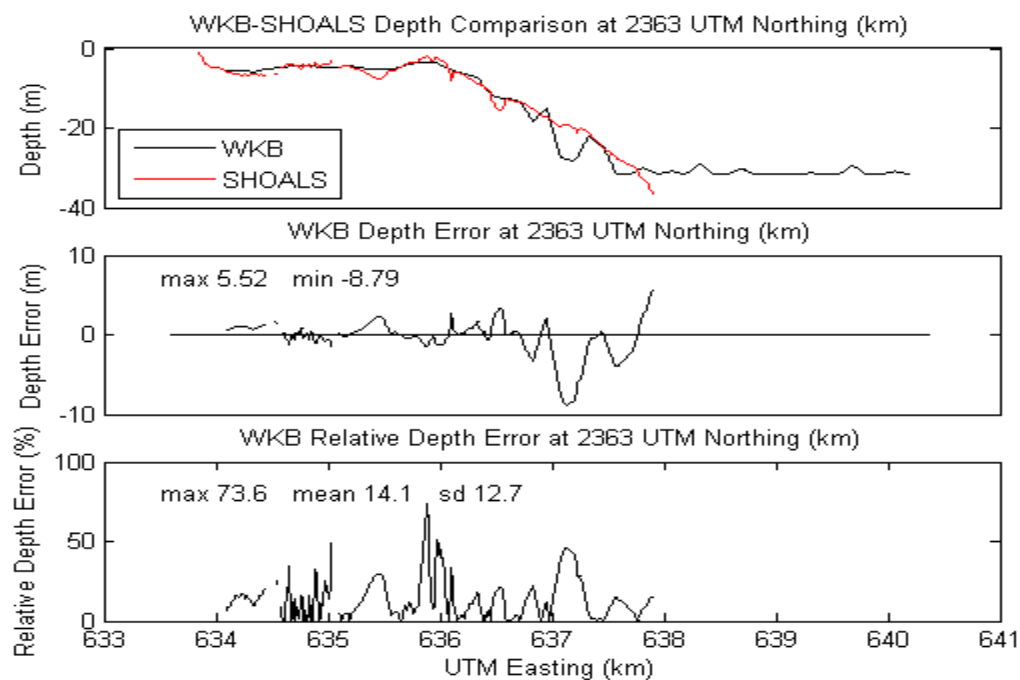

Figure 80.   Transect at specified location showing 2Pan WKB depth plotted with SHOALS depth (top); the difference between them, or depth error (mid); and depth error as a percentage of depth, or relative depth error (bot)
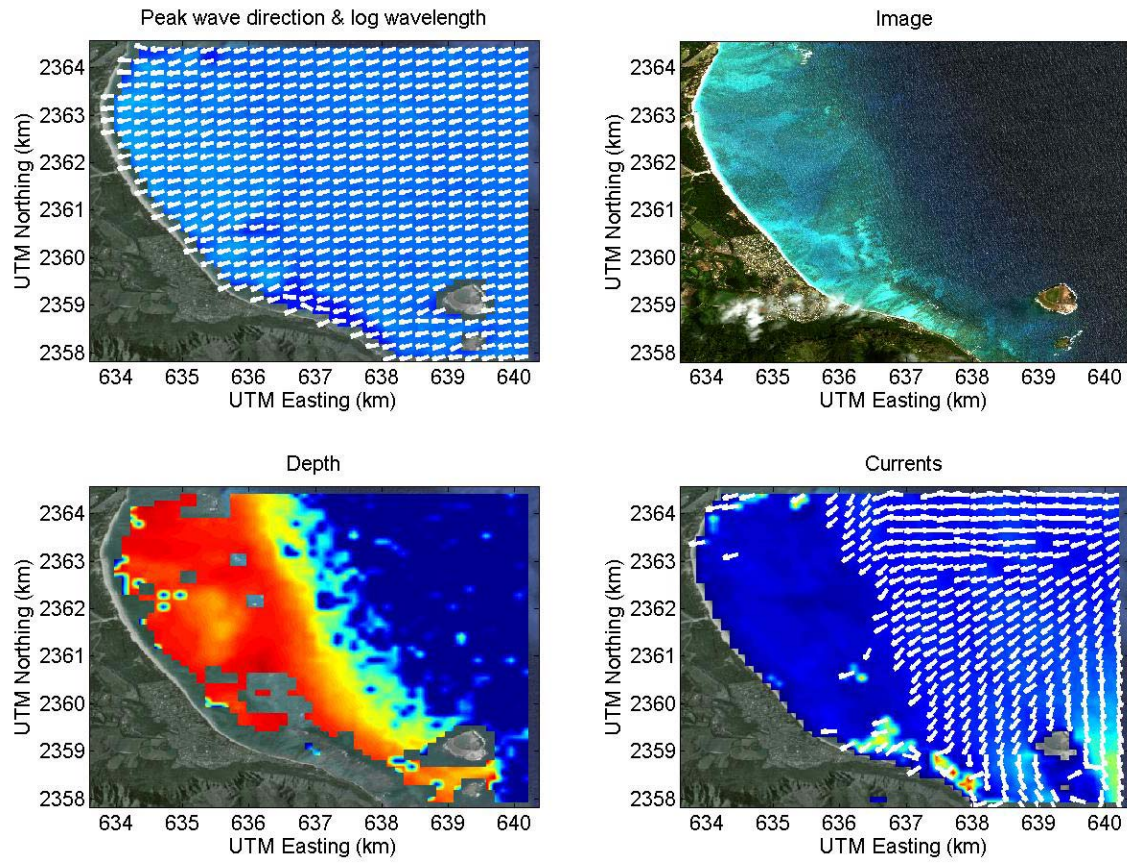
CASE: 3PAN

Figure 81.　3Pan WKB output showing wave direction (top left), a true color image (top right), extracted bathymetry (bottom left), and extracted ocean currents (bottom right)
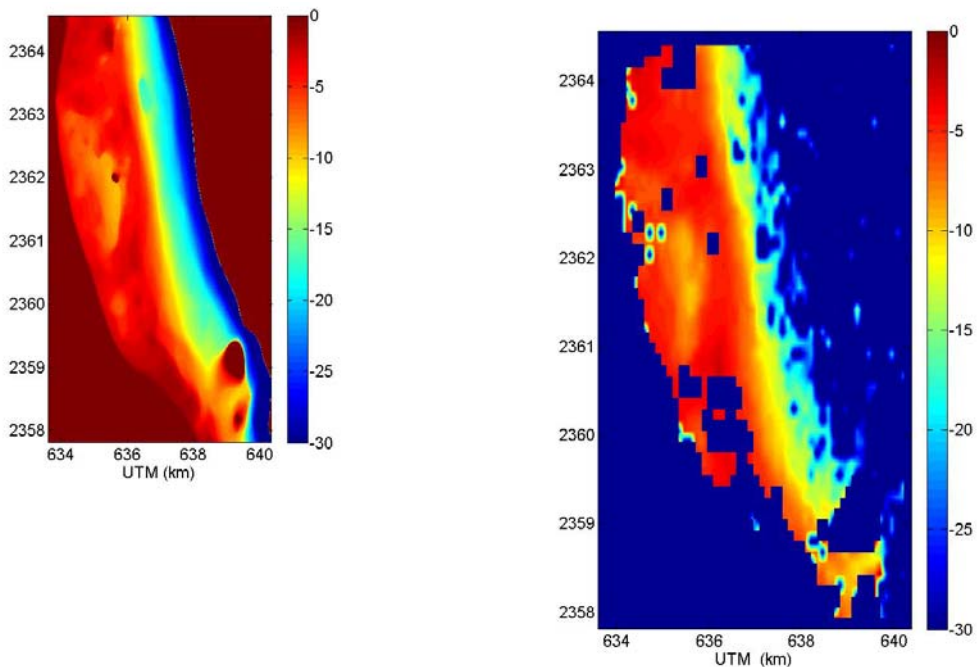
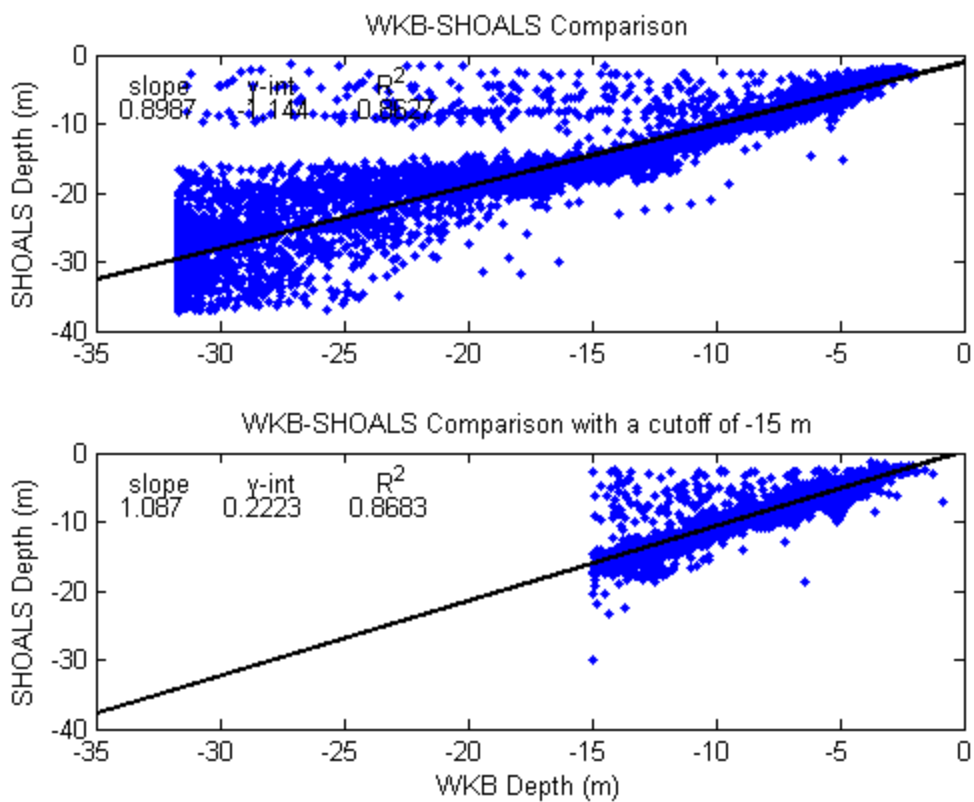Figure 82.   Comparison maps of SHOALS (left) and 3Pan WKB (right)

Figure 83.   3Pan scatter plot showing thinned data for all depths (top) and for just depths less than 15 m (bottom)

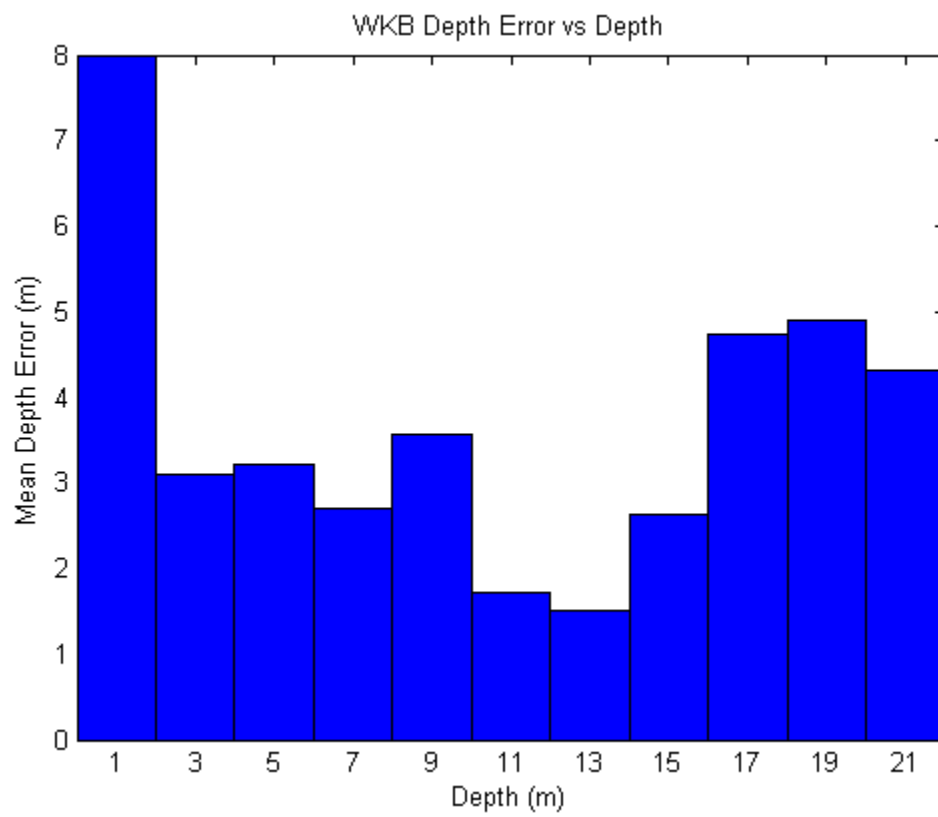Figure 84.   3Pan bar graph showing the mean depth error for several depth bins

Figure 85.   Transect at specified location showing 3Pan WKB (see below for more explanation of the panels)

Figure 86.   Transect at specified location showing 3Pan WKB depth plotted with SHOALS depth (top); the difference between them, or depth error (mid); and depth error as a percentage of depth, or relative depth error (bot)
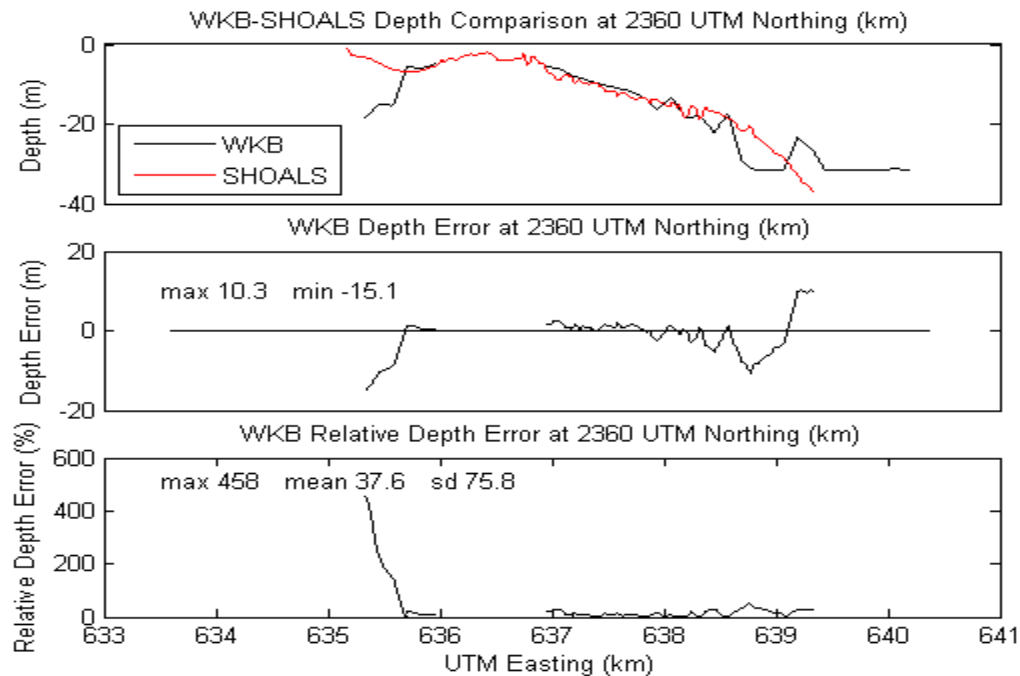
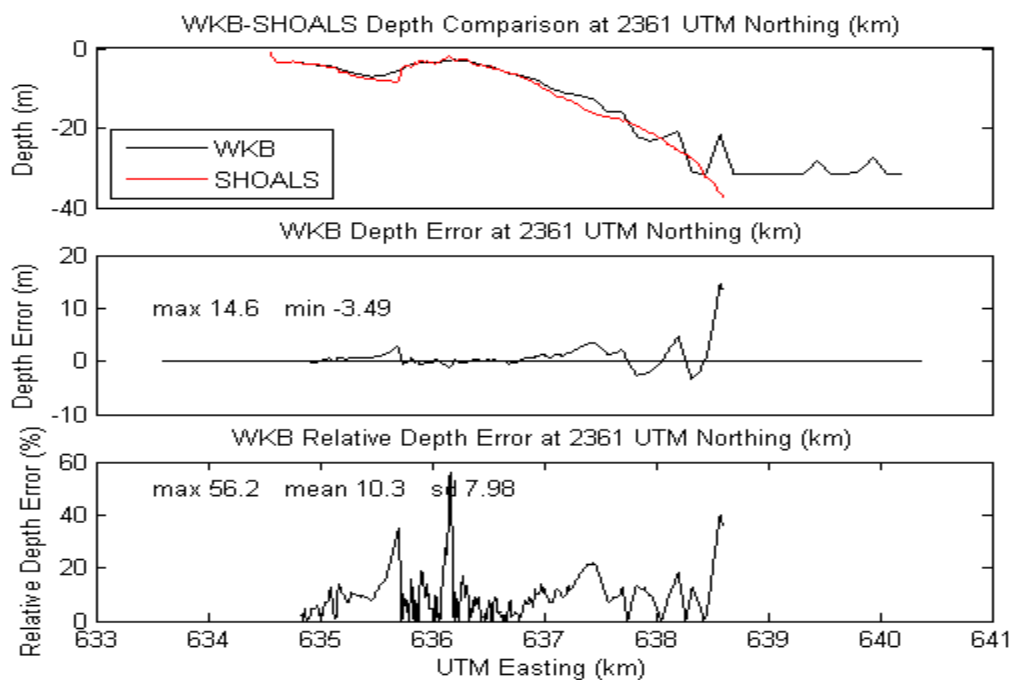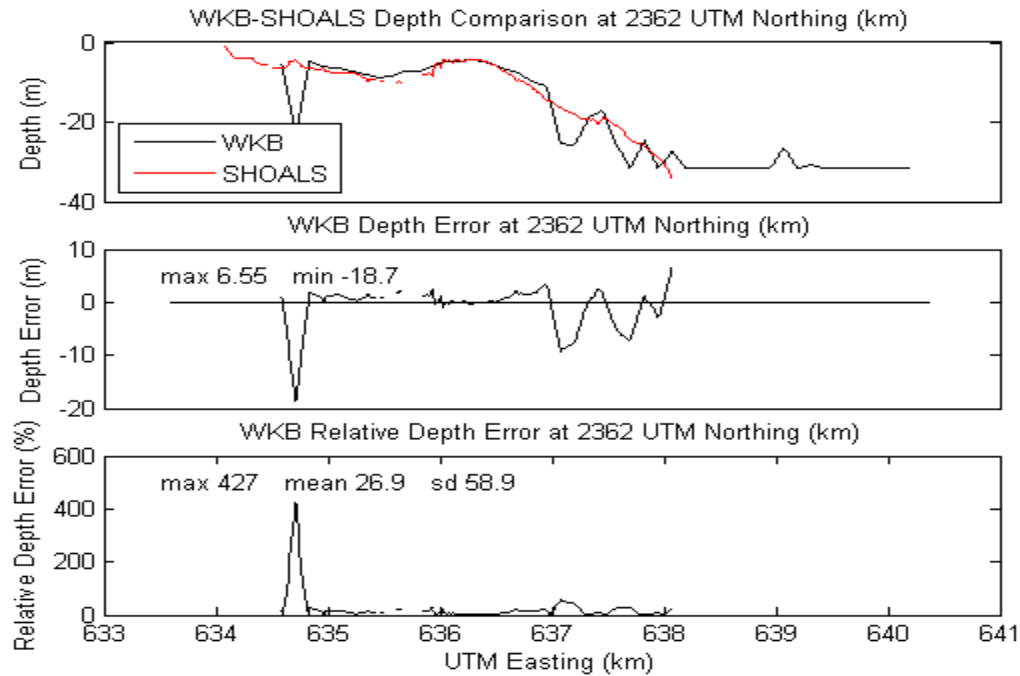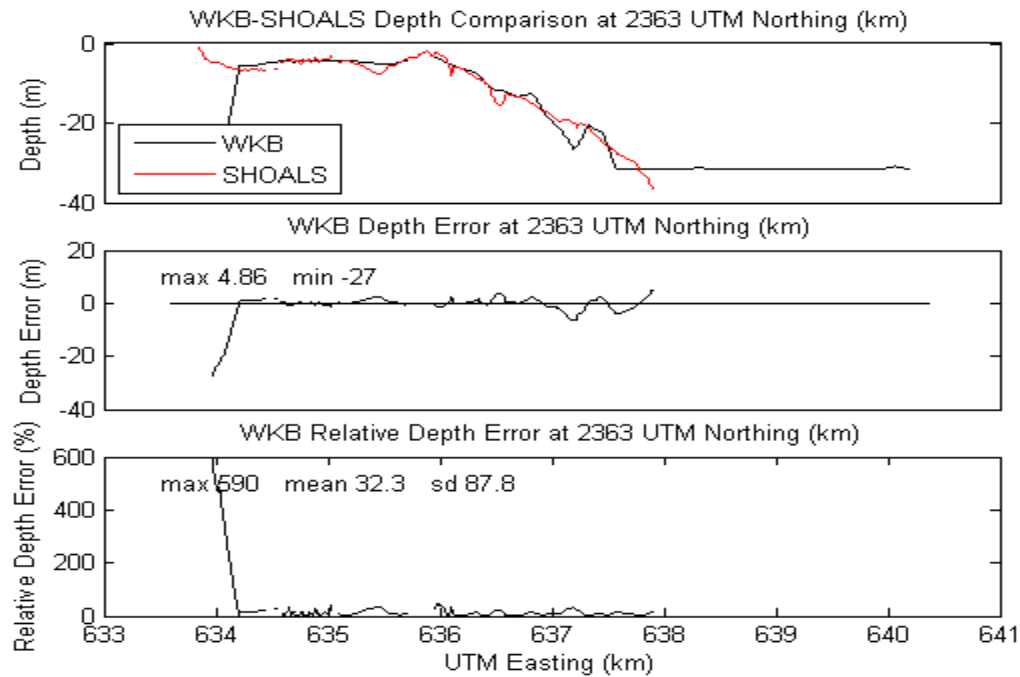Figure 87.　Transect at specified location showing 3Pan WKB (see below for more explanation of the panels)

Figure 88.　Transect at specified location showing 3Pan WKB depth plotted with SHOALS depth (top); the difference between them, or depth error (mid); and depth error as a percentage of depth, or relative depth error (bot)

LIST OF REFERENCES

Abileah, R. (2006, May). Mapping shallow water depth from satellite. *Proceedings of the ASPRS 2006 Annual Conference*, Reno, Nevada. Retrieved 11/12/2011 from http://www.asprs.org/a/publications/proceedings/reno2006/0001.pdf

Abileah, R. & Trizna, D. B. (2010). Shallow water bathymetry with an incoherent X-band radar using small (smaller) space-time image cubes. *Proceedings of the IGARSS 2010*, 4330–4333. doi: 10.1109/IGARSS.2010.5654386

Abileah, R. (2011). Methods for mapping depth and surface current. Patent application for Ron Abileah, No. 13091345, filed April 21, 2011.

Coastal Data Information Program (CDIP) website. Retrieved 1/19/2012, from http://cdip.ucsd.edu/?nav=historic&sub=data&stn=098&stream=p1&xyrmo=201103&xitem=stn_home

DigitalGlobe (2011a). WorldView-2 Data Sheet. Rev 10/11. Retrieved 12/4/2011 from http://www.digitalglobe.com/downloads/WorldView2-DS-WV2-Web.pdf

DigitalGlobe (2011b). About the WorldView-2 Satellite. Retrieved 12/4/2011 from http://worldview2.digitalglobe.com/about/

Dugan, J. P., Fetzer, G. J., Bowden, J., Farruggia, G. J., Williams, J. Z., Piotrowski, C. C., Vierra, K., Campion, D., & Sitter, D. N. (2001a). Airborne optical system for remote sensing of ocean waves. *Journal of Atmospheric and Oceanic Technology, 18*, 1267–1276.

Dugan, J. P., Piotrowski, C. C., & Williams, J. Z. (2001b). Water depth and surface current retrievals from airborne measurements of surface gravity wave dispersion. *Journal of Geophysical Research, 106, No. C8*, 16,903–16,915. doi:10.1029/2000JC000369

Dugan, J. P., Piotrowski, C. C., & Williams, J. Z. (2002). Rapid environmental assessment of nearshore METOC fields using motion imaging techniques applied to surrogate UAV data. *Oceans '02 MTS/IEEE, 4*, 1956–1961. doi: 10.1109/OCEANS.2002.1191932

Herbers, T. H. (2003). OC4211 (Ocean Dynamics II) course notes, Spring Quarter 2003. Monterey, CA: Naval Postgraduate School.

Hedges, T. S. (1976). An empirical modification to linear wave theory. *Proceedings of the Institution of Civil Engineers, 61,* 575–579.

Joint Airborne LIDAR Bathymetry Technical Center of Expertise (JALBTCX) website. Retrieved 11/10/2011, from http://shoals.sam.usace.army.mil/Charts.aspx

Lyzenga, D. R. (1978). Passive remote sensing techniques for mapping water depth and bottom features. *Applied Optics, 17*(3), 379–383.

McCarthy, B. L. (2010). *Coastal bathymetry using 8-color multispectral satellite observation of wave motion* (Master's thesis) [electronic resource]. Naval Postgraduate School, Monterey, CA.

Myrick, K. B. (2011). *Coastal bathymetry using satellite observation in support of intelligence preparation of the environment* (Master's thesis) [electronic resource]. Naval Postgraduate School, Monterey, CA.

Wackerman, C. C. & Clemente-Colon, P. (2004). Wave Refraction, Breaking, and Other Near-Shore Processes. In C. R. Jackson & J. R. Apel, *SAR Marine User's Manual* (pp. 171–188). Retrieved 11/2/2011 from http://www.sarusersmanual.com

INITIAL DISTRIBUTION LIST

1. Defense Technical Information Center
   Ft. Belvoir, VA

2. Dudley Knox Library
   Naval Postgraduate School
   Monterey, CA

3. Dr. Richard C. Olsen
   Remote Sensing Center at the Naval Postgraduate School
   Monterey, CA

4. Dr. Jamie MacMahan
   Naval Postgraduate School
   Monterey, CA

5. Mr. Ron Abileah
   jOmegak
   San Carlos, CA

6. Mr. Giovanni Marchisio
   DigitalGlobe
   Longmont, CO

7. Mr. Walter Scott
   DigitalGlobe
   Longmont, CO

8. Mr. Kumar Navulur
   DigitalGlobe
   Longmont, CO

9. Mr. Gregory Miecznik
   DigitalGlobe
   Longmont, CO

10. Mr. Milan Karspeck
    DigitalGlobe
    Longmont, CO

11. Dr. Christopher Wackerman
    General Dynamics Advanced Information Systems
    Ypsilanti, MI